

**ELECTRON DENSITY DETERMINATION AND BONDING IN TETRAGONAL
BINARY INTERMETALLICS BY CONVERGENT BEAM ELECTRON DIFFRACTION**

by

Xiahan Sang

BS, Wuhan University, 2005

MS, Institute of Metal Research, Chinese Academy of Science, 2008

Submitted to the Graduate Faculty of
Swanson School of Engineering in partial fulfillment
of the requirements for the degree of
Doctor of Philosophy

University of Pittsburgh

2012

UNIVERSITY OF PITTSBURGH
SWANSON SCHOOL OF ENGINEERING

This dissertation was presented

by

Xiahan Sang

It was defended on

May 14th, 2012

and approved by

John Barnard, Ph.D., Professor, Department of Mechanical Engineering and Materials Science

Jung-Kun Lee, Ph.D., Assistant Professor, Department of Mechanical Engineering and Materials
Science

Ravi Shankar, Ph.D., Assistant Professor, Department of Industrial Engineering

Dissertation Director: Jörg M.K. Wiezorek, Ph.D., Associate Professor, Department of
Mechanical Engineering and Materials Science

Copyright © by Xiahan Sang

2012

ELECTRON DENSITY DETERMINATION AND BONDING IN TETRAGONAL BINARY INTERMETALLICS BY CONVERGENT BEAM ELECTRON DIFFRACTION

Xiahan Sang, PhD

University of Pittsburgh, 2012

Intermetallics offer unique property combinations often superior to those of more conventional solid solution alloys of identical composition. Understanding of bonding in intermetallics would greatly accelerate development of intermetallics for advanced and high performance engineering applications. Tetragonal intermetallics $L1_0$ ordered TiAl, FePd and FePt are used as model systems to experimentally measure their electron densities using quantitative convergent beam electron diffraction (QCBED) method and then compare details of the 3d-4d (FePd) and 3d-5d (FePt) electron interactions to elucidate their role on properties of the respective ferromagnetic $L1_0$ -ordered intermetallics FePd and FePt.

A new multi-beam off-zone axis condition QCBED method has been developed to increase sensitivity of CBED patterns to change of structure factors and the anisotropic Debye-Waller (DW) factors. Unprecedented accuracy and precision in structure and DW factor measurements has been achieved by acquiring CBED patterns using beam-sample geometry that ensures strong dynamical interaction between the fast electrons and the periodic potential in the crystalline samples. This experimental method has been successfully applied to diamond cubic Si, and chemically ordered B2 cubic NiAl, tetragonal $L1_0$ ordered TiAl and FePd. The accurate and precise experimental DW and structure factors for $L1_0$ TiAl and FePd allow direct evaluation of computer calculations using the current state of the art density functional theory (DFT) based electron structure modeling. The experimental electron density difference map of $L1_0$ TiAl

shows that the DFT calculations describe bonding to a sufficient accuracy for s- and p- electrons interaction, e. g., the Al-layer. However, it indicate significant quantitative differences to the experimental measurements for the 3d-3d interactions of the Ti atoms, e.g. in the Ti layers. The DFT calculations for $L1_0$ FePd also show that the current DFT approximations insufficiently describe the interaction between Fe-Fe (3d-3d), Fe-Pd (3d-4d) and Pd-Pd (4d-4d) electrons, which indicates the necessity to evaluate applicability of different DFT approximations, and also provides experimental data for the development of new DFT approximation that better describes transition metal based intermetallic systems.

TABLE OF CONTENTS

PREFACE.....	XV
1.0 INTRODUCTION.....	1
1.1 WAVE FUNCTION AND ELECTRON DENSITY	1
1.2 CURRENT METHODS AND THEIR PROBLEMS.....	6
1.3 MULTI-BEAM OFF-ZONE AXIS METHOD.....	10
1.4 FUTURE IMPACT	12
2.0 BACKGROUND AND LITERATURE REVIEW	14
2.1 TETRAGONAL BINARY INTERMETALLICS	14
2.1.1 Tetragonal L₁₀ FePd and FePt.....	14
2.1.2 Tetragonal titanium aluminide	17
2.2 STRUCTURE FACTORS AND CHARGE DENSITY	18
2.3 CHARGE DENSITY DETERMINATION METHODS	23
2.3.1 X-ray diffraction.....	24
2.3.1.1 Conventional X-ray diffraction	24
2.3.1.2 X-ray Pendellösung method.....	26
2.3.2 Electron diffraction.....	27
2.3.2.1 Geometry of Convergent beam electron diffraction (CBED).....	30
2.3.2.2 Bloch wave theory.....	31
2.3.2.3 The energy filter system	33
2.3.2.4 Conventional CBED Methods	35

2.4	DEBYE-WALLER FACTORS DETERMINATION METHODS.....	38
2.4.1	Experimental methods.....	39
2.4.2	Theoretical methods.....	40
2.5	SIMULTANEOUS DW AND STRUCTURE FACTORS DETERMINATION	41
3.0	EXPERIMENTAL PROCEDURES AND MATERIALS	44
3.1	SAMPLE PREPARATION	44
3.2	ACQUISITION OF CBED PATTERNS.....	46
3.3	PREPROCESSING OF CBED PATTERNS	46
3.3.1	Disk positions, intensity and background	47
3.3.2	Accelerating voltage.....	48
3.4	NON-LINEAR LEAST SQUARE FITTING.....	48
3.5	SIMULTANEOUS REFINEMENT OF DW AND STRUCTURE FACTORS	49
3.6	COMPUTATIONAL MATERIALS SCIENCE METHODS	51
3.6.1	FLAPW based first principle calculations.....	52
3.6.2	Molecular dynamics (MD) simulation of DW factors.....	52
3.7	MULTI-BEAM OFF-ZONE AXIS METHOD.....	53
4.0	DEBYE WALLER FACTORS AND STRUCTURE FACTORS OF SI.....	58
4.1	RESULTS: DEBYE WALLER AND STRUCTURE FACTORS OF SILICON	60
4.1.1	Multi-Beam Diffraction Conditions	60
4.1.2	Experimental Results.....	61
4.1.2.1	Si DW factor	61
4.1.2.2	Si structure factors of the 220 and 400 reflections.....	66
4.2	DISCUSSION.....	69
4.2.1	Multi beam near zone axis method.....	69

4.2.1.1	Sensitivity of this new method to DW factors	69
4.2.1.2	Intensity Sensitivity with changes in structure factor F_g	70
4.2.1.3	R_w value	73
4.2.1.4	Beam selection	74
4.2.2	DW and structure factor determination of crystalline Si.....	75
4.3	CONCLUSION	76
5.0	DEBYE-WALLER FACTORS AND STRUCTURE FACTORS OF NIAL	77
5.1	RESULTS.....	78
5.1.1	Orientation selection – sensitivity to structure factors	78
5.1.2	Orientation selection – sensitivity to DW factors	83
5.1.3	Temperature dependence of DW factors of β -NiAl	85
5.1.4	Structure factors of β -NiAl at various temperatures.....	87
5.2	DISCUSSION.....	89
5.2.1	Comparison of DW factors with previous results	89
5.2.2	Comparison of structure factors with previous results	90
5.2.3	Temperature dependence of DW factors	91
5.3	CONCLUSION	94
6.0	THEORETICAL INTERPRETATION OF SENSITIVITY	96
6.1	THE INFLUENCE OF THE NUMBER AND AMPLITUDE OF EXCITED BLOCH WAVE BRANCHES ON PATTERN SENSITIVITY TO CHANGES IN STRUCTURE FACTOR	97
6.2	COMPARISON OF RESULTS FOR SI OBTAINED FROM THE ZONE AXIS METHOD AND THE OFF-ZONE AXIS MULTI BEAM TECHNIQUE CONDITION.....	100
6.3	EXCITATION AMPLITUDE.....	105
6.4	RESULTS INTERMETALLIC B2 ORDERED NIAL.....	113
6.5	CONCLUSIONS.....	117

7.0	ELECTRON DENSITY OF TIAL	120
7.1	REFINEMENT OF ANISOTROPIC DW FACTORS	121
7.2	RESULTS	124
7.3	DISCUSSION.....	132
7.4	SUMMARY AND CONCLUSIONS.....	136
8.0	DW FACTORS AND STRUCTURE FACTORS OF L1₀ FEPD	138
8.1	RESULTS.....	139
8.1.1	Anisotropic DW factors of L1 ₀ FePd.....	139
8.1.2	Structure factors.....	142
8.2	DISCUSSION.....	148
8.2.1	Sensitivity to DW factors	148
8.2.2	Sensitivity to structure factors	152
8.2.3	Self - consistency of structure factors refined from different zone axis..	155
8.2.4	Comparison with DFT results.....	158
8.3	CONCLUSION.....	159
9.0	PRELIMINARY RESULTS OF L1₀ FEPT	161
10.0	SUMMARY	166
10.1	RESULTS.....	166
10.2	FUTURE WORK.....	168
10.2.1	Measurements of DW and structure factors for L1 ₀ FePt	168
10.2.2	Theoretical work on L1 ₀ FePd and FePt.....	168
	BIBLIOGRAPHY.....	169

LIST OF TABLES

Table 1 Intrinsic magnetic properties of $L1_0$ phase magnets [42]	16
Table 2 Comparison between experimental and theoretical Si DW factor.....	65
Table 3 Comparison between experimental and theoretical Si structure factors $F_{g_{220}}$ and $F_{g_{400}}$. 69	
Table 4 Comparison of R_w for Si structure factor refinement with the ZAP CBED method and the multi-beam near zone axis CBED method according to condition I (Figure 10).	73
Table 5 Refined DW factors and corresponding R_w values (test case) from patterns of different sample-beam orientations	84
Table 6 DW factors of B2 NiAl at 100K, 133K, 173K and 300K.....	87
Table 7 Low-index X-ray structure factors and absorption factors of β -NiAl at 100K, 133K, 173K and 300K.....	89
Table 8 Comparison of structure factors of reflection 100, 110 and 200 at room temperature, 300K.....	90
Table 9 Experimental and theoretical DW factors.....	125
Table 10 Experimental and theoretical structure factors	126
Table 11 Electron structure factors, U_g , of $L1_0$ FePd refined from different zone axes and comparison with independent atom model (IAM) values.....	145
Table 12 X-ray structure factors of $L1_0$ FePd refined from different zone axes and comparison with independent atom model (IAM) values	146
Table 13 Refined isotropic DW factors using patterns along different orientation.....	149
Table 14 Experimental and theoretical structure factors for $L1_0$ FePd.....	159

LIST OF FIGURES

Figure 1 Relationship between tP2 cell and tP4 cell for the L10-phases.....	15
Figure 2 Fe-Pd and Fe-Pt phase diagrams & conventional unit cells of FCC and L1 ₀ phases.....	15
Figure 3 Simplified ray diagram for convergent beam electron diffraction.	31
Figure 4 An illustration of a typical EELS spectrum curve (a). Comparison between unfiltered (b) and zero-loss filter (elastically filtered) (c) CBED pattern acquired from L1 ₀ TiAl near [100] zone axis.....	35
Figure 5 (a) zone axis CBED versus off-zone axis CBED taken near [101] for FePd. (c) and (d) are line profiles along black lines in (a) and (b), respectively.	54
Figure 6 (a) electron diffraction pattern of a FCC structure along [001] zone axis. Circles are traces of intersections between the Ewald sphere and the zero order Laue plane. Two circles indicate beam directions in two four beam conditions respectively. (b) electron diffraction pattern along [011]. (c) electron diffraction pattern along [111].	57
Figure 7 A condition II Si - CBED pattern obtained at -177°C. Refinement yielded a thickness of 343.5nm. The white circle indicates the trace of the intersection of the Ewald sphere on ZOLZ plane.....	62
Figure 8 Refinement results for Si DW factors for different sample thickness at different temperatures.	63
Figure 9 Comparison between simulated disks and experimental disks after refinement for the pattern shown in Figure 7.	64
Figure 10 A Si CBED pattern acquired using condition I at -100°C. T Refinement yielded a thickness of 371.6nm. The black circle indicates the trace of the intersection of the Ewald sphere on ZOLZ plane.	66
Figure 11 Comparison between simulated discs and experimental discs after fitting for the pattern shown in Figure 10. $R_w = 0.136$ after refinement. (e) intensity profiles along the black line trace in (c) pointed by an arrow for experimental disk, simulated disc based on free atom data and simulated disc after structure factor refinement.	67

Figure 12 Refinement results of Silicon structure factors $F_{g_{220}}$ and $F_{g_{400}}$ from different sample thickness at different temperatures.	68
Figure 13 Multi-beam method (condition II) & corresponding profile (a) &(d), exited row pattern and corresponding profile (b) & (e), HOLZ method and corresponding profile (c) & (f). Rw vs. DW factor (g).....	70
Figure 14 Plot of $\frac{\partial I_0}{\partial U_g}$ at different beam conditions for different thickness.....	72
Figure 15 Inverted CBED patterns along different orientations. Black circles are traces of Ewald sphere for each orientation.....	79
Figure 16 Refinement results of patterns recording at different orientations. The first column in each part shows experimental disks. The second column shows calculated disks by relaxing structure factors and DW factors. The fourth column shows calculated disks by only relaxing DW factors and assuming IAM. The third column and the fifth column show absolute value of deviation between column1 and column 2, and between column 1 and column 4, respectively.	80
Figure 17 Refined DW factors B_{Ni} and B_{Al} versus thickness at different temperatures.	85
Figure 18 Refined structure factors versus thickness at 133K (left axis: $F_{g(100)}$, right axis: $F_{g(110)}$).	88
Figure 19 Plots of theoretical and experimental B_{Ni} and B_{Al} versus temperature. (a) Einstein model. (b) Debye model.	93
Figure 20 Simulated CBED patterns at different orientations: a) zone axis pattern, b) of – zone axis pattern multi beam orientation I (Ewald sphere intersects 000, 220, 2-20 and 400), c) of – zone axis pattern II (Ewald sphere intersects 000, 040, 400 and 440)	100
Figure 21 Excitation amplitude and dispersion surface centered about \mathbf{g}_{220} in Si, 200kV electron beam, for zone axis condition (a, b) and the multi-beam off-zone axis orientations I (c, d) and II (e, f); The branches annotated by numbers exhibit relatively strong excitation amplitudes (see text for details)	104
Figure 22 Projected structure (a) and Coulomb potential (b) for diamond cubic structure along [001] zone axis (black indicates a strongly positive potential).....	106
Figure 23 Electron probability distribution for the first 12 Bloch states for the [001] zone axis condition. The brightest area has the highest intensity. The darkest area has the lowest intensity. The highest intensity varies for each branch.....	107
Figure 24 Electron probability distribution for the first 12 Bloch states for the near [001] off-zone axis multi-beam condition.....	109

Figure 25 Sensitivity of the CBED patterns under different sample-beam orientations to the change of DW factor (a), structure factor $F_{g_{220}}$ (b) and $F_{g_{400}}$ (c) versus thickness.....	112
Figure 26 simulated CBED patterns for NiAl at zone axis condition (a) and three off-zone axis multi-beam conditions (b-d).	113
Figure 27 excitation amplitudes for NiAl zone axis condition (a) and three multi-beam conditions (b-c).....	115
Figure 28 sensitivity of intensity distribution to change of structure factors Fg(100) (a) and Fg(110) (b) and DW factors B(Ni) (c) and B(Al) (d).	117
Figure 29 (a) experimental CBED pattern acquired from γ -TiAl near [001] zone axis of a thickness of 254.5nm; (b) experimental CBED discs I, simulated discs assuming IAM $F_g(hkl)$ II, difference between $F_g(hkl)_{\text{expt}} - F_g(hkl)_{\text{IAM}}$ in (II-I), and after relaxing $F_g(hkl)$ $F_g(hkl)_{\text{expt}} - F_g(hkl)_{\text{relaxed}}$ in (III-I).....	123
Figure 30 Comparison of $F_{\text{hkl}} - F_{\text{IAM}}$ of QCBED with other F_{hkl} measurements (Holmestad and Swaminathan) and different theoretically calculated F_{hkl}	127
Figure 31 three-dimensional electron charge density distribution in the unit cell: a) experimentally determined (tetrahedral coordinated charge density localization); b) as calculated using LAPW GGA PBE	129
Figure 32 001, 004, 002 and 400 two – dimensional planar sections of the electron charge density distribution in the unit cell (illustrated in a)): b) experimentally determined; c) as calculated using LAPW GGA PBE	131
Figure 33 Off-zone axis multi-beam condition patterns acquired near (a) [001], (b) [110], (c) [100] and (d) [101] orientations. The circle in each pattern represents the trace of Ewald sphere intersecting zone order plane in reciprocal space.....	141
Figure 34 Refined DW factors for Fe and Pd. (a) $B(\text{Fe})_{11}$ and $B(\text{Pd})_{11}$ versus thickness, (b) $B(\text{Fe})_{33}$ and $B(\text{Pd})_{33}$ versus thickness.	142
Figure 35 Refinement results of CBED patterns recorded from different orientations. The first column in each part shows experimental discs. The second column shows calculated discs by using obtained DW factors and assuming IAM .The fourth column shows calculated discs by relaxing structure factors and fixing DW factors. The third column and the fifth column show absolute value of deviation between column1 and column 2, and between column 1 and column 4, respectively.	143
Figure 36 Refined structure factors versus thickness for patterns acquired near [001] zone axis (left axis: Fg(110), right axis: Fg(200)).	145

Figure 37 Difference between measured electron structure factors U_g and IAM values U_g (IAM) versus reflection g_{hkl} (a) and difference between measured X-ray structure factors F_g^X and IAM values F_g^X (IAM) versus reflection g_{hkl} (b).....	147
Figure 38 Contour maps of R_w with changing assumed isotropic DW factors along zone axes (a)[001], (b)[110], (c)[100] and (d)[101].....	151
Figure 39 Changes of R_w as increasing numbers of reflections are included and relaxed in the refinement for patterns taken along zone axes (a)[001], (b)[110], (c)[100] and (d)[101].	152
Figure 40 (a) Comparison of the electron density obtained by the IAM model approximation and the experimental CBED measurements along the $\langle 101 \rangle$ orientation in the tp4 unit cell, which is equivalent to the $\langle 111 \rangle$ orientation of the tp2 unit cell; (b) Difference of the electron density from the IAM approximation and the experimentally determined structure factors along the same direction	154
Figure 41 Dependence of the electron structure factors (a) $U_g(110)$ on the $\cos(\theta)$ and (b) $U_g(200)$ $\sin(\theta)$, where θ is the angle between the zone axis orientation, $[uvw]$, used for CBED from which the structure factor was refined and the easy magnetization axis $[001]$ of the $L1_0$ -FePd phase.	156
Figure 42 a bright field image of the ion-milled FePt	164
Figure 43 off zone axis multi-beam CBED pattern showing symmetry break.....	165

PREFACE

It is a pleasure to thank the many people who made this dissertation possible.

It is difficult to overstate my gratitude to my Ph.D. supervisor, Prof. Jörg Wiezorek, who has supported me throughout my Ph. D study with his kindness, patience, inspiration, encouragement, enthusiasm and knowledge. I would also like to thank Dr. Andreas Kulovits for his enthusiastic discussion with me on details of this dissertation and his constant help on performing experiments and theoretical analysis.

I am indebted to my many student colleagues and friends for providing a stimulating and fun environment in which to learn and grow. I am especially grateful to Zhongfan Zhang, Xiaojun Liang and Zhuoqun Li at Pitt for their help on many aspects of daily life. Can Liu, Hasan Kotan, Yaakov Idell, Giovanni Facco and Kai Zwiackner in my group were particularly helpful in providing a harmonic and friendly atmosphere in the lab.

I would like to thank Prof. Guofeng Wang and his students Zhiyao Duan and Yinkai Lei for their help on density functional theory simulation.

I am grateful to the secretaries and staff in the department of Mechanical Engineering and Materials Science for assisting me in many different ways. Albert Stewart and Cole Van Ormer deserve special mention.

Lastly, and most importantly, I wish to express my love and gratitude to my beloved wife Wen Wang and parents Jiantao Xia and Qiong Sang, for their understanding and endless love, through the duration of my studies.

1.0 INTRODUCTION

The building blocks of our world are atoms. Through interactions between the constituent atoms of certain proportions, various materials are formed with tremendously different morphology and properties. Among millions of existing materials, intermetallic phases, formed from two or more metal elements with certain crystal structures, play an important and indispensable role in the modern science and technology. The periodic arrangement of atoms in intermetallics results from strong atomic interactions, also known as bonding, between metal atoms. On the other hand, the bonding characteristics, e.g., bonding angle, bonding direction and bonding length, are also influenced by the arrangement of atoms in the space. The intrinsic physical and mechanical properties of intermetallics, important for advanced industrial and technological applications, are strongly determined by the bonding between the constituent atoms. A comprehensively theoretical and experimental comparative study of the bonding in intermetallics thus is important to facilitate investigation of intermetallic phases.

1.1 WAVE FUNCTION AND ELECTRON DENSITY

Theoretically, the behavior of a physical system is described by the wave function of particles within the system. The wave function ψ is obtained by solving the Schrödinger equation[1]. Various physical properties, e.g. phase stability [2], elastic constants [3], absorption behavior [4],

magnetic properties [5], electronic properties [6-8] and optical properties [9], are fundamentally related to the wave function. Unfortunately, analytical solution of wave function from the Schrödinger equation can only be obtained for a limited number of structures, for example, a hydrogen atom [1]. For intermetallics containing multiple atoms with more than one electron in each atom, the wave functions can only be obtained numerically using different approximations or simplifications for electron interactions terms in the Schrödinger equation [10]. The density functional theory (DFT) [10-12], by far the most successful and widely-used method, solves the Schrödinger equation for a periodic system or non-periodic system by optimizing the electron density $n(r)$ of the system instead of the many-electron wave function ψ of the system [10]. Because electron density $n(r)$ is a function of three parameters x , y and z in the space, while the wave function ψ is a function of $3n$ parameters, where n is the number of electrons in the system, the complexity of numerical calculation is greatly reduced by using the DFT theory. Hohenberg and Kohn [12] proved that an electron density $n(r)$ that minimizes the ground state energy E_{GS} determines the ground state and the wave function ψ , the solution of Schrödinger equation. Therefore, the information on interatomic bonding and all other ground state properties of a system are determined by the electron density distribution. The accuracy of the electron density distribution calculation has implications on how accurately materials properties can be predicted using the theoretical models. Modern DFT methods incorporating reasonable approximations (e.g. local density approximation (LDA) and general gradient approximation (GGA)) for the exchange and correlation energy treatment in the calculations have greatly advanced materials research by predicting properties that are comparable to most accurate experimental measurement [3, 13-17].

However, DFT has problems in describing intermolecular or interatomic interactions, especially van der Waals forces, spin-orbit coupling, charge transfer excitations, transition states, global potential energy surfaces and some other strongly correlated systems, and in calculations of the band gap in semiconductors [18-21]. DFT also has problems in dealing with finite size nano-crystalline materials, e.g. particles, where the composition and intrinsic properties differ from those of the corresponding bulk materials [22-24]. In the abovementioned cases, it would give us a better description of a system if we can experimentally measure the fundamental properties of the system, using the experimental data for validation of predictions and results from the DFT calculations. Although it is impossible to measure the wave function of a system experimentally, equivalently, the electron density could be measured, since, as stated earlier, the electron density also determines bonding and all the ground state properties [10].

Experimental measurements of electron densities for crystals with a multi-atomic motif containing mostly very low atomic number elements such as H, C, N and O, e. g. organic crystals, have been established using X-ray single crystal diffraction [25]. The extension of these X-ray diffraction based measurements to crystals containing heavier atoms with larger atomic number, e.g. metals and intermetallic systems, higher accuracy is required to convincingly determine electronic structure, as effectively smaller fractions of the total number of atomic electrons contribute to the bonding. The quantitative convergent beam electron diffraction (QCBED) method [26], which inherently measures electronic structure with higher accuracy than is possible with X-ray diffraction approaches, were introduced over the past two decades and have been applied to some metal oxides [27-32] and covalently bonded materials, such as Si [33, 34]. Most previous attempts to determine electron density for metals have suffered from the difficulty to prepare sufficiently large and defect-free samples for combinations of X-ray

diffraction to complement the experiments by QCBED methods in the transmission electron microscope (TEM) [35]. Hence, dispensing with the need for complementary X-ray diffraction experiments and determining the electron density solely from TEM using QCBED measurements would be desirable in order to study metals, alloys, and intermetallics successfully. The recent success in using novel QCBED methods alone to determine the electron density in Al [36] indicate that it is now possible to further improve the accuracy of current QCBED methods and to measure electron density of more challenging materials, namely those based on elements heavier than Si, such as intermetallic compounds, chemically ordered phases comprised only of metal atoms. The development of QCBED methods with further improved accuracy and precision is important in this context, especially when considering intermetallics containing only transition metal elements with atomic numbers larger than twenty. Current methods for electron density determination based on X-ray and/or electron diffraction are not sufficiently precise to enable accurate studies of bonding effects in these materials.

This research effort is focused on developing further the most promising current QCBED methods using diamond Si as a test case crystal and then extending applications to incrementally more complex chemically ordered crystals, e. g. NiAl, TiAl, FePd and FePt. Ultimately, this will enable a direct comparison of the 3d-4d and 3d-5d electron interactions and their effects on bonding in the isostructural $L1_0$ FePd and $L1_0$ FePt intermetallics. Notably, the phase γ -TiAl also exhibits the tetragonal $L1_0$ type crystal structure and its electronic structure has been investigated previously by theory and experiment [37-41]. Therefore, it is included here as the final benchmarking structure for the QCBED methodology that will be developed in this effort, prior to application to the cases of FePd and FePt.

$L1_0$ FePd and FePt are ferromagnetic intermetallics that are potentially useful in high density information storage devices and sensors due to their large uniaxial magnetocrystalline anisotropy constants [42] and good corrosion resistance. Despite of similarities in properties and the fact that Pd and Pt are in the same column in the periodic table, the mechanical properties of $L1_0$ FePd and FePt are different. $L1_0$ FePd is ductile and easy to cold-roll, while $L1_0$ FePt is brittle and difficult to cold-roll. The solid solution behaviors of $L1_0$ FePd and FePt are also quite different, as can be illustrated by comparing Fe-Pd and Fe-Pt phase diagrams [43] (See also Figure 2). The uniaxial magnetocrystalline anisotropy of $L1_0$ FePt ($\sim 6.6 \times 10^7$ ergs/cm³) [22] is almost four times as large as that of $L1_0$ FePd ($\sim 1.8 \times 10^7$ ergs/cm³) [42], although they are both very large. Since materials' properties are related to electronic structures, we may be able to explain these discrepancies between $L1_0$ FePd and FePt if we have a better understanding of electronic structures of both materials. The atomic number of Fe(26), Pd(46) and Pt(78) are relatively large, requiring unprecedented high accuracy in QCBED based experiments for probing the interatomic bonding in the iso-structural intermetallic phases of $L1_0$ FePd and FePt.

The main objective of this study is the accurate measurement of the electron density of $L1_0$ FePd and FePt by advancing currently available experimental methods, which support development of more reliable DFT approximations to explain materials properties of $L1_0$ FePd and FePt based on electron density. The successful realization of this objective will enable direct extension of direct measurement of electronic structures to more complex intermetallics and other chemically ordered compounds with a higher precision and accuracy than the current state of the art. This would provide theoreticians with currently unavailable experimental data for more effective validation of modeling predictions and to establish better first principle

calculation models, therefore bridging the difference between ab-initio calculation and experiments.

1.2 CURRENT METHODS AND THEIR PROBLEMS

The electron density distribution in crystals is the Fourier transform of X-ray diffraction structure factors. Traditionally X-ray structure factors are measured by quantitatively analyzing intensities of peaks of reflections in X-ray single crystal diffraction experiments [44]. Since dynamical interaction of X-ray photons and the atoms in the sample is not taken into consideration, the accuracy of this method is relatively low. For instance, for KCl a 3% difference between experimental structure factors and theoretical structure factors was regarded as “excellent” [45]. In order to evaluate experimentally effects of interatomic bonding accurate measurements with precision on the order of 0.5% or better are considered necessary [26]. The accuracy of X-ray measurements can be improved by including dynamical interactions, as in the Pendellösung method, where structure factors are measured from the periodicity of fringing patterns (‘beating patterns’) generated by interference of the diffracted X-rays obtained from a large wedge-shaped single crystal [46-48]. The accuracy of this method is as high as 0.1% for materials for which large defect-free bulk crystal can be grown and wedge-shaped geometry single crystal samples can be obtained without introduction of large densities of crystal defects. For $L1_0$ FePd and FePt and many other materials, especially metals and intermetallics, it is very difficult to grow large defect-free single crystals due to high density of anti-phase boundaries and dislocations retained upon solidification from the melt. Furthermore, the preparation of the low defect density wedge-shaped samples required for application of the Pendellösung X-ray diffraction method proves

extremely challenging for reasonably ductile materials, such as metals and most intermetallics. Synchrotron sources can generate intense X-ray beams and offer another choice to measure structure factors [26]. However, data obtained with synchrotron-based experiments is again limited by the quality of the samples that can be made.

In this study the QCBED methods are utilized to measure X-ray diffraction structure factors with commercially available transmission electron microscope (TEM) instruments. The main advantage of the QCBED methods relative to X-ray methods for structure factor measurements springs from the fact that the scattering interaction between the electron beam and the crystalline sample is confined to a very small volume, which is ensured to be defect-free using inspection by transmission electron microscope (TEM) imaging. The inspections of the sample volume regarding quality (defect-free, composition etc...) of the crystal and the QCBED experiments can be conducted in the same transmission electron microscope and in a single experimental session. The well-characterized and small sample volume used for QCBED ensures diffraction from a single crystal and the electron beam interaction with it is well described using the Bloch wave formalism of dynamic electron diffraction theory [49]. Another advantage of QCBED over X-ray diffraction is that the scattering interaction between the electron beam and the sample atoms is much stronger than that between X-rays and the sample, which enables acquisition of electron diffraction pattern with an exposure time on the order of seconds. Even converging the X-ray beam to nano scale diameters results in exposure times for high-quality diffraction patterns that would typically would be two to three orders of magnitude larger (several minutes to hours) than for QCBED, due to the intrinsically much weaker scattering of X-rays by the atoms. By minimizing the difference between experimental CBED patterns and dynamical electron diffraction theory calculated CBED patterns through refinement

and relaxing of the electron diffraction structure factors, we obtain optimized electron diffraction structure factors, which are then converted to X-ray diffraction structure factors using the Mott formula [49]. This enables detection of the slight differences between the experimental X-ray diffraction structure factors and the independent atom model (IAM) values of the structure factors, which reflects minute charge redistribution in the case of the $L1_0$ FePd and FePt systems due to 3d-4d and 3d-5d electron interactions, respectively.

QCBED has been widely used to measure highly precise structure factors of oxides [27-32]. The large magnitude of charge transfer and pronounced localization in ionic structures as compared to covalently and metallically bonded materials leads to larger differences in experimentally determined structure factors and those obtained from the IAM approximations. For example, for MgO, the electronic structure of which has been investigated by QCBED [32], two 3s electrons transfer from the Mg atom to the O atom, resulting in approximately $2/(12+8)=0.10$, i.e., about 10% charge transfer relative to the total number of electrons in the unit cell. For silicon (Si) much fewer electrons (≈ 0.258 electrons, equating to $\approx 1.8\%$ of the total electron density) from each atom transfer to form the covalent bond [33]. In pure elemental transition metals and intermetallic alloys, especially those involving only transition metals, these differences are much smaller still, due to a rather delocalized electronic charge distribution and the increased number of total electrons per atom. Bonds involve often only fractions of an elementary electronic charge as can be seen from the case of Si. To measure bonding, it is therefore necessary to determine the difference between IAM theory electron density and experimental electron density distribution with sufficient precision and accuracy. As the atomic numbers of elements in the unit cell increases, the respective percentage of electrons participating in bonding decreases. As a result, the precision and accuracy of QCBED

measurements and refinements for pure elemental metals and most intermetallics has to be much higher as compared to the case of ionic structures, such as metal oxides. Few metals, such as Cu [50, 51], and some intermetallics that contain at least one atom species that is not a transition metal, such as cubic B2 ordered NiAl [52] and cubic L1₂ ordered Ni₃Al [53] and tetragonal L1₀ ordered TiAl [37], were investigated regarding electron density distribution and bonding by CBED with some success in the past. Investigations of more challenging and complicated metallic systems with non-cubic crystal structures that only contain heavier transition metals have not been pursued successfully to date. The paucity of experimental QCBED studies for electron density determination for transition metals and the chemically ordered compounds based on them can be attributed to the required high precision and accuracy in the experimental measurements, resulting from the fact that only a very small fraction of the large number of total electrons in the unit cells are bonding contributing electrons. Therefore, in this project very high accuracy of structure factors measurement is required to investigate L1₀ FePd and FePt. Based on the assumption that 0.5% electrons transfer in L1₀ FePt, if we can achieve 0.05% accuracy in structure factors, the accuracy of measurement of transferred electronic charge is still only 10%.

Another problem hindering wider application of QCBED to different categories of materials is that currently established CBED methods are incapable of measuring accurately Debye-Waller (DW) factors, which are the basis to obtain accurate structure factors. Previous attempts always produced either large uncertainty in the measurement of DW factors (13% for the DW factor of Ni in B2 NiAl) [54], or only one or two data points that are hardly statistically convincing [34, 55]. The room temperature DW factors for atoms in the stable crystal structures of the elements, e.g. Si or Cu, are typically known from prior studies with sufficient accuracy for use as starting values in structure factor refinements. However, the DW factors of the various

atom species that constitute the unit cell content for multi-elemental chemical compounds are reasonably expected to vary from those known for the respective elements due to the effects from interatomic bonding. For example, α -Fe (BCC), γ -Fe (FCC), L1₀ FePd and FePt should have different Fe-Fe bond length and bond energy, therefore different DW factors. An alternative would be to measure DW factors by X-ray diffraction and the Wilson plot. This, however, complicates interpretation of the measurements since CBED and X-ray experiments are not always carried out at the same temperature. Plus, the sample volume interacting with X-ray beam is different from that interacting with the electron beam in CBED, which may cause further differences, for instance due to variations in elemental composition or the averaged effects from the presence of crystal imperfections. Although it is better to obtain both structure factors and DW factors using QCBED, previous attempts have shown little success, because CBED patterns that previous experiments used were not sufficiently sensitive to changes of DW factors [56].

1.3 MULTI-BEAM OFF-ZONE AXIS METHOD

To address the main problems mentioned above, (i) inability to measure Debye-Waller factor accurately for unknown crystal structures and (ii) improve the accuracy and precision of measurements of large numbers of structure factors for unknown transition metal based intermetallics to facilitate probing of bonding effects, we have developed and established a new beam-sample orientation in QCBED experiments. This method enables the simultaneous determination of multiple accurate structure factors and multiple DW factors [56-58]. In this multi-beam off-zone axis CBED method, the sample is tilted away from zone axes so that three or five diffraction beams are exactly in diffraction geometry, i.e., they intersect the surface of the

Ewald sphere, which means that those diffraction beams are strongly excited. The dynamical interactions between strongly excited diffraction beams with each other and the transmitted beam ensure that the pattern is sensitive to both structure factors and DW factors. In order to establish this new QCBED method we have used for benchmarking purposes single crystals of Si and of β -NiAl. For both types of cubic crystals high quality single crystals can be obtained and literature data exist for comparison [47, 48, 52, 54, 59]. Si provides an excellent test case for benchmarking since the structure factors associated with the structurally forbidden diffractions, e.g. for $hkl = 200$ and $hkl = 222$, are small in magnitude and only finite because of the permanent electron density localization associated with covalent bond between adjacent Si atoms. Si is a cubic face centered elemental crystal and can be described by a single, isotropic DW factor. The chemically ordered B2 structure of β -NiAl, primitive cubic with Ni at 0,0,0 and Al in the body-centered position at $\frac{1}{2}, \frac{1}{2}, \frac{1}{2}$ as the motif, has also been studied by X-ray diffraction [59], electron diffraction [52, 54] and theoretically via DFT [14, 60, 61], and requires isotropic DW factors for each of the two atom species, Ni and Al, respectively. Thus, NiAl provides a somewhat more complex challenge for the QCBED method for the simultaneous determination of numerous structure factors and DW factors than Si.

After the new QCBED method has been established using it for the benchmarking cases of Si and NiAl, we applied it with confidence to the even more challenging and complex cases of the tetragonal $L1_0$ TiAl and $L1_0$ FePd. These binary intermetallic phases have two species of atoms and require four anisotropic DW factors for an accurate description due to the tetragonal symmetry. Accurate DW factors and structure factors for Si, B2 NiAl, $L1_0$ TiAl and $L1_0$ FePd have successfully been measured using this new method developed here. Literature reports on DW factors for Si and B2 NiAl have been used for comparison of results obtained with the new

CBED method [14, 34, 47, 48, 52, 54, 60]. The electron density difference map or charge density distribution of $L1_0$ TiAl has been constructed from experimentally measured structure factors and was compared with the simulation results using different DFT approximations. Excellent agreement between experimental and theoretical electron density was achieved for $L1_0$ TiAl. For $L1_0$ FePt, the interpretation is a little more complicated, presumably due to ferromagnetism. Measurements of structure factors and DW factors of $L1_0$ FePt have been prevented to date by problems with TEM sample preparation and therefore have been deferred to the future by exploring other sample preparation techniques than conventional electrolytic polishing and argon based ion-beam thinning.

1.4 FUTURE IMPACT

The new multi-beam off zone axis method broadens the application of QCBED method to investigation of intermetallics systems with heavier atoms. Highly precise and accurate DW factors and low order structure factors can be measured solely using TEM in a reasonably small amount of experimental time, which enables systematic investigations of compound systems. The experimental data can then be compared with simulated data using different approximations of exchange term in DFT to determine which approximation is the most reasonable. Also, the accurate experimental data should provide details on how to develop new advanced DFT approximations which can better predict physical and mechanical behaviors of intermetallics.

The design of new intermetallics systems with excellent mechanical and physical properties for advanced applications such as turbines and high-capacity storage material will be greatly accelerated with the more accurate description of the exchange term in DFT. After the

3d-4d 3d-5f interactions have been fully understood, numerous transition metal intermetallic systems can be theoretically investigated with high accuracy, which saves tremendous time of experimentally making the alloys of different composition and testing the properties, not to mention the difficulty to optimize the composition to obtain the best property for a certain alloy in experiments. Since there are several tens of transition metals, the combination of those metals to form intermetallic systems is almost infinite. The influence of a trace element (or alloying element) on the properties of a certain alloy system can also be extensively studied using simulation which also saves lots of time.

2.0 BACKGROUND AND LITERATURE REVIEW

2.1 TETRAGONAL BINARY INTERMETALLICS

2.1.1 Tetragonal $L1_0$ FePd and FePt

$L1_0$ ordered FePd and FePt are layered structures with a tp2 unit cell ($L1_0$, tP2, $P4/mmm$) with an Fe atom at 0, 0, 0, and a Pd or Pt atom at 1/2, 1/2, 1/2. Lattice parameters for the tp2 unit cell (Figure 1) are $a=2.722 \text{ \AA}$ and $c=3.714 \text{ \AA}$ [62] for $L1_0$ FePd and FePt. Traditionally a larger unit cell with lattice constants $a'=3.849 \text{ \AA}$ and $c'=3.714 \text{ \AA}$, which is based on a tp4 unit cell (Figure 1, Figure 2) with 2 Fe atoms at 0, 0, 0 and 1/2, 1/2, 1/2, and 2 Pd or Pt atoms at 1/2, 0, 1/2, and 0, 1/2, 1/2, derived from the high temperature face cubic centered ($A1$, cF4, $Fm\bar{3}m$) phase (Figure 2), is used for convenience. Lattice parameters of tp2 cell for FePt were determined to be $a=2.722 \text{ \AA}$ and $b=3.7 \text{ \AA}$ by [63], $a=2.761 \text{ \AA}$ and $b=3.735 \text{ \AA}$ by [64], $a=2.717 \text{ \AA}$ and $b=3.702 \text{ \AA}$ by [65] and $a=2.726 \text{ \AA}$ and $b=3.712 \text{ \AA}$ by [66] using X-ray diffraction. The differences in these measurements are possibly caused by different compositions of the samples used in these separate experiments since the γ_2 -FePt is stable in a single phase field below 600°C for 35at.% to 55at.% Pt.

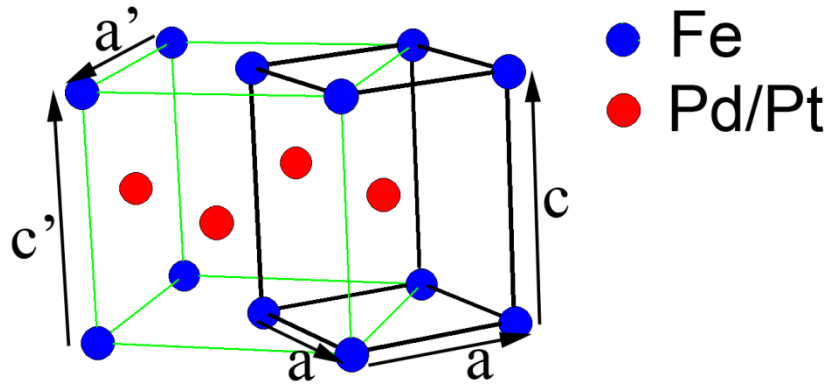


Figure 1 Relationship between tP2 cell and tP4 cell for the L10-phases

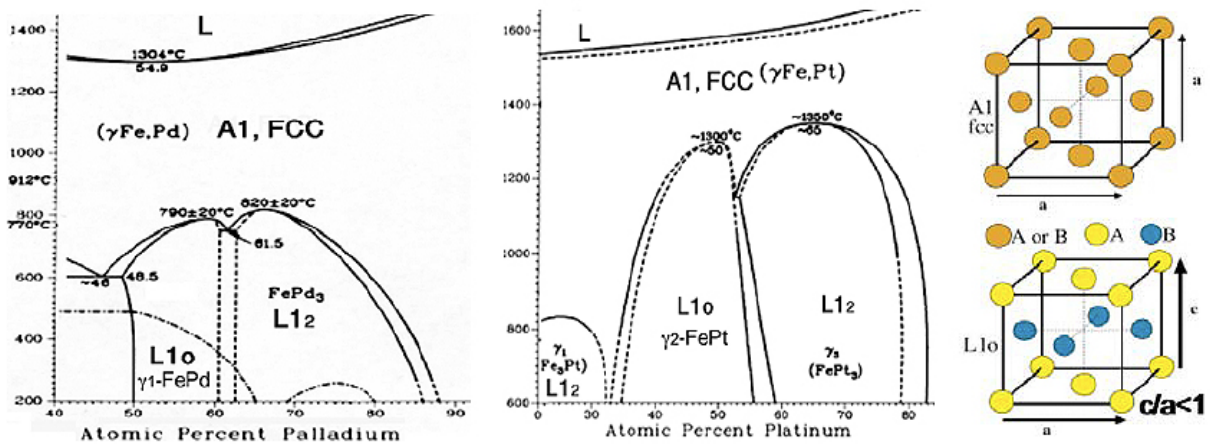


Figure 2 Fe-Pd and Fe-Pt phase diagrams & conventional unit cells of FCC and L1₀ phases

L₁₀ FePd and FePt have very large magnetocrystalline anisotropy constants ($\sim 1.8 \times 10^7$ ergs/cm³ for FePd [42] and $\sim 6.6 \times 10^7$ ergs/cm³ for FePt [22]), which make them suitable for applications in ultra-high density information storage device technologies. Table 1 lists intrinsic properties of some L₁₀ phase magnets.

Table 1 Intrinsic magnetic properties of L1₀ phase magnets [42]

	$K1 \times 10^7$	M_s	H_a	T_c	δ	γ	Dc	$(B \times H)_{max}^{theor}$
Unit	ergs cm ⁻³	emu cm ⁻³	kOe	K	nm	erg cm ⁻²	nm	MGOe
FePd	1.8	1100	33	760	7.5	17	200	48
FePt	6.6	1140	116	750	3.9	32	340	51
CoPt	4.9	800	123	840	4.5	28	610	25
MnAl	1.7	560	69	650	7.7	16	710	12
Fe ₁₄ Nd ₂ B	4.6	1270	73	585	4.6	27	230	64
SmCo ₅	11-20	910	240-440	1000	2.2-3.0	42-57	710-960	33

Pd and Pt are in the same column of periodic table and their outer shell electron configurations are quite similar (Pd: [Kr]4d¹⁰ 5s⁰, Pt: [Xe]4f¹⁴ 5d⁹ 6s¹). The bonding between Fe and Pd or Pt is mainly between Fe 3d electrons and Pd 4d electrons or Pt 5d electrons. Different bonding behaviors of 3d-4d and 3d-5d electrons interactions result in different solution behaviors of FePd and FePt (Figure 2). For example, the congruent ordering temperature for L1₀ FePd is around 790°C, which is much lower than the congruent ordering temperature for L1₀ FePt, which is around 1300°C. The congruent ordering composition for L1₀ FePd is at about 58at.% Pd, while for L1₀ FePt the congruent ordering composition is at about 50at.% Pt. Investigation of bonding behaviors may help to develop better understanding of the cause(s) for those differences mentioned above. Most material properties of intermetallics can be related to interactions between atoms and the corresponding electronic charge density distribution. In this study experimental approaches of QCBED are used to measure with sufficient precision accurate structure factors to facilitate investigation of bonding between 3d-4d and 3d-5d. This is expected

to provide accurate information based in experiments to develop basic understanding of properties of the intermetallic phases, γ 1-FePd and γ 2-FePt.

2.1.2 Tetragonal titanium aluminide

Titanium aluminide based intermetallic alloys are of interest for use in advanced transportation technologies because they offer an excellent combination of density specific mechanical properties and good oxidation resistance at temperature up to $\approx 900^\circ\text{C}$ [67-75]. The technologically most relevant γ -TiAl phase based intermetallic alloys typically contain a minority fraction of the chemically ordered α_2 -Ti₃Al phase and, depending on the details of the thermo-mechanical processing, exhibit different microstructural morphologies, e.g. ranging from fully-lamellar to equiaxed, which affect the resultant alloy property combinations [67-80]. It has been widely recognized that the desirable further optimization of performance properties of next generations of γ -TiAl based alloys can benefit from the intelligent utilization of computational studies, including DFT calculations [11, 12]. Thus, plane-wave pseudo-potential DFT in combination with the GGA has been used for calculation of elastic constants [41, 81], while shear deformation in the pure TiAl and Ti₃Al phases has been studied via DFT using ultra-soft pseudo-potentials and the GGA [82]. For the assessment of the phase stability, site preference of substitutionally incorporated alloying atoms and effects of interstitial impurity atoms the cluster variation method (CVM), full electron linearized augmented plane wave (FLAPW) approximation, combinations of projector augmented waves (PAW) and GGA and the self-consistent linearized muffin tin model within the atomic sphere approximation (LMTO ASA) have been used [83-91]. Continuous development of DFT methods is required to improve the

treatment of d- and f-orbital transition metal systems, which remains challenging for current theoretical approaches [92]. Verification and validation of theoretical results is accomplished by comparison with experimental data. Hence, the availability of highly accurate and precise experimental data that is suitable for comparison with quantities determined directly by the DFT calculations, such as the electron density and structure factors, would be of benefit. In the absence of such data, validation efforts often have to rely on other property data, e.g. bulk moduli, elastic constants or stacking fault and/or anti-phase boundary energies [93, 94], which are related to the electronic structure calculation results less directly than the metrics of the electron density distribution and structure factors.

In this study, prior to accurate DW and structure factors determination for $L1_0$ FePd and FePt, the QCBED method was applied to $L1_0$ TiAl to validate the applicability of this method to tetragonal transition metal based intermetallics. Because $L1_0$ TiAl is non-magnetic and contains only one transition metal, while both $L1_0$ FePd and FePt are magnetic and contain only transition metals, experimentally it is easier to measure DW and structure factors for $L1_0$ TiAl to establish the QCBED method. It is also interesting to experimentally validate DFT simulation for $L1_0$ TiAl using results from QCBED measurement as extensive previous literature for $L1_0$ TiAl can be compared with our results.

2.2 STRUCTURE FACTORS AND CHARGE DENSITY

Charge density in a crystal is experimentally measured by diffraction methods. In X-ray diffraction, interaction between the incident X-rays and electrons in the crystal is much stronger

than that between the X-rays and the nucleons [49]. For X-ray diffraction it is reasonable to neglect nuclear contributions and only consider contribution of atomic electrons to the scattering of X-ray photons. Therefore, the X-ray atomic scattering factor is defined as the Fourier transform of the electron density distribution of the scattering atom. The dimensionless X-ray scattering factor, f^X , has the units of number of electrons and is given by,

$$f^X = \int \rho(\mathbf{r}) \exp(-2\pi i \mathbf{g} \cdot \mathbf{r}) d\mathbf{r}, \quad (1)$$

where \mathbf{g} is a reciprocal space lattice vector of the crystal. For a crystal with an integer number i , $i \geq 1$, atoms in the unit cell, the X-ray structure factor is defined by,

$$F_{\mathbf{g}}^X = \sum_i f_i^X(s) \exp(-B_i s^2) \exp(-2\pi i \mathbf{g} \cdot \mathbf{r}_i), \quad (2)$$

where $f_i^X(s)$ is atomic scattering factor for the i^{th} atom in the unit cell located at the vector \mathbf{r}_i relative to origin, s is $|\mathbf{g}|/2$, and B_i is the Debye-Waller (DW) factor (temperature factor) for the i^{th} atom, which describes attenuation of X-ray scattering caused by thermally induced vibrations or oscillations of the atoms about their equilibrium positions. It is defined by,

$$B_i = 8\pi^2 \langle u^2 \rangle, \quad (3)$$

with $\langle u^2 \rangle$ the mean-square vibrational amplitude of the atom. The DW factor of an atom can change depending on which structure the atom is in [95, 96]. For instance the room temperature DW factor for Al atoms in the face-centered cubic structure of the element, $B(\text{Al})_{\text{FCC}} = 0.86(1) \text{ \AA}^2$, is significantly different from that of Al atoms in the intermetallic

compound NiAl with a chemically ordered primitive cubic structure of CsCl-type, $B(\text{Al})_{\text{NiAl}}=0.47(1) \text{ \AA}^2$, as a result of the differences in interatomic bonding [95, 97]. For most problems regarding X-ray diffraction, $f_i^X(s)$ for each atom is approximated by the values obtained from the independent atom model (IAM), which assumes no interaction between adjacent atoms. Expansion of $f_i^X(s)$ for each element in terms of Gaussian functions was given by Doyle and Turner [98] based on relativistic Hartree-Fock atomic wave function calculation, and is defined as,

$$f_i^X(s) = \sum_{j=1}^4 a_j \exp(-b_j s^2) + c, \quad (4)$$

In electron diffraction, electrons interact with the electrostatic potential $V(\mathbf{r})$ around an atom. This potential is related to electron density by,

$$\nabla^2 V(\mathbf{r}) = -\frac{|e|}{\epsilon_0} (\rho_n(\mathbf{r}) - \rho(\mathbf{r})), \quad (5)$$

and the electron atomic scattering factor is the Fourier transform of electrostatic potential $V(\mathbf{r})$,

$$f^e = \int V(\mathbf{r}) \exp(-2\pi i \mathbf{g} \cdot \mathbf{r}) d\mathbf{r}, \quad (6)$$

Notably both the nuclear charge density and the electronic charge density of the atom contribute to the electrostatic potential $V(\mathbf{r})$. Combining equations (1), (5) and (6), we obtain relationship between f^X and f^e ,

$$f^e(s) = \frac{|e|}{16\pi^2 \epsilon_0 s^2} [Z - f^X(s)], \quad (7)$$

This definition here uses the convention of the new version of International Tables for Crystallography [49]. The traditional definition is based on the Born approximation and is defined as,

$$f^B = \frac{2\pi m_e |e|}{h^2} f^e = \frac{m_e e^2}{8\pi \epsilon_0 h^2} \frac{Z - f^X(s)}{s^2} = 0.02393367 \frac{Z - f^X(s)}{s^2}, \quad (8)$$

with s in units of \AA^{-1} , giving f^B in units of \AA .

For a crystal with an integer number $i, i \geq 1$, atoms in the unit cell, the Fourier coefficients of crystal potential can be obtained by summing over the contents of the unit cell with a suitable phase factor,

$$V_{\mathbf{g}} = \frac{1}{\Omega} \sum_i f^e \exp(-2\pi i \mathbf{g} \cdot \mathbf{r}_i), \quad (9)$$

with $V_{\mathbf{g}}$ in the units of volts and Ω the volume of unit cell. Combining equations (8) and (9), we obtain $F_{\mathbf{g}}^B$, the electron structure factor in a crystal according to the old Born approximation system (International Tables before 1990) [49] in units of \AA , as,

$$F_{\mathbf{g}}^B = \frac{8\pi \epsilon_0 m_e |e| \Omega}{h^2} V_{\mathbf{g}}, \quad (10)$$

The other definition of electron structure factor commonly used in the literatures is defined as,

$$U_{\mathbf{g}} = \frac{\gamma F_{\mathbf{g}}^{\text{B}}}{\pi \Omega} = \frac{2m|e|V_{\mathbf{g}}}{h^2}, \quad (11)$$

where γ is the relativistic constant and is defined as,

$$\gamma = \frac{1}{\sqrt{1 - \left(\frac{v}{c}\right)^2}}, \quad (12)$$

with v the speed of electrons used in the diffraction experiment, the incident beam, and c the speed of light. $U_{\mathbf{g}}$ is in the units of \AA^{-2} and used in Bloch wave formalism, which will be introduced in the next section. Combining equations (2), (7), (9) and (11), we obtain the Mott Formula which describes the relationship between X-ray structure factor $F_{\mathbf{g}}^{\text{X}}$ and electron structure factor $U_{\mathbf{g}}$,

$$F_{\mathbf{g}}^{\text{X}} = \sum_i Z_i \exp(-B_i s^2) \exp(-2\pi i \mathbf{g} \cdot \mathbf{r}_i) - \left(\frac{C \Omega s^2}{\gamma}\right) U_{\mathbf{g}}, \quad (13)$$

where the numerical constant $C=131.2625$ if the relevant parameters are given in angstrom units. This formula is of great importance here since it enables X-ray structure factor determination from electron structure factors, which are the results of QCBED measurement. From equation (13), we can see that Debye Waller factors are included in the conversion and later we will find that they are most important to obtain accurate structure factors [56-58].

2.3 CHARGE DENSITY DETERMINATION METHODS

Scattering-based experimentations, e. g. X-ray and electron diffraction experiments have been used successfully in the past to determine structure factors and also DW factors [28, 30, 34, 99]. Based on sufficiently accurately measured sets of structure factors the electron density distribution in crystals can be determined experimentally, providing data of direct utility for validation of predictions from theory and computer simulations [28, 30, 34]. Successful application of X - ray scattering techniques for structure factor determination is limited to materials for which high-quality (low defect density) single crystals of sufficiently large dimensions (several hundred μm in linear dimensions) can be prepared. This typically has prevented experimental determination of electron density distribution and bonding charge for metals and intermetallic systems using X-rays, since it is difficult to obtain crystals of sufficient size and quality. Using a contemporary TEM, electron beam probes as small as ~ 0.2 to 1.0 nm in diameter can be formed routinely for the acquisition of CBED patterns. Hence, a major advantage of CBED methods with respect to X-ray methods is the reduced scale of the defect-free single crystal sample volume that is required. For instance, using a 10 nm diameter electron probe for a 100 nm thick sample the CBED signal is generated from a material volume of about $\sim 8 \times 10^3 \text{ nm}^3$ as compared to the $\sim 3 \times 10^{16} \text{ nm}^3 = 3 \times 10^7 \mu\text{m}^3$ sample volume typically required for X - ray diffraction. As a result, quantitative CBED has been used for accurate measurement of structure factors and the experimental determination of the electron density for a wide variety of materials, including some metals and intermetallics [28, 30, 51]. A detailed description of both methods and other scattering-based methods are discussed below.

2.3.1 X-ray diffraction

As we mentioned in the previous chapter, electron density is the Fourier transform of X-ray structure factors. Conventional ways to determine electron density of crystals involve different types of quantitative diffraction experiments, such as X-ray diffraction, electron diffraction and neutron diffraction. Up to the late 1980th, X-ray diffraction was prominently used for determining structure factors partially because the theory regarding interaction between X-ray and crystal had been established and X-ray diffraction equipment was readily available almost in every lab. Several different diffraction methods with different geometry have been used to measure X-ray structure factors.

2.3.1.1 Conventional X-ray diffraction

Depending on the quality of samples that are available for X-ray diffraction, powder diffraction or single crystal X-ray diffraction were used conventionally to measure X-ray structure factors. In kinematic approximation, the intergrated X-ray intensity I_{hkl} , which is obtained by measuring the area under the diffraction peak diffracted by a set of planes hkl , is expressed as,

$$I_g = I_0 \nu A(\mu) Q_g, \quad (14)$$

$$Q_g = \left| \frac{e^2}{m_e c^2 V} \right|^2 \frac{\lambda^3}{\sin 2\theta} |F_g|^2, \quad (15)$$

where I_0 is the incident beam intensity, $A(\mu)$ the transmission factor that is determined by absorption coefficient μ , V the volume of the irradiated material. By carefully measuring

all the factors such as diffraction angle and the absorption, structure factors F_g are deduced from diffraction intensities. One thing to mention here is that from X-ray diffraction, only amplitudes of structure factors are obtained. Nowadays the phase problem can be solved through some mathematical approaches using computer program [100]. As we will mention later, in electron diffraction, the amplitude and phase can both be measured directly. The electron density $\rho(\mathbf{r})$ is the Fourier transform of the structure factors F_g ,

$$\rho(\mathbf{r}) = \sum_g F_g \exp(-2\pi i \mathbf{g} \cdot \mathbf{r}), \quad (16)$$

However, it is very difficult to accurately measure structure factors with uncertainty on the order of 1% using X-ray diffraction since samples always contain defects, such as dislocations and stacking faults, whose interaction with X-ray is difficult to account for quantitatively. Still, X-ray diffraction works well for organic materials with light elements which have large charge transfer with relative to the total number of electrons in each atom. However, when it comes to intermetallics where the bonding related charge transfer is less than 1% (as we mentioned in the introduction part, charge transfer for $L1_0$ FePd and FePt reasonably expected to be on the order of 0.5%), X-ray diffraction cannot probe with sufficient accuracy to obtain the detailed bonding information. As Zuo [26] mentioned: “*The experimental NaCl electron density has an uncertainty in the measured structure factors which is far larger than the difference between models consisting of neutral atoms or ions*”. Since the charge transfer in NaCl is larger than that in intermetallics, the accuracy of X-ray diffraction is deemed insufficient to determine bonding behavior of most intermetallics. NaCl is an ionic structure with the fraction of charge transfer ($1/(11+17)=3.6\%$), which is much larger than that of $L1_0$ FePd and FePt.

2.3.1.2 X-ray Pendellösung method

Kato and Lang [101] are the first to introduce the X-ray Pendellösung method where beating fringes resulting from dynamical interaction between incident X-ray and an almost perfect single crystal wedge-shaped sample were measured and analyzed to obtain absolute values of structure factors. The fringes are analogue to thickness fringes in TEM [102]. The periodicity of the fringes in Pendellösung method is inversely proportional to $|F_g|$. An accuracy of 0.5% in structure factor was achieved after careful measurement of geometrical factors. Teworte [48] used a different geometry in their Pendellösung experiment which significantly reduced the required sample volume to 0.5 mm^3 . Teworte claimed that the uncertainty was probably under 0.1%. Saka [103] measured 30 planes for silicon using the same method and achieved 0.05% accuracy for 10 lower-order structure factors and 0.1% for 20 other structure factors.

To use the Pendellösung method, a wedge-shaped single crystal sample is required, which limits the application of this method to very few materials. In fact, until now, only silicon has been measured by this method and its variations [48, 101, 103, 104]. Although much higher accuracy can be obtained using this method, for most materials, it is extremely difficult to grow a single crystal with a dimension that satisfies the requirement of Pendellösung experiment. It is also difficult to cut the sample into a wedge without introducing surface defects that also influences dynamical interaction between X-ray and the sample and introduces errors. Therefore, to accurately measure structure factors for materials other than silicon, a better method should be utilized.

2.3.2 Electron diffraction

Interaction between electrons and materials is much stronger than that between X-rays and materials [102]. With 200kV electron energy, kinematic approximation fails in electron diffraction when the sample thickness is only several nanometers [105]. While in X-ray diffraction, typically a sample thickness of several millimeters is essential to get strong dynamical interaction. By examining sample areas with thickness between 100nm to 200nm or even thicker depending on the materials, researchers expect to see strong dynamical interaction in electron diffraction pattern which provides a variety of information that can be used to extract structure factors [29-31, 33, 34, 37, 51, 53, 55-58, 106-142]. For example, in the critical voltage method, the extinction of Kikuchi bands at particular voltages is used to determine low order structure factors [106, 108, 110-113, 116-119]. Early critical voltage methods were mostly applied in a systematic row condition where one or two low order structure factors could be obtained[108]. Matsuhata and Gjønnes [110-113, 143] extended this method to non-systematic conditions where three or more beams cases were investigated. The accuracy of the critical voltage method is claimed to be under 0.1%.

To use the critical voltage method to measure structure factors, a TEM that is capable of working at a continuous wide range of accelerating voltages (up to 1MV) is essential, which is a problem for most labs where commercially available TEMs mainly operate at fixed voltages between 80kV to 300kV. Another group of methods, based on intensity analysis of diffraction patterns, was favored by most researchers ([27, 30, 31, 34, 37, 51, 56, 57, 99, 107, 114, 120, 122, 123, 125, 127-130, 133, 136-138, 144-148]). Jansen [105] used selected area electron diffraction (SAED) patterns and multi-slice least squares (MSLS) method to solve the structure of

$\text{La}_3\text{Ni}_2\text{B}_2\text{N}_3$ by matching intensities of diffraction peaks. Since there are only few diffraction spots in a SAED pattern and limited experimental intensity information, the accuracy of structure factor measurement using this method is not sufficient to reveal bonding information, and is only sufficient to reconstruct the crystal structure. Therefore, the convergent beam electron diffraction method that provides more intensity information (at least 80,000 data points in a diffraction disc) in the pattern for matching has become the most successful method among those methods that we have mentioned.

Shortly after Ruska et al. invented TEM in 1933 in technical university of Berlin, in 1940 MacGillavry [149] showed that two beam condition CBED [150] could be used to measure structure factors assuming two beam approximation [151]. In 1967 Goodman and Lehmpfuhl [152] studied MgO h00-systematic interaction using CBED and determined the thickness with an accuracy of 0.5%. These old attempts were not very successful for two reasons. First, the inelastic scattering background in CBED pattern is very difficult to remove before energy filter is widely used [132, 153, 154]. The background greatly deteriorates image quality and introduces large error. Second, the two-beam approximation does not reflect the real dynamical interaction and oversimplifies what is going on inside the crystal. However, due to very limited computing power at that time, it was impossible to implement the Bloch wave formalism including hundreds of branches, as it would have resulted in unreasonable amount of computing time. Due to these two reasons, before the mid-1980's, the CBED method to accurately determine structure factors ceased to advance. The main application of CBED was therefore to use symmetry of CBED patterns to determine the space groups of crystals [155-158].

In the 1980's, two main breakthroughs occurred enabling advances in quantitative CBED experimentation. On the one hand, accurate theoretical electron diffraction intensity calculation

became possible as the computing power increased rapidly with the development of very large-scale integration chips. On the other hand, energy filtering devices that remove most of the inelastic background and allow selection of the elastically scattered electrons for formation of diffraction patterns and images in the TEM became popular. This facilitated acquisition of CBED data with considerably improved quality, as the inelastic scattering in TEM greatly compromises quality of CBED pattern, and made quantitative work impossible. To date, QCBED has been applied for structure factor measurement to many oxides [27-32], some metals [50, 51] and some intermetallics, such as cubic B2 ordered NiAl [52] and cubic L1₂ ordered Ni₃Al [53] and tetragonal L1₀ ordered TiAl [37]. The accuracy of structure factors determined using QCBED is typically in the order of 0.1%.

A major advantage of all the electron diffraction methods results from the fact that researchers can examine the area that interacts with electron beam in TEM before acquiring diffraction patterns. Defects including dislocations and planar defects always form distinct features in conventional diffraction contrast images [102]. By selecting areas that are visually defect-free from the micrograph, it is ensured that the interaction between the electron beam and the sample is confined in a perfect single crystal volume. Therefore, unlike X-ray diffraction methods, there is no need to correct for influence of defects on diffraction intensity in electron diffraction [26], which greatly increases accuracy of structure factor measurement. In electron diffraction experiments, it is also not necessary to make single crystal samples as long as the grain size is reasonably large (one magnitude larger than the spot size which is 0.5nm in our case).

2.3.2.1 Geometry of Convergent beam electron diffraction (CBED)

Figure 3 shows schematically how a CBED pattern is formed in a TEM with a simplified ray diagram. In TEM CBED mode, the sample is illuminated by a convergent electron beam, which typically has a convergence angle of less than one degree. The convergence angle of the incident electron beam has been exaggerated in Figure 3 to better illustrate the basic principles. The convergent angle can be adjusted by changing the focus lengths of the condenser lenses. Unlike selected area diffraction patterns, which show arrays of spots, CBED patterns are comprised of disks containing features such as contours and fringes (see, for example, Figure 7 and Figure 10). For each beam direction (marked with different color in Figure 3) that is included in the cone of the converged incident electron beam, a spot diffraction pattern forms on the screen (for example, red, black and yellow spot diffraction patterns formed from red, black and yellow incident beams, respectively, in Figure 3). Superposition of spot-like patterns formed from every beam contained in the cone results in a disk-like CBED pattern (Figure 3). Assuming the sample has a face centered cubic structure and the incident electron beam is parallel to the cube axis 001, the diffraction discs can be indexed as in Figure 3 with knowledge of crystallography. The center disc is formed from the incident beam and indexed as 000. The 200 type and 220 types discs are formed from the diffracted. The intensity features in the 000 disc and some low order disks have comparatively higher intensity than discs with higher scattering angle, and therefore can be used to measure structure factors. The symmetry of those discs is used to determine the space group of the crystal [157, 159-164], which is the most effective way to obtain space group information for crystals with small grains, such as precipitate phases.

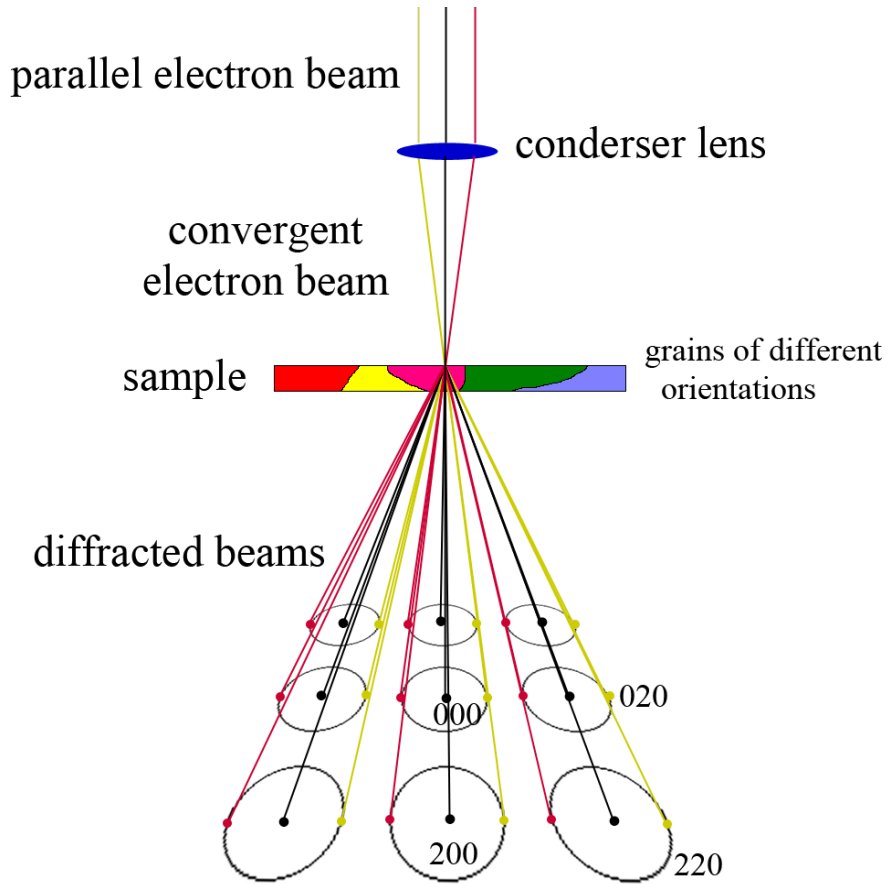


Figure 3 Simplified ray diagram for convergent beam electron diffraction.

2.3.2.2 Bloch wave theory

The theory of interaction between fast electrons and crystal was established by Bethe [151] in 1928. Detailed description of the theory can be found somewhere else [49, 107]. In the Bloch wave formalism the electron wave function $\Psi(\mathbf{r})$ in a crystal with a periodical potential $V(\mathbf{r})$ must satisfy the relativistically corrected Schrödinger equation as follows,

$$-\frac{\hbar^2}{8\pi^2 m} \nabla^2 \Psi(\mathbf{r}) - |e|V(\mathbf{r})\Psi(\mathbf{r}) = \frac{\hbar^2 K_0^2}{2m} \Psi(\mathbf{r}), \quad (17)$$

This equation can be solved by expanding the crystal potential and the wave function into Fourier series,

$$V(\mathbf{r}) = \sum_{\mathbf{g}} V_{\mathbf{g}} \exp(2\pi i \mathbf{g} \cdot \mathbf{r}), \quad (18)$$

$$\Psi(\mathbf{r}) = \sum_i c_i \exp(2\pi i \mathbf{k}^{(i)} \cdot \mathbf{r}) \sum_{\mathbf{g}} C_{\mathbf{g}}^i \exp(2\pi i \mathbf{g} \cdot \mathbf{r}), \quad (19)$$

Substitution of (15) and (16) into (14) leads to a set of basis equations

$$[K^2 - (\mathbf{k}^{(j)} + \mathbf{g})^2] C_{\mathbf{g}}^{(j)} + \sum_{\mathbf{h} \neq \mathbf{g}} U_{\mathbf{g}-\mathbf{h}} C_{\mathbf{h}}^{(j)} = 0, \quad (20)$$

with $K^2 = 2me(E + V_0)/h^2$ and $U_{\mathbf{g}} = 2meV_{\mathbf{g}}/h^2$. This *eigenvalue* problem can be solved using numerical methods. The j^{th} *eigenvalue* $k^{(j)}$, the j^{th} *eigenvector* $C_{\mathbf{g}}^{(j)}$ are calculated and form the j^{th} branch of Bloch waves,

$$\Psi^{(j)} = \sum_{\mathbf{g}} C_{\mathbf{g}}^{(j)} \exp(2\pi i (\mathbf{k}^{(j)} + \mathbf{g}) \cdot \mathbf{r}), \quad (21)$$

Wave functions $\Psi(\mathbf{r})$ can then be expressed as a sum of Bloch waves with coefficients $c^{(j)}$, which are calculated using boundary conditions on the surfaces of the thin section. Rearranging terms in equation (21), the amplitude of reflection \mathbf{g} at thickness t can be calculated,

$$\phi_{\mathbf{g}}(t) = \sum_j c^{(j)} C_{\mathbf{g}}^{(j)} \exp(2\pi i k_z^{(j)} t), \quad (22)$$

provided that beam orientation, sample orientation, accelerating voltage and sample thickness are known. The intensity along each \mathbf{g} direction after dynamical interactions can be calculated based on (18) as the intensity, I , is given as:

$$I = \left| \phi_{\mathbf{g}}(t) * \phi_{\mathbf{g}}^*(t) \right|, \quad (23)$$

We used and adapted a public-domain simulation and refinement routine software, namely MBFIT (many-beam dynamical calculations and least-squares fitting, the C code and instructions are available from <http://www.numis.northwestern.edu/edm/documentation/edm.htm#9>), based on the Bloch wave formalism developed by Tsuda and Tanaka [99]. The approximate values of the real parts of the electron scattering structure factors are converted from X-ray structure factors, which are calculated based on atomic scattering factors from Doyle and Turner [98]. The imaginary part of structure factors which takes into account thermal diffuse scattering (TDS) is calculated using a method described by Bird and King [165]. For high-index structure factors of crystals, this approximation works well since atoms behave like independent atoms at high scattering angle. For low-index structure factors, the approximated values may deviate from IAM values due to bonding and that deviation is exactly what we have to measure.

2.3.2.3 The energy filter system

The quality of experimentally collected CBED patterns has been greatly improved since the introduction of energy filtering systems for TEM instruments, which enabled imaging and diffraction in the TEM with essentially only elastically scattered electrons (energy loss of less than 5eV, zero loss peak in Figure 4) by blocking most of the inelastically scattered electrons, which have suffered inelastic scattering and associated energy losses larger than about 5 eV due to phonon scattering, plasmon scattering and inner shell ionization (Figure 4). Figure 4b (unfiltered) and Figure 4c (filtered) were acquired from exactly the same sample volume and at

the same temperature. It can be seen that Figure 4c has much clearer features than Figure 4b. The background intensity (white area means low intensity) is much reduced in Figure 4c compared with Figure 4b, resulting in much improved signal-to-noise ratio for Figure 4c. The principle of an energy filter lies in the fact that electrons with different energy have different trajectories in a varying magnetic field of a sector magnet created by the filter. Therefore, it is possible to adjust a slit to only let electrons with a certain range of energies through and form an image or diffraction pattern using those energy-selected electrons. In the experiments typically a slit width of about 10eV was selected and centered about the zero loss peak (Figure 4). In our study, we used a JEOL JEM 2100F TEM operated at nominally 200kV and equipped with a GIF TRIDIEM post-column energy filter (Gatan Inc.). When operated at nominally 200kV, for this TEM instrument the zero loss peak (Figure 4a) width (Full Width at Half Maximum) ranges from about 0.6-1.4eV, depending on the details of the extraction bias and heating currents for the Schottky-type field emission gun. The details of the low electron energy loss region (Plasmon region in Figure 4a) and the higher electron energy loss regions with the characteristic ionization edges (atom core loss and fine structure in Figure 4a) depend on the chemical composition crystal structure, crystal orientation and section thickness of the sample used. Elastic or zero loss filtering includes only the zero loss peak in the image or diffraction pattern formation process in the TEM equipped with an energy filtering device.

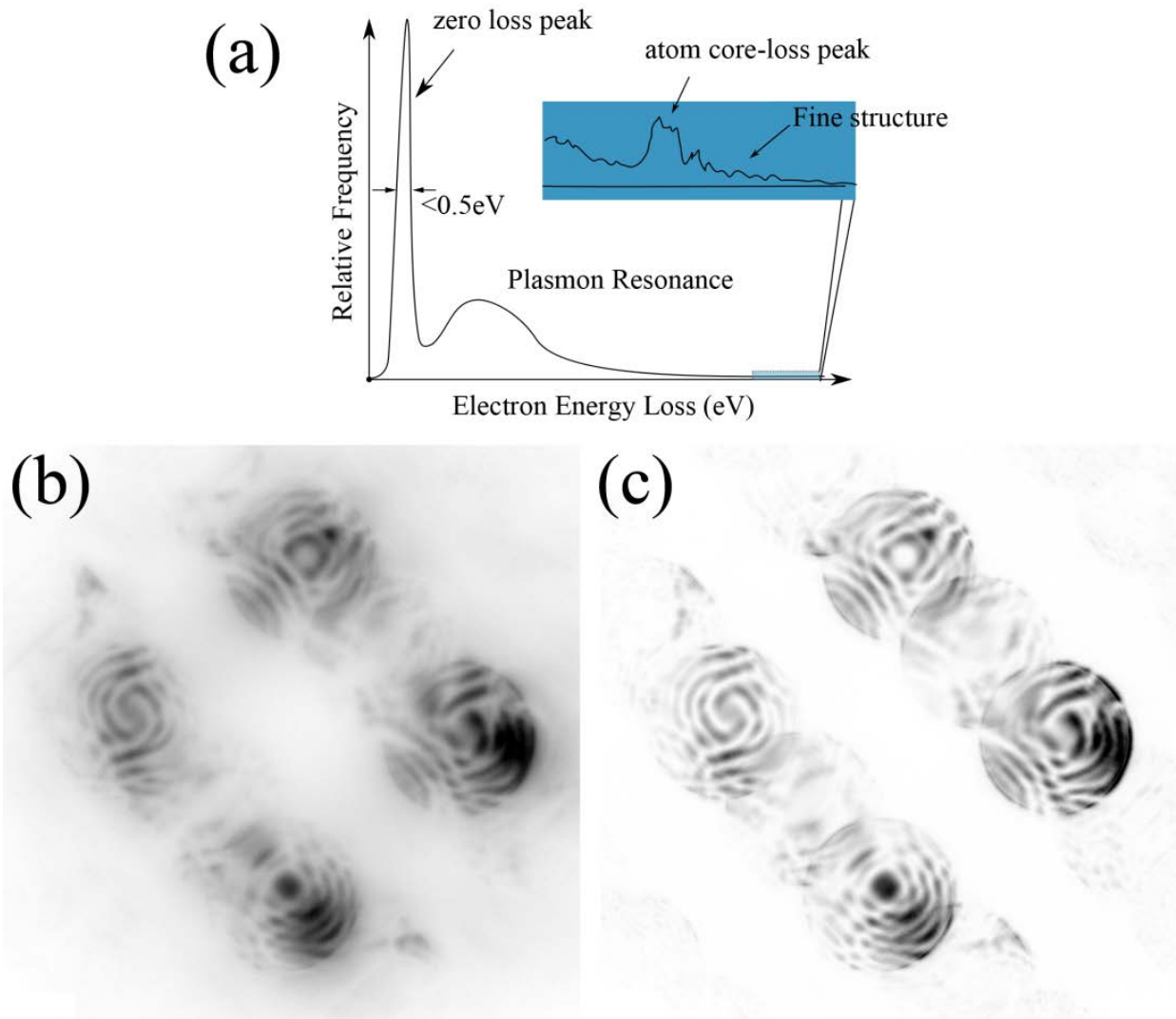


Figure 4 An illustration of a typical EELS spectrum curve (a). Comparison between unfiltered (b) and zero-loss filter (elastically filtered) (c) CBED pattern acquired from L_{10} TiAl near [100] zone axis.

2.3.2.4 Conventional CBED Methods

Structure factor measurements by quantitative CBED have utilized one of three different types of diffraction geometries, namely those associated with the so-called ‘systematic row method’ [28, 54], the zone axis pattern (ZAP) method [128, 129] and the modified ZAP method [99]. Each of

these CBED methods has its advantages and disadvantages regarding electron density determination from experimental measurements of accurate and precise structure factors.

The ‘systematic row method’ uses an incident beam direction relative to the crystal that leads to one strongly excited diffracted beam or \mathbf{g} -vector, setting up a two-beam condition comprised of the strong transmitted and the singular diffracted beam. This leads to very strong interaction between the incident beam and the diffracted beam and renders the intensities in the respective CBED discs very sensitive to changes in the corresponding structure factor $F_{\mathbf{g}}$. Line profiles in the transmitted- and the diffracted-beam CBED discs are typically used for refinement [28, 54]. This method requires the least computational time as compared to the other two methods. However, it proves difficult to determine the exact incident beam direction used in experiments and only one structure factor can be obtained from each CBED experiment.

For ZAP CBED [128, 129] the crystal is tilted into a high-symmetry or zone-axis orientation and the entire two-dimensional experimental CBED pattern is compared with a computer calculated pattern. Unlike the systematic row method, where only two beams interact strongly with each other, in ZAP CBED several low-order diffracted beams, $\mathbf{g}_{\mathbf{hkl}}$, interact dynamically, which allows for the simultaneous determination of multiple structure factors for beams in the ZOLZ. Additionally, the crystal orientation and the quality of zone axis pattern can be evaluated relatively easily by exploiting the symmetry of the ZAP. This method has been utilized rarely in the past, because of the significantly increased complexity of the refinement process and the associated increased computational effort relative to the line profile based refinements of the systematic row method. However, the increase in affordably available computing power over the past two decades has rekindled interest in the ZAP CBED method [34, 148].

Tsuda et al. modified the ZAP CBED method by including HOLZ beams into the refinement routine [99]. Since the background for high order discs is lower and more uniform than in ZOLZ discs it can be subtracted in HOLZ reflections with improved confidence. However, distortions caused by the electron optical lens system, the energy-filtering and imaging device (e.g. post-column Gatan Imaging Filter, GIF, or in-column Omega filter type and recording devices) of the TEM instrument increase with increasing scattering angle and can therefore not be neglected in the HOLZ CBED discs. Correcting for such distortions has proven difficult and tends to introduce significant uncertainty to the refinement results, which at least partly and often completely negates the advantage regarding background subtraction offered by use of the HOLZ discs. The requirement for simultaneous acquisition of the ZOLZ and HOLZ discs in the modified ZAP CBED method implies the need to use a TEM instrument equipped with an in-column Omega-type energy filtering device, since post-column energy-filtering devices currently restrict too severely the scattering angle range that can be acquired in single exposures to ZOLZ discs.

Jiang et al. [134] discussed consistency of QCBED results, obtained from the excited row method, for two different rutile samples without considering effects from sample thickness. Swaminathan et al. [166] stated that the accuracy of structure factors, determined through refinement of excited row patterns decreases with increasing sample thickness and concomitantly background signal as background corrections become problematic. Saunders [130] discussed the capabilities of the zone axis method for accurate structure factor determination and uncertainties in DW factor refinement, hinting at the advantage of the formation of a hybrid technique, which combines advantageous attributes of both zone-axis and close-to systematic or excited row

methods [130]. The multi-beam off-zone axis QCBED method what will be discussed comprehensively in this study is essentially such a hybrid technique.

Recently, Ogata et al. used modified ZAP CBED and near zone axis sample-beam orientations to determine DW factors and structure factors for Si simultaneously [34]. They acquired CBED patterns of different sample-beam orientations, which were subsequently combined and refined simultaneously, allowing for simultaneous refinement of DW factor and multiple structure factors. This work is the first publication that to some extent realizes the importance of beam-sample orientation selection and how it influences sensitivity to structure factors and DW factors in QCBED measurement. However, in this study only a single measurement of DW factors and structure factors has been performed, preventing assessment of the repeatability or reliability of the method and statistical quantification of the uncertainty of the measurement. It remains to be determined how stable this promising QCBED method is [34].

2.4 DEBYE-WALLER FACTORS DETERMINATION METHODS

As mentioned previously and noted in equation (13) (the Mott formula), DW factor plays an important role in converting experimentally measured electron diffraction structure factors to X-ray structure factors. There are two different approaches to obtain DW factors that are used in quantitative CBED.

2.4.1 Experimental methods

X-ray and neutron diffraction methods are widely used to measure DW factors by investigating damping behavior of structure factors as scattering angle increases using the method of the Wilson plot [48, 59, 167]. The accuracy of Wilson plot is not very high. Teworte [48] used X-ray diffraction to measure structure factors of Si to very high accuracy (0.1%) but obtained DW factor of Si at room temperature of 0.40 ± 0.24 with 60% uncertainty. Despite of large uncertainty entailed by this method, traditionally most prior studies have used DW factors obtained from X-ray diffraction in QCBED measurements for structure factor determination [27, 28, 30, 37, 53], since DW factors obtained from X-ray diffraction are still more reliable than those obtained from theoretical calculation [57] and QCBED measurements performed to date [54].

Another problem with X-ray diffraction methods is that the defects in the crystals may cause error in the measurement, as we mentioned in 2.3.2. The electron diffraction methods to measure DW factors should not be influenced by defects.

Several research groups [34, 54] have attempted to measure DW factors using QCBED methods, but results were not very reliable. As stated before, measurement of DW factors for Ni in B2 NiAl using QCBED has an uncertainty of about 13% [54]. In the other cases, DW factors were always obtained from only one CBED pattern [34, 54, 55, 168], which is statistically unconvincing.

2.4.2 Theoretical methods

DW factors are related to the phonon density of states (PDOS) $g(\omega)$, which is the Fourier transform (FT) of the velocity-velocity auto-correlation function [169],

$$g(\omega) = \int e^{i\omega t} \frac{\langle v(t)v(0) \rangle}{\langle v(0)v(0) \rangle} dt, \quad (24)$$

The DW factors are then obtained by calculating the integral with the normalized PDOS [170],

$$B = \frac{4\pi^2\hbar}{m} \int_0^{\omega_m} \coth\left(\frac{\hbar\omega}{2k_B T}\right) \frac{g(\omega)}{\omega} d\omega, \text{ with } \int_0^{\omega_m} g(\omega) d\omega = 1, \quad (25)$$

Conventionally, to calculate the velocity-velocity auto-correlation function, a molecular dynamics (MD) simulation software (for example, LAMMPS [171] (<http://lammps.sandia.gov>)) should be used to simulate the trajectory of atoms in the structure. The information of velocities of atoms after each step is recorded and used to estimate the velocity-velocity auto-correlation function. A large supercell (at least $20 \times 20 \times 20$ unit cells), a large number of simulation steps (at least 500,000) and a reasonably small step size (1fs, depending on the highest frequency of atomic vibration in the system) are essential to obtain good velocity-velocity autocorrelation functions. The accuracy of DW factors predicted by this method largely relies on the quality of the semi-empirical potential [60, 172] that is used in the MD simulation and is conventionally constructed by combining ab-initio calculation and experimental parameters. Due to the difficulty in constructing a perfect potential that perfectly describes the system, great discrepancy

is expected to obtain between simulated DW factors and experimentally measured DW factors [60].

2.5 SIMULTANEOUS DW AND STRUCTURE FACTORS DETERMINATION

Methods for CBED experiments that enable robust simultaneous refinements for DW factors and multiple structure factors are very desirable in the quest to determine experimentally electron densities in crystals. The room temperature DW factors for atoms in the stable crystal structures of the elements, e.g. Si or Cu, are typically known from prior studies with sufficient accuracy for use as starting values in structure factor refinements. However, the DW factors of the various atom species that constitute the unit cell content for multi-elemental chemical compounds, e.g. metal-oxide, -nitride, -carbide, -boride phases and also for intermetallic compounds, are reasonably expected to vary from those known for the respective elements due to the effects from interatomic bonding. For instance the room temperature DW factor for Al atoms in the face-centered cubic structure of the element, $B(\text{Al})_{\text{FCC}}=0.86(1) \text{ \AA}^2$, is significantly different from that of Al atoms in the intermetallic compound NiAl with a chemically ordered primitive cubic structure of CsCl-type, $B(\text{Al})_{\text{NiAl}}=0.47(1) \text{ \AA}^2$, as a result of the differences in interatomic bonding [95, 97]. Therefore, to determine experimentally the electron density and probe interatomic bonding in multi-elemental chemical compounds it is necessary to refine DW factors and structure factors simultaneously. Ideally, this is accomplished by utilization of sufficiently information rich data obtained from a single sample of the material in a single experimental TEM session, since this limits uncertainty arising from non-systematic effects, such as even

minor variations in chemical composition between different samples of a given phase/material or significant changes in background intensities for instance.

As mentioned in section 2.3.2.4, previous QCBED methods do not provide CBED patterns that are sufficiently sensitive to DW and structure factors simultaneously. The current study introduces different sample-beam orientations, which provide an effective combination of advantages of the systematic row method, e.g. reasonable computational effort, high-contrast dynamical features in the disc, and the ZAP method, e.g. easy determination of incident beam direction, simultaneous determination of multiple structure factors, and are suitable for quantitative CBED experimentation without the need for an in-column Omega-type energy filtering device equipped TEM instrument. To achieve both high sensitivity for structure factor and DW factor refinement and easily examinable symmetry, CBED patterns are recorded for crystal orientations relative to the incident beam that are within a few Bragg angles of a low-order zone axis orientation with three or more strongly diffracting beams. These orientations are referred to as multi-beam near zone axis orientations in the remainder of the manuscript. Dynamical interaction of four (transmitted and three diffracted beams) or six (transmitted and five diffracted) strongly excited beams restricts and distributes intensity uniformly among all excited discs, including the transmitted beam or zero-beam disk. This constitutes a major advantage vis-à-vis to ZAP CBED in which the intensity in the center disc is always much higher as compared to that of the diffracted-beam discs, corrupting intensities in the diffracted discs by background and noise. Additionally, it has been shown that off-zone-axis patterns are more sensitive to structure factor changes than perfect on-axis ZAP [34, 173]. In a prior study [153] off-zone axis patterns have been used to illustrate the advantage for improved background subtraction in quantification of CBED pattern intensities and structure factors have been

successfully determined by QCBED without use of an energy filter. However, the method was not applied specifically for Debye Waller (DW) factor determination. In the following chapters, the development and optimization of an off-axis multi-beam QCBED method will be established.

3.0 EXPERIMENTAL PROCEDURES AND MATERIALS

3.1 SAMPLE PREPARATION

We have used four materials (Si, B2 NiAl, L1₀ FePd, L1₀ TiAl) for QCBED experiments in this study. The Silicon sample used for TEM investigation was obtained from a Si single crystal wafer with [001] surface normal and a thickness of 350 μ m. Discs with a diameter of 3 mm were cut using a South Bay Technology Model 350 ultrasonic cutter. Those discs were then reduced in thickness to about 50 μ m and mounted on copper rings. The final polishing to electron transparency was conducted using a Fischione Model 1010 low angle ion milling & polishing system.

β -NiAl samples used for TEM investigation were obtained from an equiatomic composition β -NiAl single crystal plate with [001] surface normal by electro-polishing 3mm diameter discs with a solution of 5% perchloric acid and 95% ethanol at -30°C.

High purity elemental Ti (99.995% pure) and Al (99.999% pure) metal was used to prepare intermetallic TiAl by arc melting. After homogenization for 100 hours at 1473K (1200°C) a morphologically equiaxed two phase mixture of L1₀ ordered γ – TiAl with a minor fraction of α_2 – TiAl was observed by transmission electron microscopy (TEM) and scanning electron microscopy (SEM). The composition and the degree of long range order of the L1₀ – ordered γ – TiAl were measured both at the local scale with the TEM probes and on a larger

meso-scale in the SEM. Using combinations of analytical SEM and TEM techniques, namely energy dispersive X-ray spectroscopy (EDS) and electron diffraction, inclusive of QCBED, it has been determined that the γ -phase studied here is fully ordered and of equiatomic composition $\text{Ti}_{50}\text{Al}_{50}$. TEM samples were prepared from 3mm discs by electro-polishing using a solution of 60% methanol, 35% butanol and 5% perchloric acid at 30V and -20°C .

L1_0 FePd samples used for TEM investigations were prepared from an equiatomic chemically disordered FCC - FePd ($A1$, $cF4$, $Fm3m$) single crystal. Sections were cut such, that single crystalline TEM samples with surface plane normal axes parallel to $[001]$ and $[110]$ directions could be fabricated. The plates were first heat-treated at 550°C for 5 hours, to fully order the specimens. Subsequently a heat treatment for 95 hours at 600°C was carried out to maximize the grain size. Finally, to maximize the long-range order (LRO) parameter and reduce the point defect concentration the samples were heat treated at 400°C for 24 hours. The 3mm diameter discs were electro-polished to electron transparency using a solution of 82% acetic acid, 9% perchloric acid and 9% ethanol at 6°C .

Prior to each TEM session, the TEM samples were plasma-cleaned using a South Bay Technology 'PC 2000' Plasma Cleaner, operated with a forward power about 140 watts and a frequency of 13.56 MHz, to remove carbonaceous contamination from the sample surface. The plasma generating gas is comprised of oxygen and argon with volume ratio 1:5.

3.2 ACQUISITION OF CBED PATTERNS

Experimental CBED patterns were acquired using a JEOL JEM 2100F TEM operated at nominally 200KV and equipped with a GIF TRIDIEM post-column energy filter (Gatan Inc.). A double-tilt cooling stage holder (Gatan Inc.) was used to acquire CBED patterns at temperatures as low as $-177^{\circ}\text{C} \approx 96\text{K}$ to reduce thermal diffuse scattering (TDS). Zero-loss peak, energy filtered CBED patterns were acquired using an electron beam diameter of 0.5 nm, essentially eliminating the possible role of thickness variations on the CBED pattern intensity, with a 5eV-8eV wide energy-selecting slit and recorded on a charge-coupled device (CCD) camera with a maximum resolution of 2048×2048 .

3.3 PREPROCESSING OF CBED PATTERNS

Before analyzing the CBED patterns we acquired quantitatively, it is necessary to transcribe the data format of the graphic files acquired with the CCD of the GIF TRIDIEM to a format that a structure factor refinement program can read. Here, a program called AdjCbd has been developed to analyze the experimentally acquired CBED patterns and to extract information from experimental patterns. The program is capable of reading a dm3 file (with the proprietary GATAN file format of the Digital Micrograph software suite), finding positions of individual CBED disks, measure and apply distortion corrections, background reduction and generating intensity files compatible with the public domain CBED and structure factor refinement program MBFIT.

3.3.1 Disk positions, intensity and background

The intensity variation in a given CBED disc is caused by the range of different beam directions contained in a disk, since all the other conditions (e.g. thickness of crystal section) are the same for the pixels in the CBED disc. A unique beam direction is associated with a diffraction spots pattern distributed in each corresponding disk. Therefore, an accurate coordinate system in reciprocal space should be established for each CBED pattern. In the AdjCbd program, we use two-dimensional periodic arrays of circles to delineate edges of the CBED disks. We manually adjust positions of the center circle and the other two independent vectors of the CBED disk array until differences between the circles and edges of the disks are minimized. The two vectors are then related to the two shortest reciprocal lattice vectors along that particular zone axis. The beam direction associated with each point in the disks is then calculated using the calibration. For zero-order Laue zone (ZOLZ) patterns the non-linear distortion is negligible. However, linear distortions are commonly encountered in the CCD and post-column energy-filtering device. Thus, the angle between $[220]^*$ and $[2-20]^*$, here the notation $[hkl]^*$ refers to reciprocal lattice vectors or scattering vectors, observed in experimental silicon $[001]$ CBED patterns is consistently not exactly 90 degrees. When higher-order Laue zone (HOLZ) disks are included in the refinement, the non-linear distortion should be taken into consideration, which is achieved by analyzing displacements of points of intersections of Kikuchi bands. In the newly developed QCBED method only the ZOLZ disks are used, which are not affected by these higher-order effects, and the non-linear distortion correction is not necessary.

Some researchers prefer to include the background into the refinement process in order to relax the background [30, 129]. We used an average value obtained from circular traces along a

ring around each disc and then assigned this value as a constant background for the corresponding disc. That assumption has proven sufficient for Si. For B2 NiAl and L1₀ FePd, we assumed zero background, which yielded the best refinement compared to other assumptions. This might become a problem for future work. Background treatment remains a problem in quantification of electron diffraction data.

3.3.2 Accelerating voltage

We used the single crystal Si to measure the accelerating voltage of the TEM instrument used for the CBED experiments following the HOLZ line matching technique [174] and determined the voltage as 203 kV. The 3kV difference is caused by the post-column GIF system, which introduces an addition of 3kV to the nominal 200kV operating voltage of the TEM in order to allow for improved performance of the TEM instrument electron optics even when inelastically scattered electrons associated with atom core-losses are used. The inclusion of the TEM accelerating voltage in the refinement only rendered refinement more complicated and an accurate value for the accelerating voltage should be determined prior to QCBED using the method mentioned above.

3.4 NON-LINEAR LEAST SQUARE FITTING

Non-linear least square fitting routines minimize the objective function S , which measures the difference between observed experimental intensity, I_i^{obs} , and calculated intensity, I_i^{cal} , and is defined as

$$S = \sum_i (I_i^{obs} - cI_i^{cal})^2, \quad (26)$$

where c is a scale factor. By variation of parameters that are relaxed during the refinement, the computer program provides a minimum of S using a modified Marquardt Method [125]. Typically the computer program can find a minimum in less than ten iterations. Assignment of different initial values for various parameters ascertains that the global minimum of S is found consistently.

The goodness of fit (GOF) is evaluated using a weighted reliability factor [125],

$$R_w = \left(\frac{\sum_i \frac{(I_i^{obs} - cI_i^{cal})^2}{\sigma_i^2}}{\sum_i \frac{(I_i^{obs})^2}{\sigma_i^2}} \right)^{\frac{1}{2}}, \quad (27)$$

with the standard deviation for i^{th} point, σ_i . Generally, it holds that $\sigma_i = \sqrt{I_i^{obs}}$. The perfect fit between the observed and the calculated CBED patterns would result in an R_w value that is zero, i.e., when I_i^{obs} is identical to cI_i^{cal} .

3.5 SIMULTANEOUS REFINEMENT OF DW AND STRUCTURE FACTORS

This section explains how simultaneous refinement of DW and structure factors works. $L1_0$ TiAl is used as an example. During the refinement several low order electron structure factors U_g with $h^2+k^2+l^2 < N$ (N depends on the structure and the constituent atoms of the material) are relaxed,

as only low order hkl planes are affected strongly by bonding. High order electron structure factors are approximated using the independent atom model IAM approximation. IAM values for higher order electron structure factors $U_g^{\text{higher order}}$ ($h^2 + k^2 + l^2 > N$) are obtained by application of the Mott formula using IAM X-ray atomic scattering factors

$$U_g^{\text{higher order}} = \frac{\gamma}{C\Omega s^2} \left(\sum_i (Z_i - f_i^{\text{XRD}}) \exp(-B_i s^2) \exp(-2\pi i \mathbf{g} \cdot \mathbf{r}_i) \right), \quad (28)$$

in general, or for L1₀ ordered γ TiAl using the tp2 cell with Ti at (0,0,0) and Al at (0.5,0.5,0.5)

$$U_g^{\text{higher order}} = \frac{\gamma}{C\Omega s^2} \left((Z_{\text{Ti}} - f_{\text{Ti}}^{\text{XRD}}) \exp(B_{\text{Ti}} s^2) + (Z_{\text{Al}} - f_{\text{Al}}^{\text{XRD}}) (-1)^{h+k+l} \exp(B_{\text{Al}} s^2) \right), \quad (29)$$

with $s = g_{hkl} / 2$, Ω = volume of the unit cell, γ = relativistic constant, $C=131.2625$ if Ångstroms are used as a unit, $Z_i = Z_{\text{Ti}}$ and Z_{Al} , the atomic numbers for Ti (22) and Al (13), respectively [49], f_i^{XRD} = X-ray atomic scattering factors $f_{\text{Ti}}^{\text{XRD}}$ and $f_{\text{Al}}^{\text{XRD}}$ for Ti and Al, respectively, and B_i = Debye Waller factors B_{Ti} and B_{Al} for Ti and Al in the L1₀ ordered γ TiAl. In this formulation the DW factors can be interpreted as dampening terms.

While in this approximation for $U_g^{\text{higher order}}$ the X – ray atomic scattering factors are fixed and approximated with readily available IAM values [98], the DW factors B_i are relaxed. Using this formalism allows us to integrate Debye Waller factors into our routine and refine them simultaneously with low order electron structure factors U_g . In total one to ten low order U_g ($h^2 + k^2 + l^2 < N$) electron structure and the Debye Waller factors are relaxed simultaneously.

In order to ensure that a global rather than a local minimum is reached we provide reasonable starting values for the low order electron structure factors and for the Debye Waller factors. Reasonable starting values for Debye Waller factors are obtained from refinements with fixed electron structure factors, which are approximated with IAM values obtained from Eq. 36.

Using these newly obtained starting values for Debye Waller factors and IAM values for low and high order structure factors, the set of low order electron structure factors and Debye Waller factors are refined simultaneously in a subsequent refinement run. Low order electron structure factors are then subsequently converted into X – ray structure factors using Mott formula:

$$F_g^X = Z_{Ti} \exp(-B(Ti)s^2) + (-1)^{h+k+l} Z_{Al} \exp(-B(Al)s^2) - \left(\frac{C\Omega s^2}{\gamma}\right) U_g, \quad (30)$$

The successful refinement of low order electron structure and DW factors from a CBED pattern depends not only on the sensitivity of intensity distribution in the pattern to the changes in low order but also on the sensitivity to changes of high order electron structure factors, as they are used to refine DW factors. Refinement of DW factors alone could lead to systematic errors [128].

3.6 COMPUTATIONAL MATERIALS SCIENCE METHODS

As one objective of this study is to validate different DFT approximations, structure factors were simulated using the commercially available software WIEN2K for the tetragonal binary

intermetallics L1₀ TiAl and FePd. Anisotropic DW factors for L1₀ TiAl have also been simulated using the method described in 2.4.2 to verify our experimental data.

3.6.1 FLAPW based first principle calculations

The DFT calculation based structure factors for L1₀ TiAl and FePd were obtained with the WIEN2K package, which is based on a full potential linearized augmented plane-wave (LAPW) + local orbitals (lo) method [175]. The exchange correlation energy functional was calculated using different approximations of the GGA approach, namely GGA PBE and LDA PW [176, 177]. For each atom species, a muffin tin radius R_{MT} of 2.5 au was used. A modified tetrahedron method was applied to perform the Brillouin – zone integration. A total of 10,000 k points in the unit cell with $R_{MT} * K_{max} = 10$ was used to test convergence.

3.6.2 Molecular dynamics (MD) simulation of DW factors

DW factor simulations were performed using the well-established interatomic potential [172, 178] using methods described in 2.4.2 [169-171]. We used the MD software LAMMPS [171] (<http://lammmps.sandia.gov>) to simulate the trajectory of atoms in γ -TiAl and then calculated the velocity-velocity auto-correlation functions for both atoms along three Cartesian directions. A supercell with 20×20×20 unit cells were created and 500,000 steps with a step size of 1fs were simulated using the semi-empirical potential [172] which was constructed by combining ab-initio calculation and experimental parameters and has been successfully applied to simulate deformation behavior of γ -TiAl [178].

3.7 MULTI-BEAM OFF-ZONE AXIS METHOD

The current study introduces different sample-beam orientations, which provide an effective combination of advantages of the systematic row method, e.g. reasonable computational effort, high-contrast dynamical features in the CBED disc, and the ZAP method, e.g. easy determination of incident beam direction, simultaneous determination of multiple structure factors, and are suitable for quantitative CBED experimentation without the need for an in-column Omega-type energy filtering device equipped TEM instrument. To achieve both high sensitivity for structure factor and DW factor refinement and easily examinable symmetry, CBED patterns are recorded for crystal orientations relative to the incident beam that are within a few Bragg angles of a low-order zone axis orientation with three or more strongly diffracting beams, e. g. multi-beam off-zone axis orientations. Dynamical interaction of four (transmitted and three diffracted beams) or six (transmitted and five diffracted) strongly excited beams restricts and distributes intensity more uniformly among all excited discs, including the transmitted beam or zero-beam disk (Figure 5b), as compared to the case of a symmetric ZAP CBED (Figure 5a). This constitutes a major advantage vis-à-vis to ZAP CBED in which the intensity in the center disc is always much higher as compared to that of the diffracted-beam discs, corrupting intensities in the diffracted discs by background and noise (Figure 5b). Additionally, it has been shown that off-zone-axis patterns are more sensitive to structure factor changes than perfect on-axis ZAP [34, 173]. Nakashima [153] used off-zone axis patterns to illustrate the advantage for improved background subtraction in quantification of CBED pattern intensities and successfully determined structure factors by QCBED without use of an energy filter. However, the method was not applied specifically for simultaneous determination of Debye Waller factors and multiple structure

factors. It was first proposed in this study that this multi-beam off-zone axis method should be used for simultaneous DW and structure factors measurements.

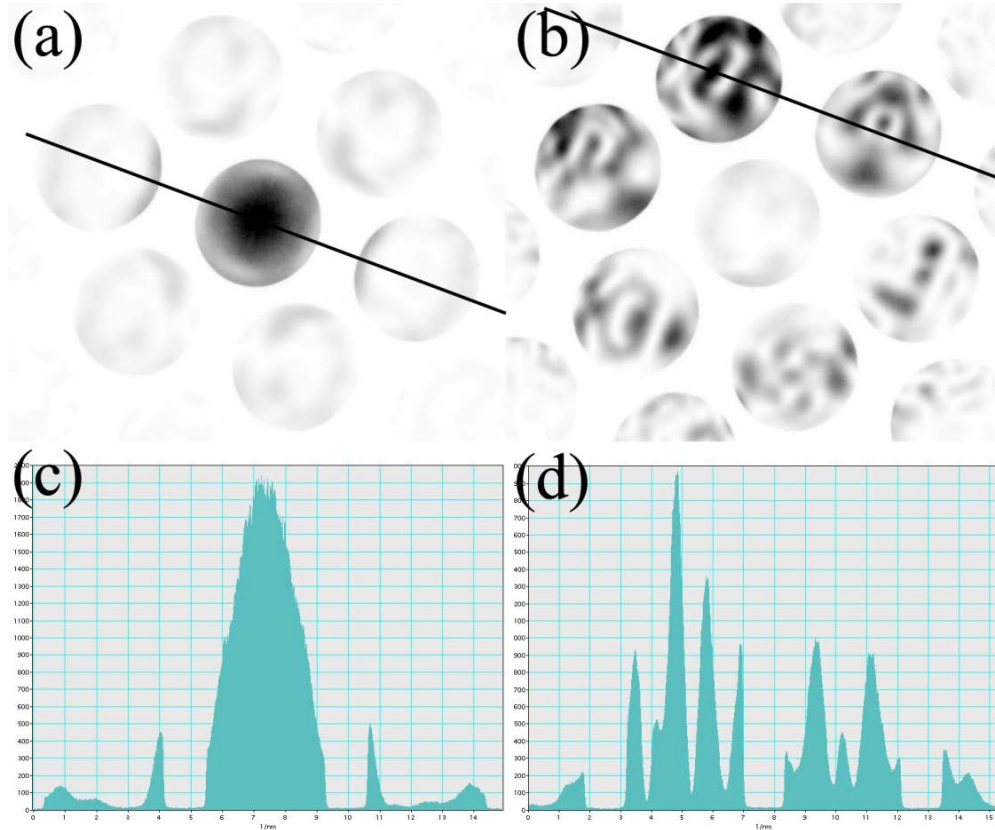


Figure 5 (a) zone axis CBED versus off-zone axis CBED taken near $[101]$ for FePd. (c) and (d) are line profiles along black lines in (a) and (b), respectively.

In the multi-beam off-zone axis method, the exact sample orientation with respect to the incident beam, which is important for the refinement process, can be readily figured out. In patterns obtained from thick regions, Kikuchi bands can be used to index the diffraction pattern and to determine crystal orientation with respect to incident beam. In thinner sample regions, where Kikuchi bands are too weak or absent, features in the CBED discs are used for crystal orientation determination. The symmetry of discs in a multi-beam off-zone axis orientation has

been discussed before, as can be seen in Figure 7 and Figure 10. The mirror-planes and two-fold axes in the excited discs are used for accurate crystallographic orientation determination.

For data extraction from the experimentally acquired patterns coarser features prove to be less sensitive to small misalignment than finer features. Generally, CBED patterns acquired from multi-beam off-zone axis orientations have coarser features than ZAP. In comparison to the ZAP method, the small crystal tilt away from the exact zone axis orientation brings the respective diffracted beam discs in the multi-beam near zone axis method we used very close to or exactly into Bragg conditions, i.e., the associated deviation vector \mathbf{s}_g are small or zero. This renders the contrast features resulting from dynamical beam interactions observed in the diffracted CBED discs to become coarser. The contrast feature periodicity in the disks is approximately proportional to the inverse of the effective deviation vector \mathbf{s}_{eff} , which is given as

$$s_{eff} = \sqrt{s^2 + \frac{1}{\xi_g^2}}, \quad (31)$$

with ξ_g the extinction distance. Then the intensity, I , can be written as

$$I = \frac{1}{v} \left(\frac{\pi}{\xi_g} \right)^2 \frac{\sin^2(\pi s_{eff} t)}{(\pi s_{eff})^2}, \quad (32)$$

A small s_g results in small s_{eff} and concomitantly in an enlarged or coarser periodicity in the contrast feature characteristic of the CBED disc.

Figure 6 shows a number of different sample-beam orientations that constitute four- and six- beam near zone axis orientations. The circles in the reciprocal space lattice sections shown

in Figure 6 schematically represent intersections of the Ewald sphere with the ZOLZ. In each case, when the Laue center is close to the incident or zero beam (always in the center of the schematic reciprocal space lattice section depictions shown in Figure 6), the contrast features in the CBED pattern result from strong interactions between low order reflections among themselves and low order reflections and the transmitted or zero-beam, which makes the pattern very sensitive to the structure factors of excited reflections. For example, in the graphical representation of the diffraction geometries shown in Figure 6(a), the diffracted beams g_{200} , g_{220} and g_{020} are strongly excited simultaneously (circle 1), satisfying their respective Bragg conditions exactly. Therefore, the intensity distributions in the resulting CBED discs are sensitive to $F_{g_{200}}$ and $F_{g_{220}}$. In Figure 6(b), g_{200} , g_{02-2} and g_{22-2} are in exact Bragg condition, while g_{-11-1} and g_{31-1} are near Bragg conditions, rendering these five low order diffraction vectors strongly excited. This orientation enables the simultaneous determination of the structure factors of all five reflections from this one pattern. The interplay of the many beams in these near-zone axis multi beam orientations results in a sufficient number of equations that allow for simultaneous refinement of the DW factors and the structure factors. Conversely, in the systematic row method, only one diffracted beam is strongly excited, which results in an insufficient number of equations to determine simultaneously DW- and structure factors robustly with high sensitivity.

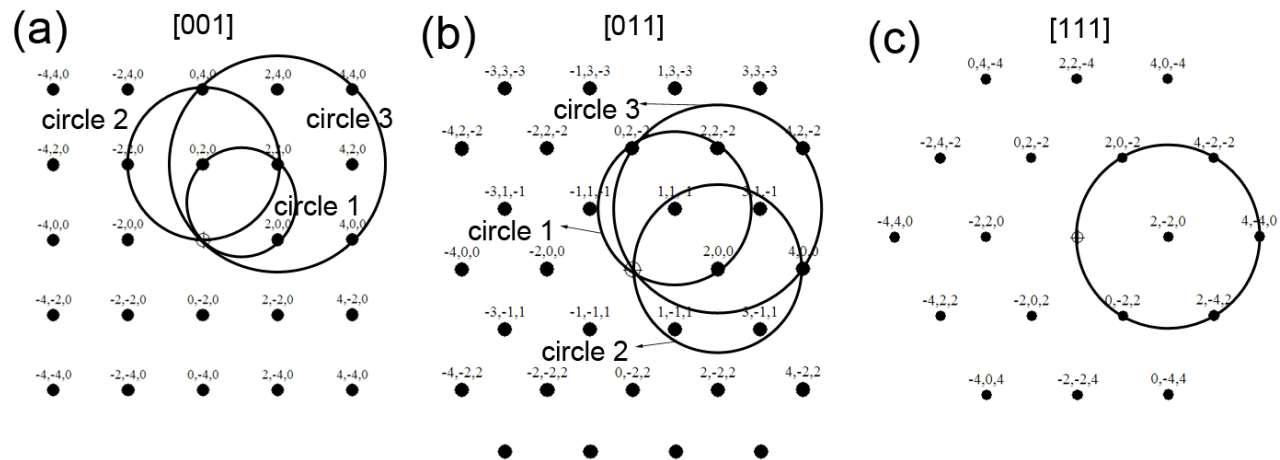


Figure 6 (a) electron diffraction pattern of a FCC structure along [001] zone axis. Circles are traces of intersections between the Ewald sphere and the zero order Laue plane. Two circles indicate beam directions in two four beam conditions respectively. (b) electron diffraction pattern along [011]. (c) electron diffraction pattern along [111].

4.0 DEBYE WALLER FACTORS AND STRUCTURE FACTORS OF SI

In this chapter and next chapters, a robust multi-beam off-zone axis QCBED method to measure DW factors and structure factors, starting with Silicon, to B2 NiAl and L1₀ TiAl and then to L1₀ FePd, will be established. The difficulty lies in the fact that both DW factors and structure factors have to be accurately determined (equation (13)). As mentioned in 2.3.2.4, the three widely-used CBED methods do not satisfy the stringent requirement for our measurement of transition-metal based intermetallics.

This section presents and discusses the application of the new multi-beam off-axis QCBED method for the accurate and precise simultaneous measurement of multiple structure factors and DW factors for Si. This section of the dissertation document is based on a manuscript published in *Acta Crystallographica A* 66, (2011) p685 entitled “Determination of Debye Waller Factor and Structure Factors for Si by Quantitative Convergent Electron Beam Diffraction using off-axis Multi-Beam Orientations”, by X. H. Sang, A. Kulovits and J. M. K. Wiezorek.

In this chapter, Si, which has a cubic structure and one nonequivalent atomic position with only one unknown DW factor, is used to describe basics of the off-axis multi-beam method, because it provides an excellent material for benchmarking of the new method, e. g., it has been characterized experimentally and theoretically and both XRD and CBED measurements have been reported [33, 34, 46-48]. In the next chapter, we will investigate B2 NiAl, which also has a

cubic structure, comprised of two nonequivalent atom positions and two unknown DW factors. As more DW factors are included in the refinement, more elaborate QCBED method is needed as compared to the case of an elemental crystal, e.g. Si. After enough experience on QCBED was accumulated, in chapter 7.0 and 8.0, we then investigated $L1_0$ TiAl and FePd, which have a tetragonal structure and two nonequivalent atomic positions with four unknown DW factors. In chapter 6.0 a theoretical explanation why our method is superior to the previous methods will be presented.

Crystalline silicon is a face cubic centered (FCC) structure that belongs to the space group $Fd\bar{3}m$ (227) with a motif of two symmetrically equivalent atoms situated at 0,0,0 and $\frac{1}{4}, \frac{1}{4}, \frac{1}{4}$. The lattice parameter used in this work is 0.357 nm. DW-factors, structure factors and bonding properties of Si have been widely investigated by various methods, mainly because low defect concentration, single crystalline silicon is relatively readily available and both X-ray and electron diffraction experiments yielded accurate results. Structure factors have been measured by [47] using the X-ray Pendellösung method at liquid nitrogen temperature and room temperature. Quantitative CBED measurements on Si have been attempted using the ZAP method [33] and the systematic row method [131]. DW-factors were theoretically calculated by [179] in a temperature range from 1 K to 1000 K. Hence, Si is used in this study to evaluate the accuracy of our CBED method, as the obtained results can be readily compared with previously reported data.

To evaluate the accuracy of the multi-beam near zone axis orientations, zero-loss filtered CBED patterns have been acquired for single crystals of Si (space group $Fd\bar{3}m$, no. 227) using a post-column energy-filtering device attached to a field-emission gun equipped TEM instrument and DW factors and structure factors have been measured for sample temperatures of -

177°C \approx 96K, -100°C \approx 173K and room temperature, 27°C \approx 300K, including those used in previous reports and adding one new temperature. Also, ZAP CBED experiments have been performed for Si. Results of the refinements for DW factors and structure factors obtained from the multi-beam near zone axis CBED method experiments for Si are compared with those from ZAP CBED experiments performed here and those reported in previous studies.

4.1 RESULTS: DEBYE WALLER AND STRUCTURE FACTORS OF SILICON

4.1.1 Multi-Beam Diffraction Conditions

Figure 6 shows possible and important multi-beam off-zone axis conditions for the FCC structures. Changing the crystal orientation such that the Laue center moves far away from the incident beam at the center of the reciprocal space lattice section shown in Figure 6, the intensity distributions in the resulting CBED disks becomes more sensitive to DW factors, as then only higher order \mathbf{g} -reflections interact strongly with each other and are in exact Bragg condition. The structure factors of high order reflections can be approximated much better than low-order reflection structure factors by values based on free atom data during the initial iterations of refinement of experimental data sets. Here, our approach is to use the four-beam conditions schematically described schematically by circle 2 in Figure 6 (a) for the FCC-lattice to determine DW-factors and to use the four-beam conditions illustrated by circle 1 in Figure 6 (a) to refine simultaneously multiple low-order structure factors. Due to the presence of glide-plane symmetry for Si reflections, $hkl = \mathbf{g}_{hkl} = \mathbf{g}$, satisfying the extinction condition $h+k+l = 4n + 2$, with n an integer equal or larger than zero, are structurally forbidden or extinct. The four-beam

diffraction condition used here for structure factor refinement is therefore associated with excitation of g_{220} , g_{2-20} and g_{400} in Si (=condition I). Tilting the crystal even further away from the perfect [001] zone axis orientation (Laue circle center coincident with the incident beam direction) the four-beam condition for which g_{400} , g_{040} and g_{440} are excited is attained, which was used for the DW-factor determination (=condition II).

4.1.2 Experimental Results

4.1.2.1 Si DW factor

Near [001] zone axis CBED patterns in conditions I and II (Figure 6) were recorded for Si at -177°C \approx 96 K, -100°C \approx 177 K and room temperature 27°C \approx 300 K. At each temperature CBED patterns were collected for a range of different sample thicknesses. The CBED patterns obtained for the diffracting condition II (Figure 6) were used to determine DW-factors of Si at these temperatures and a typical example pattern is shown in Figure 7. Two-dimensional intensity data was extracted from the CBED discs for g_{000} , g_{040} , g_{-400} and g_{-440} . Every pattern in condition II was refined using fixed structure factors based on free atom values and relaxing the DW factor. The results for the CBED experiments performed at different temperatures and sample thicknesses are summarized in Figure 8. Examples comparing the experimental and calculated CBED disks for the zero-beam, 000, and the diffracted beams, 040, -400 and -440, used in the refinement for the DW-factors are shown in Figure 9.

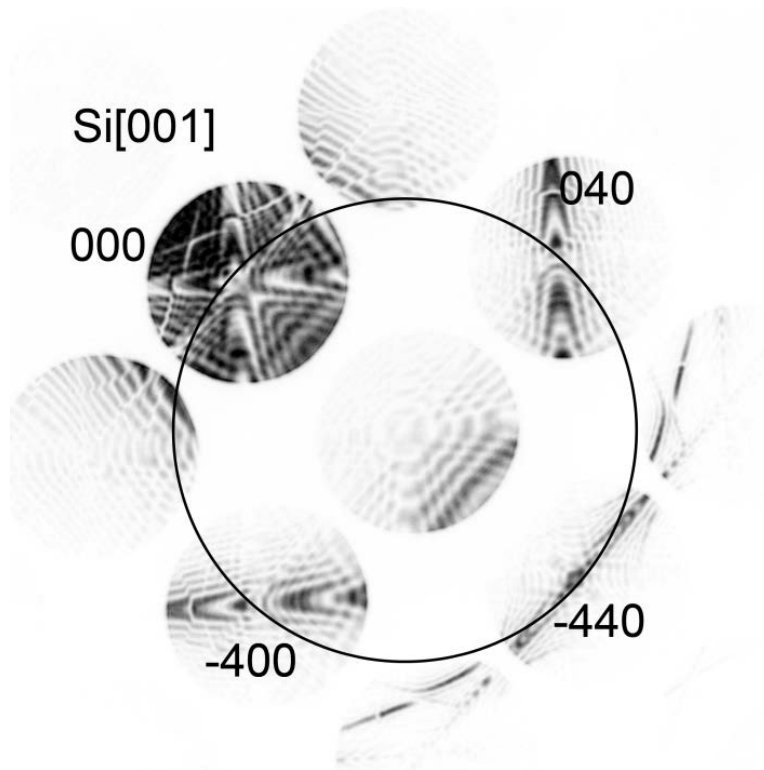


Figure 7 A condition II Si - CBED pattern obtained at -177°C . Refinement yielded a thickness of 343.5nm. The white circle indicates the trace of the intersection of the Ewald sphere on ZOLZ plane.

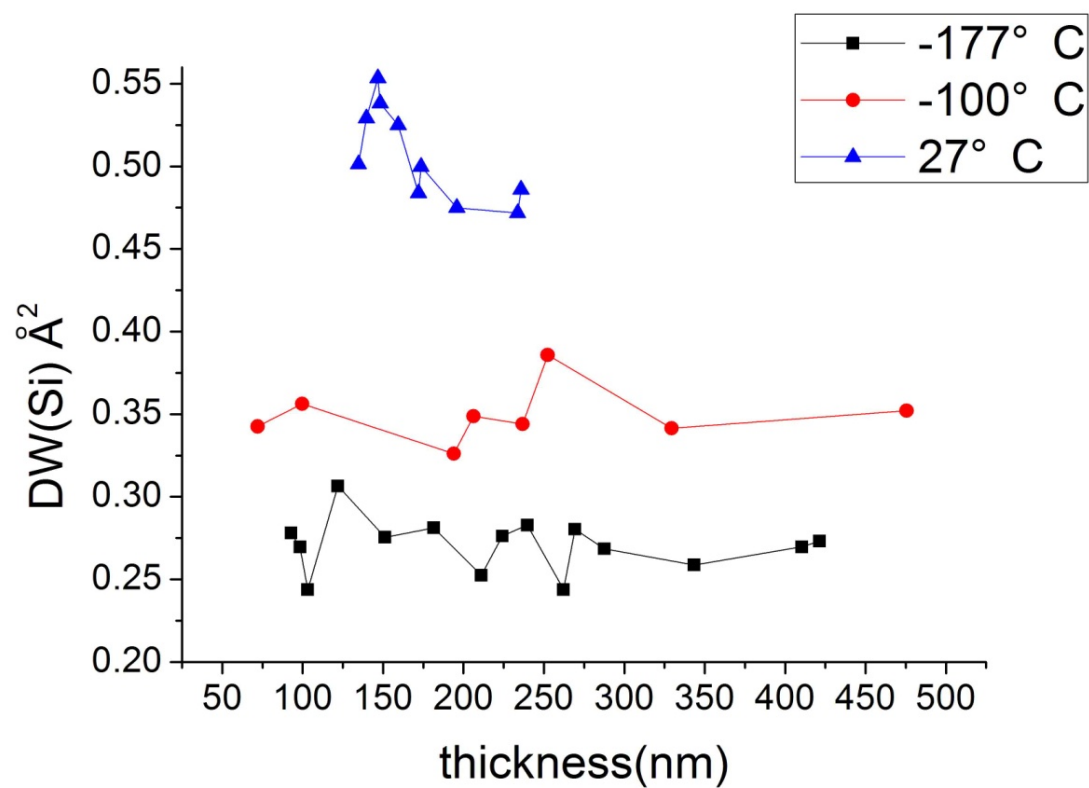


Figure 8 Refinement results for Si DW factors for different sample thickness at different temperatures.

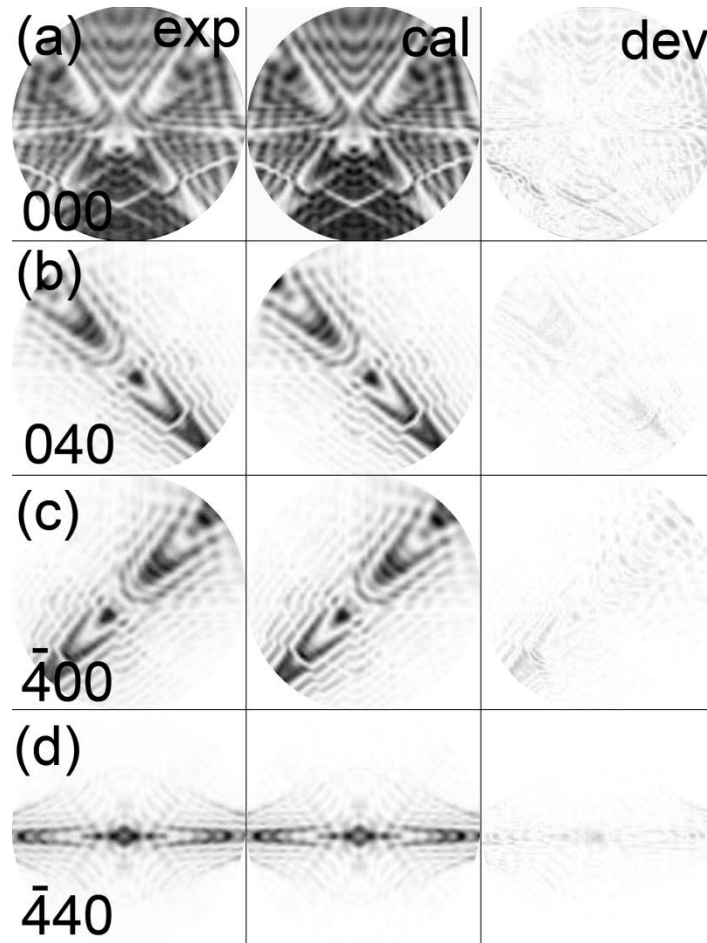


Figure 9 Comparison between simulated disks and experimental disks after refinement for the pattern shown in Figure 7.

At the lower temperatures (-177°C and -100°C) the DW-factors exhibit very small scatter (Figure 8). With increasing sample thickness the signal-to-noise ratio in the CBED data increases, because the influence of residual surface contamination on the dynamical diffraction data decreases, which improves the accuracy of the refinements. The DW factors converge to an average value for each temperature as the thickness increases. The refined DW-factor values are systematically higher than the average for sample thicknesses less than 160nm in the data obtained at room temperature. This can be attributed to surface contamination effects on the quality of experimental CBED data. At room temperature the contamination rate is increased

relatively to the lower temperature experimental conditions, increasing the uncertainty of DW-factor measurements Figure 8 for sample thicknesses less than 160nm. The scatter of the refined values for the DW-factors at room temperature also tends to decrease as the thickness increases. At room temperature we could not acquire CBED patterns of sufficient quality for inclusion in the refinements from sample thicknesses in excess of 240nm, because detrimental TDS contributions become intolerable for Si. Averaging our measurements for the different sample thicknesses yields the values and standard deviations for Si DW-factors for the three different temperatures as summarized in Table 2. These values agree well with theoretical values and other experimental measurements for the measurements below room temperature. The discrepancy between the room temperature DW-factor reported by Ogata et al. and Zuo et al. and our data becomes negligible (less than 2%) after we reject the data obtained for sample thicknesses, t , below 160 nm, which may have been affected significantly by contamination during the CBED experimentation (Table 2).

Table 2 Comparison between experimental and theoretical Si DW factor

Temperature	Fitted Si DW factor and standard deviation (\AA^2)	Theoretical DW factor (\AA^2) [179]	(Ogata <i>et al.</i> , 2008) [34] (\AA^2)	(Saunders <i>et al.</i> , 1995) [33] (\AA^2)	(Zuo <i>et al.</i> , 1997) [13] (\AA^2)
-177°C	0.2707±0.0162 ($\pm 6\%$)	0.2446		0.26 (-180°C)	
-100°C	0.3476±0.0171 ($\pm 5\%$)	0.3417			
27°C, $t > 160$ nm	0.4833±0.0110 ($\pm 2\%$)	0.5275	0.463		0.4668

4.1.2.2 Si structure factors of the 220 and 400 reflections

For Si structure factor refinement CBED patterns were acquired under condition I for different thicknesses at -177°C and -100°C . An example of a typical CBED pattern taken under condition I is shown in Figure 10.

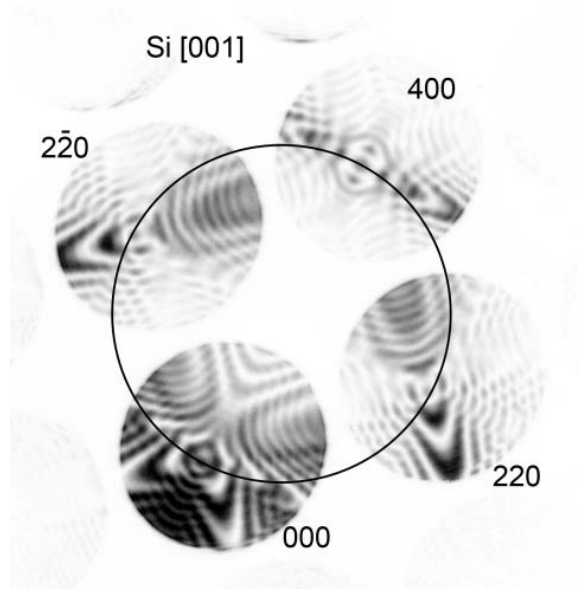


Figure 10 A Si CBED pattern acquired using condition I at -100°C . T Refinement yielded a thickness of 371.6nm . The black circle indicates the trace of the intersection of the Ewald sphere on ZOLZ plane.

Pattern refinements were accomplished by relaxing $F_{g_{220}}$ and $F_{g_{400}}$ while using the DW-factors determined experimentally here. We included 223 exact beams in the Bloch wave calculation without using the Bethe approximation. Si is a covalently bonded material and shows only relatively small charge transfer. Previous measurements [47] have shown that the deviation of X-ray structure factors $F_{g_{220}}$ from those obtained for the free atom model due to covalent bonding is on the order of 1 percent. This small amount of change has minute influence on the intensity distribution in the CBED discs of the structurally allowed reflections. Hence, any

method applied to determine structure or DW-factors experimentally requires accuracies about an order of magnitude smaller than this small 1% change in the intensity due to the covalent bonding in Si.

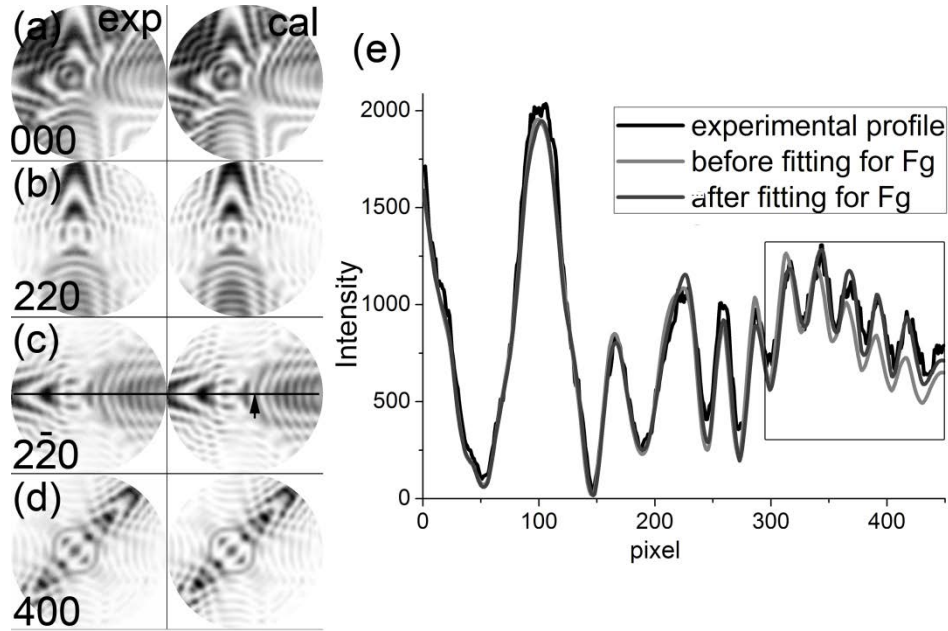


Figure 11 Comparison between simulated discs and experimental discs after fitting for the pattern shown in Figure 10. $R_w = 0.136$ after refinement. (e) intensity profiles along the black line trace in (c) pointed by an arrow for experimental disk, simulated disc based on free atom data and simulated disc after structure factor refinement.

Figure 11(e) illustrates that almost the entire profile can be approximated by the free atom model (the gray line), except for the region enclosed in the black square, where the intensity predicted by the free atom model is notably lower than the intensity observed experimentally. Figure 11(e) clearly demonstrates that the four-beam method utilized here is highly sensitive to changes in F_g and suitable to detect the smallest differences between the true F_g of the structure and approximated F_g values. The refined values of F_{g220} and F_{g400} are plotted versus sample thickness at -177°C and -100°C in Figure 12.

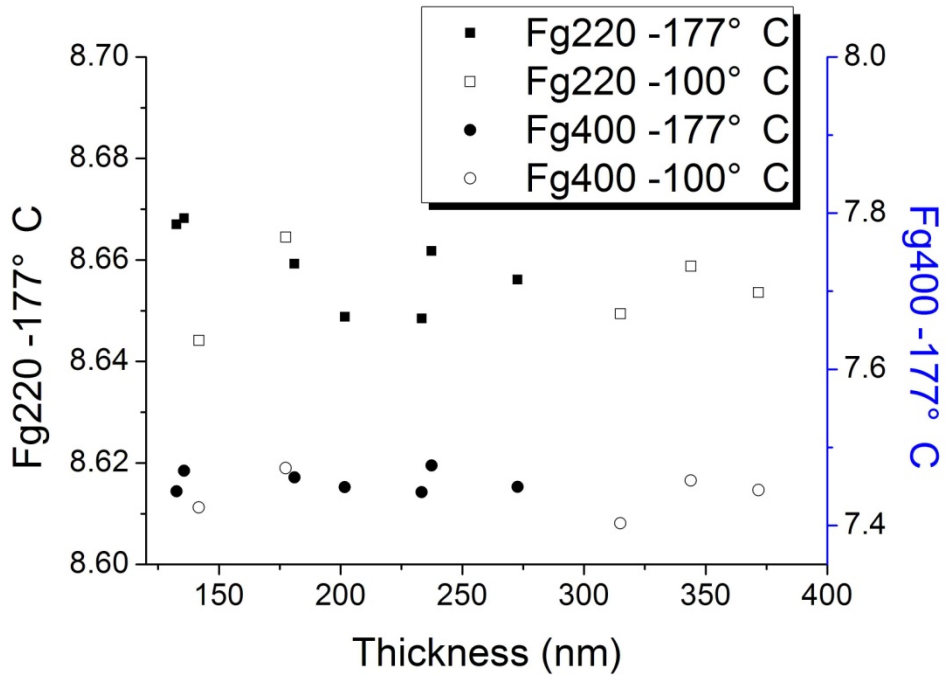


Figure 12 Refinement results of Silicon structure factors Fg_{220} and Fg_{400} from different sample thickness at different temperatures.

We converted the electron structure factors to X-ray structure factors using the Mott formula. As the thickness increases the structure factors tend to converge. A similar trend was observed during DW-factor refinement and residual surface contamination is a possible cause for it. The standard deviation for structure factors during each refinement is small as compared to deviations observed in separate refinement attempts. Hence, we report here the statistical errors in terms of the equivalent of one standard deviation. The average values and errors

corresponding to one standard deviation, which is $s = \sqrt{\frac{1}{N-1} \sum_{i=1}^N (x_i - \bar{x})^2}$, are calculated and for

Fg_{220} and Fg_{400} listed in Table 3 together with values from prior reports. The results reported here are consistent with previously reported values.

Table 3 Comparison between experimental and theoretical Si structure factors $F_{g_{220}}$ and $F_{g_{400}}$

Structure Factor	Present work at -177°C	Present work at -100°C	(Aldred & Hart, 1973)[47]	(Teworte & Bonse, 1984)[48]*	(Ogata et al., 2008)[34]**	Free atom
F(220)	8.659±0.008	8.654±0.008	8.651	8.682	8.685	8.712
F(400)	7.456±0.013	7.440±0.028	7.444	7.446	7.478	7.511

* DW factor is set to be 0.4\AA^2 to convert it to X-ray scattering factor per Si atom; ** DW factor is set to be 0.463\AA^2 to convert it to X-ray scattering factor per Si atom;

4.2 DISCUSSION

4.2.1 Multi beam near zone axis method

4.2.1.1 Sensitivity of this new method to DW factors

We took patterns under different conditions to compare the sensitivity of our method and other two commonly-used methods, namely excited row method and HOLZ method. The changes of line profiles with the change of the DW factor under different conditions are shown in Figure 13(d, e, f). It can be seen that the line profile from pattern under multi-beam condition changes dramatically as the DW factor changes while line profiles from the other conditions change to a very limited amount. This is reflected in Figure 13(g), which shows that the multi-beam condition gives the most pronounced minimum in the R_w vs. DW factor curve.

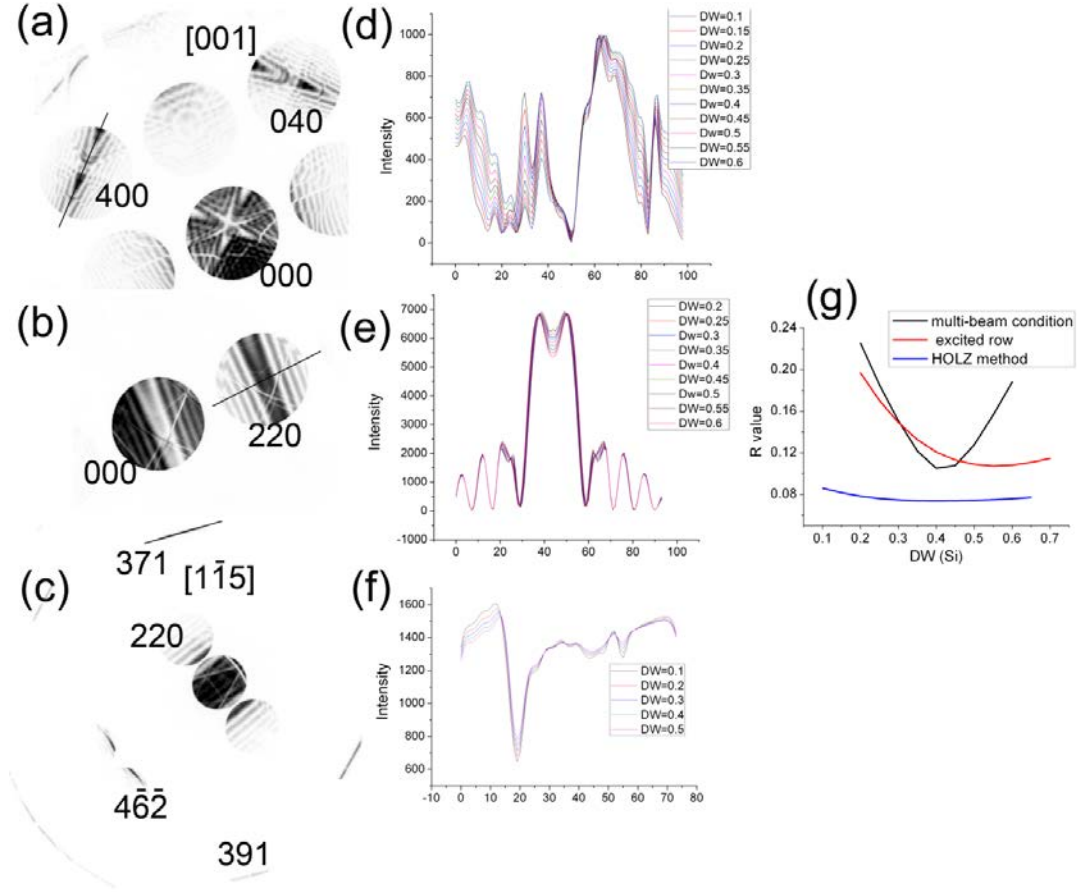


Figure 13 Multi-beam method (condition II) & corresponding profile (a) &(d), excited row pattern and corresponding profile (b) & (e), HOLZ method and corresponding profile (c) & (f). R_w vs. DW factor (g).

4.2.1.2 Intensity Sensitivity with changes in structure factor F_g

The systematic row CBED pattern method has been known as sufficiently sensitive for refinement of the structure factor F_g of the excited beam in the two-beam condition. Accurate Bloch wave solutions have been determined [49]. When the excitation error s_g is zero, the intensity of the transmitted beam, I_0 , can be written as [49],

$$I_0 = \cos^2\left(\frac{\pi |U_g|}{K_n}\right), \quad (33)$$

with K_n the wave vector component in beam direction, U_g the structure factor of the excited beam g , and t is the thickness. The partial derivative of I_0 with respect to structure factor U_g is given as,

$$\frac{\partial I_0}{\partial U_g} = -\frac{\pi}{K_n} \sin\left(\frac{2\pi |U_g|}{K_n}\right), \quad (34)$$

For a four-beam condition with a sample–beam orientation such that the Ewald sphere intersects the ZOLZ at circle 1 in Fig.1a, g_1 , g_2 and g_3 are excited. g_1 and g_2 have the same structure factor U_g , and the structure factor of g_3 is U_m . When s_{g_1} , s_{g_2} and s_{g_3} are all zero, the exact solution of intensity of transmitted beam can be written as [142],

$$I_0 = \frac{3}{8} + \frac{1}{8} \cos\left(\frac{4\pi |U_g|}{K_n}\right) + \frac{1}{2} \cos\left(\frac{2\pi |U_m - U_g|}{K_n}\right), \quad (35)$$

From equation (35) follows the derivative of I_0 with respect to structure factor U_g :

$$\frac{\partial I_0}{\partial U_g} = -\frac{2\pi}{K_n} \sin\left(\frac{4\pi |U_g|}{K_n}\right) - \frac{\pi}{K_n} \sin\left(\frac{2\pi |U_m - U_g|}{K_n}\right), \quad (36)$$

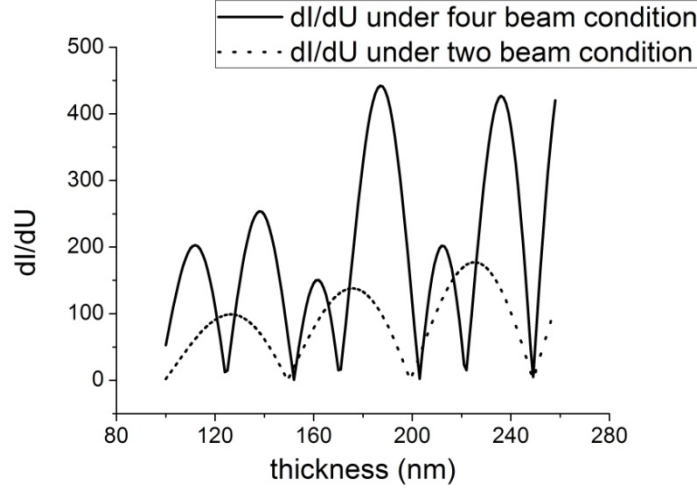


Figure 14 Plot of $\frac{\partial I_0}{\partial U_g}$ at different beam conditions for different thickness.

$\frac{\partial I_0}{\partial U_g}$ has been plotted for different thickness for both the two-beam condition and the multi-beam orientation of condition I for Si (Figure 14). U_g is set to be 0.04\AA^{-2} and U_m is 0.024\AA^{-2} . K_n is calculated using an accelerating voltage of 200kV. Figure 14 shows that generally the intensity for the four-beam condition is more sensitive to changes in structure factor than for the two-beam condition. It is also discernible that with increasing thickness the magnitude of $\frac{\partial I_0}{\partial U_g}$ increases. CBED patterns from thick areas are more sensitive to structure factors. However, CBED patterns from thick area are also always noisy and exhibit diminished contrast, due to high absorption and also potential defect content in the scattering volume of the material. As there are no analytical solutions for the ZAP method [142] it could not be included in this part of the discussion. While the ZAP method might also be very sensitive to changes in structure factor, the treatment of the background and the differences in intensity distribution in

the center disc as compared to the diffracted discs at higher scattering angle compromise the precision and accuracy that can be attained in the ZAP method, which is reflected in the typically large R_w values that obtain (Table 4).

Table 4 Comparison of R_w for Si structure factor refinement with the ZAP CBED method and the multi-beam near zone axis CBED method according to condition I (Figure 10).

Si	Thickness [Å]	R_w using free atom model	R_w $F_{g_{220}}$ is relaxed	R_w $F_{g_{220}}$ and $F_{g_{400}}$ are relaxed
Room temperature, zone axis pattern	1437.10	0.241	0.235	0.231
	2228.98	0.217	0.210	0.209
	2725.49	0.289	0.283	0.281
Room temperature, condition I	2001.58	0.181	0.170	0.169
	1718.33	0.187	0.181	0.179
	1407.29	0.184	0.178	0.177
Liquid nitrogen temperature, condition I	1324.98	0.152	0.147	0.145
	1354.87	0.139	0.131	0.129
	1809.41	0.135	0.122	0.119

4.2.1.3 R_w value

R_w value is used here to evaluate goodness of the fit. Smaller R_w values correspond to increased reliability and reduced uncertainty of the refinement result. We have performed ZAP CBED experiments for comparison with the multi-beam near zone axis CBED method in order to provide a direct comparison regarding the goodness of fit and robustness of the refinements of structure factors. The results of this comparison are summarized in Table 4. Table 4 shows that R_w is in general significantly higher for ZAP CBED as compared to the four-beam condition. In ZAP CBED, the intensity of the transmitted beam is orders of magnitude larger than for the diffracted beams, unless the pattern is recorded in a very thick region. Hence, ZAP CBED data

sets are subjected to noise and Kikuchi bands, which makes the background subtraction difficult. Even though the intensity distributions in discs affected by Kikuchi bands and noise are corrupted, those discs still have to be included in the refinement as the intensity distribution in the center disk alone does not provide sufficient information for robust refinements of the structure factors and DW-factors. Conversely, in the multi-beam (four-beam or six-beam) conditions, the intensity is evenly distributed between the transmitted and the respective diffracted beams. Every disc contains sufficient intensity to reduce the usually detrimental influence of noise and inelastic scattering. Therefore the magnitudes of R_w can be significantly reduced if CBED patterns are obtained in this type of multi-beam near zone axis orientations. Cooling the sample to liquid nitrogen temperature results in further improvement of the goodness of fit, i.e., a reduction of the R_w (Table 4).

4.2.1.4 Beam selection

Although multi-beam near zone axis CBED patterns orientations are more sensitive than zone axis pattern or two-beam conditions regarding structure factor changes, it was found in this work that it can be disadvantageous to include all diffracted beams into the refinement. Generally in the ZAP as well as the multi beam near zone axis method not every disc is sensitive to structure factor changes. The inclusion of structure factor insensitive discs into the calculation can introduce large errors rendering the refinement useless. While it can prove rather difficult in the ZAP method to find criteria to determine which beams to include and which to discard, the selection criterion for the multi-beam near zone axis method is relatively straightforward. Strongly diffracting beams with $s = 0$ interact strongly with each other and the transmitted beam and are very sensitive to changes in structure factor. Diffracted beams with large deviation

vectors \mathbf{s} that interact only very weakly with all the other beams can be quite insensitive to structure factor changes. Inclusion of diffracted beams with large s can increase R_w from 0.15 to 0.4. Hence, only discs that fulfill the Bragg condition should be included in the refinement.

4.2.2 DW and structure factor determination of crystalline Si

The multi-beam near zone axis method has been successfully applied to determine low order structure factors and DW-factors for Si at three different temperatures. Table 2 shows very good agreement between the measured DW factors and theoretically estimated values at the three different temperatures [179]. The experimentally determined DW-factors have subsequently been used to refine the structure factors for the 220 and 400 reflections. Table 3 shows that structure factors obtained at different temperatures are consistent and in good agreement with literature results [47, 48]. These experimentally obtained results for crystalline Si demonstrate that the multi-beam near zone axis CBED method has successfully been applied to obtain quantitative values for structure and DW factors. This result shows that the multi-beam near zone axis CBED method is accurate and sensitive enough to allow structure and Debye Waller factor refinement with less than 1% error, which is a requirement for electronic structure determination to probe effects of bonding. Hence, results obtained by this method are suitable for experimental electronic structure determination.

4.3 CONCLUSION

In this section, we described the application of a multi-beam near zone axis CBED method, a modified zone axis CBED method, to improve the accuracy of determination of DW-factors and multiple structure factors. By selecting four-beam conditions near the [001] zone axis, we successfully determined DW-factors at three different temperatures ($B(\text{Si})=0.2707 \text{ \AA}^2$ at -177°C , $B(\text{Si})=0.3476 \text{ \AA}^2$ at -100°C and $B(\text{Si})=0.5063 \text{ \AA}^2$ at 27°C) and the $F_{g_{220}}$ (8.659 at -177°C and 8.654 at -100°C) and $F_{g_{400}}$ (7.456 at -177°C and 7.440 at -100°C) structure factors with very high accuracy. We thereby successfully verified the validity of the method for fcc Si.

5.0 DEBYE-WALLER FACTORS AND STRUCTURE FACTORS OF NIAL

This chapter presents and discusses the application of the new multi-beam off-axis QCBED method for the accurate and precise simultaneous measurement of multiple structure factors and DW factors for β -NiAl with the B2 (CsCl type) structure in Strukturbericht notation. This section of the dissertation document is based on a manuscript published in *Acta Crystallographica A* 66, (2010) p694 entitled “Simultaneous determination of highly precise Debye-Waller factors and structure factors for chemically ordered NiAl” by X. H. Sang, A. Kulovits and J. M. K. Wiezorek.

β -NiAl has a simple cubic structure, which belongs to the space group Pm3m (221). The unit cell of β -NiAl contains one Ni atom at 0, 0, 0 and one Al atom at 0.5, 0.5, 0.5 and has a lattice constant $a = 2.8863\text{\AA}$. In chemically ordered structures of metal species DW factors have to be determined for each atom species, which requires more stringent criterion to select orientations that ensure sensitivity of the pattern to multiple DW factors.

The temperature dependence of DW factors of β -NiAl has been previously investigated theoretically by [60], and experimentally by [52, 54] measuring CBED patterns at 110K and by XRD experiments at room temperature by [97]. The theoretical and combined experimental studies report that a cross-over temperature exists for β -NiAl, below which the amplitudes of thermal vibrations of Al exceed those of Ni, and above which the inverse holds. Namely, above the cross-over temperature the thermal vibration amplitude of Ni has been found to be larger than

those of Al. The prior works of [54, 60, 97] determined the cross-over temperature at about 140K. However, from Debye temperature data [180] a cross-over temperature of 90K can be deduced. Here the highly accurate and robust off-zone axis multi-beam CBED method has been applied to determine DW factors of β -NiAl for various temperatures ranging from room to liquid nitrogen temperature. This CBED experimentation enabled a more accurate determination of the cross over temperature, which we present and discuss in this study.

5.1 RESULTS

5.1.1 Orientation selection – sensitivity to structure factors

A beam-sample orientation that has high sensitivity to DW factors and structure factors is essential for successful and robust simultaneous refinements of both factors. Four different orientations near [001] zone axis were acquired and tested for stability of the refinements. The first beam-sample orientation is a zone axis orientation (Figure 15 (a)). The second orientation (Condition I) is a multi-beam near zone axis orientation, where the crystal is tilted such that the Ewald sphere intersects the transmitted beam and the reflections g_{100} , g_{110} and g_{010} , i.e., the transmitted beam and g_{100} , g_{110} and g_{010} are excited (Figure 15 (b)). The third orientation (Condition II) is a multi-beam near zone axis orientation with excited transmitted beam, g_{110} , g_{1-10} and g_{200} (Figure 15 (c)). Condition III is a multi-beam near zone axis orientation with excited transmitted beam, g_{200} , g_{020} and g_{220} excited (Figure 15 (d)). All test patterns were recorded at 100K.

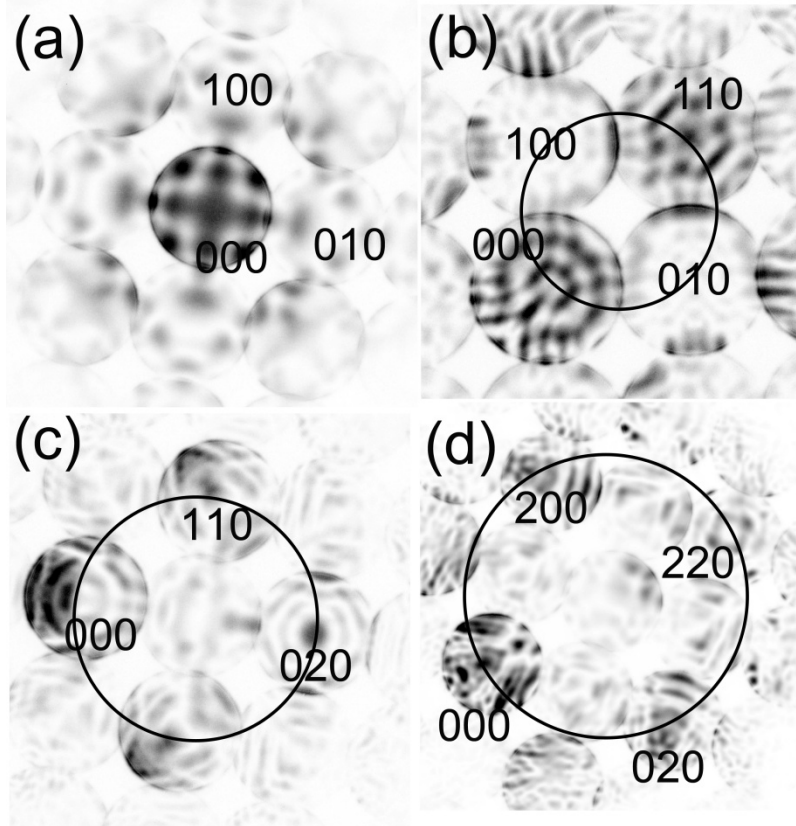


Figure 15 Inverted CBED patterns along different orientations. Black circles are traces of Ewald sphere for each orientation.

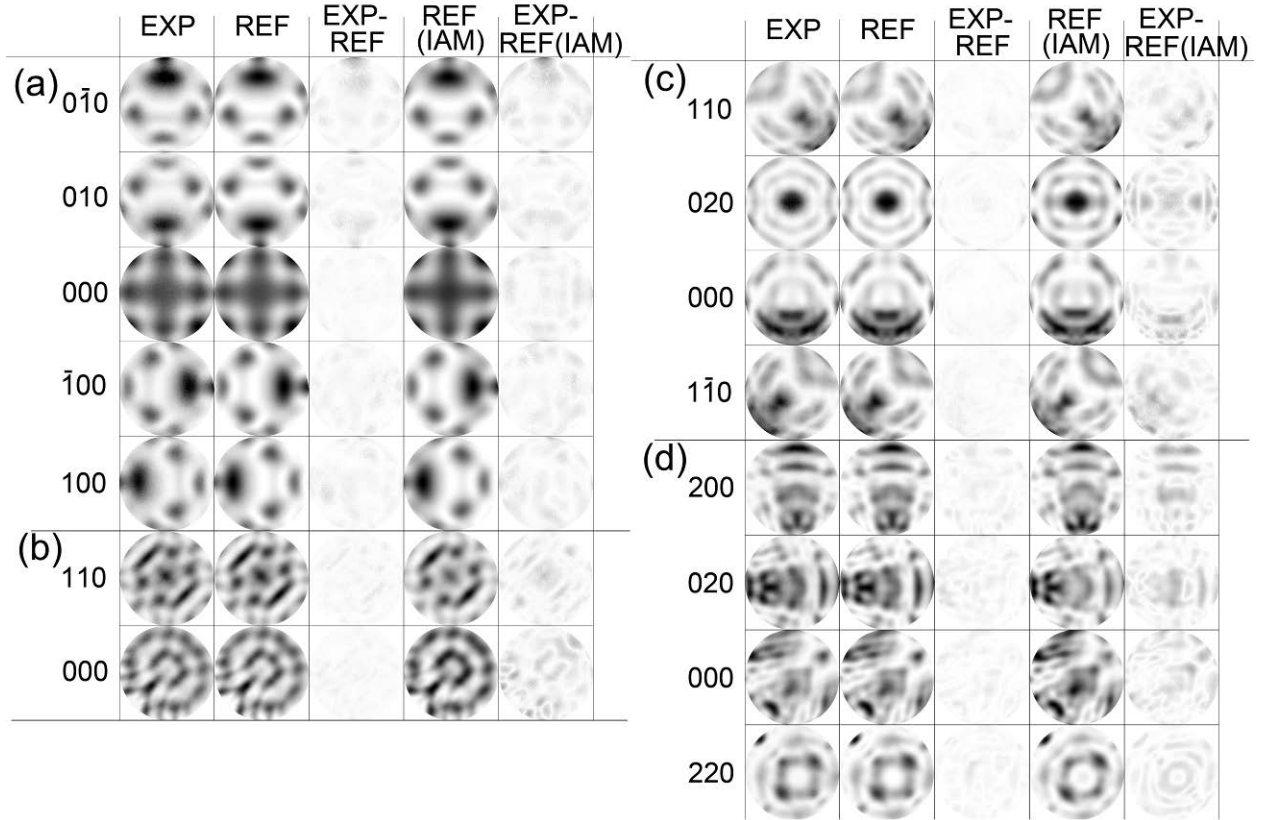


Figure 16 Refinement results of patterns recording at different orientations. The first column in each part shows experimental disks. The second column shows calculated disks by relaxing structure factors and DW factors. The fourth column shows calculated disks by only relaxing DW factors and assuming IAM. The third column and the fifth column show absolute value of deviation between column1 and column 2, and between column 1 and column 4, respectively.

Figure 16 shows the refinement results obtained from the patterns in Figure 15. Figure 16 (a) shows the results for the zone axis orientation in Figure 15 (a). For ZAP patterns, data points in $0\bar{1}0$, 010 , 000 , $\bar{1}00$ and 100 discs are compared with results of Bloch wave calculation. Each disc contains 144471 data points. Refinement of each pattern was implemented by relaxing DW factors B_{Ni} and B_{Al} , structure factors of reflection 100 , 110 and 200 . Reflections for which excitation errors of less than 0.06\AA^{-1} are used as exact beams in the Bloch wave calculation. Reflections whose excitation errors are between 0.06\AA^{-1} and 0.09\AA^{-1} are included in the

calculation using the Bethe approximation [49]. Approximately 145 exact beams and 75 Bethe beams are included depending on slight changes in beam-sample orientation. This number of beams is too small for accurate refinements but sufficient to test goodness of beam-sample orientations. For more accurate refinement of DW factors and structure factors, many more beams (approximately 220 exact beams and 220 Bethe beams) are included in the refinement, which results in longer calculation times. Relaxation of higher reflections, such as 210, in the refinement does not improve the result. It increases the probability that the refinement result gets trapped in a local minimum rather than converging to the global minimum. The accelerating voltage was determined to be around 203kV using HOLZ lines method [174]. The thickness of investigated area was determined as 146.6nm.

Figure 16 (b-d) show results of the refinements for the multi-beam near zone axis conditions in Figure 15 (b-d) respectively. The disc selection for multi-beam near zone axis conditions is straightforward. Discs that are intersected by the Ewald sphere should be included in the refinement as those beams strongly interact with the transmitted and the other diffracted beams with $s \approx 0$. Furthermore the intensity in those discs is higher as compared to discs with large deviations and far from zero, $s \neq 0$.

For condition I (Figure 16 (b)) data points in 000 and 110 disks are used for comparison between experimental data and simulated data. Each disc contains 202055 data points. 100 and 010 discs are not included as the signal-to-noise-ratio in both discs is insufficient for accurate refinements. Patterns were refined by relaxing DW factors B_{Ni} and B_{Ai} and structure factors of reflection 100,110 and 200. The thickness of that area is 217.2nm. For condition II (Figure 16 (c)) data points in the 000, $\bar{1}10$, 110 and 200 discs are included in the refinement. Each disk

contains 138143 data points. DW factors B_{Ni} and B_{Al} and structure factors of the 100, 110 and 200 reflections are relaxed during refinement. The thickness of that area is 207.7 nm. For condition III (Figure 16 (d)), data points in 000, 200, 020 and 220 discs are used in the refinement. Each disk contains 87811 data points. DW B_{Ni} and B_{Al} and structure factors of reflections 100, 110, 200, 220 and 310 are relaxed during refinement. The thickness of that area has been determined as 173.2nm.

In Figure 16 the first column shows the \mathbf{g} vectors of the discs displayed in the following columns. The second column in Figure 16 shows the intensity distribution of the \mathbf{g} -discs corresponding to the respective \mathbf{g} -vectors indicated in the first column. The third and fifth columns in Figure 16 show the calculated intensities of the respective \mathbf{g} -discs using refinement optimized DW and structure factors and the calculated intensities using the independent atom model (IAM), respectively. The comparison with the IAM simulations was included in this figure to illustrate the effect of bonding on the intensity distribution in the experimentally acquired and refined discs. The fourth and sixth columns of Figure 16 show the absolute deviations of intensities in the experimental and the refined discs and experimental and IAM based disc intensities. Comparison of columns three with five shows a vast improvement in the CBED intensity matching when using the optimized DW and structure factors instead of using the IAM values. The discs in column three in Figure 16 (b) and (c) are almost featureless, exhibiting nearly uniform white contrast after the refinement, whereas little improvement can be seen in Figure 16 (a). This improvement is also reflected in changes in the R_w values. The R_w values for calculations based on the IAM model for the different crystal orientations and CBED methods are (a) 0.186, (b) 0.232, (c) 0.364 and (d) 0.296. After refinement R_w values improve to 0.150, 0.110, 0.136 and 0.154, respectively. The smallest improvement was achieved in the zone

axis orientation (Figure 16 (a)), while the orientation in condition II (Figure 16 (c)) showed the biggest improvement. Hence, condition II is most sensitive to changes in structure factors. Condition III shows the least improvement among the multi-beam near zone axis conditions. This orientation is furthest away from a true zone axis orientation. While the advantage that the IAM approximation of the atomic scattering factors is better as compared to the conditions I and II, the combination of finer and more numerous features (Figure 16 (d)) with the actual disc size leads to complications in disc misalignment for data extraction and thereby degrade the refinement result. Nevertheless, condition III still yields better improvements than the zone axis orientation. Hence, among the four probed orientations the zone axis orientation (Figure 15 (a) and Figure 16 (a)) is the least sensitive to changes in structure factor.

5.1.2 Orientation selection – sensitivity to DW factors

If a beam-sample orientation is sensitive to changes in DW factors, the optimized DW factors obtained from different patterns should result in the same values, within the error bars, independent of orientation and thickness. We refined here three different zone axis orientations, and for six different condition I, six different condition II and six different condition III patterns, each acquired from different sample thicknesses. For each CBED condition, DW factors and corresponding low index structure factors as described above were included in the refinement. For the refinements we used the same parameters as described in 5.1.1, which is sufficient for beam sensitivity determination and maintenance of a high computation speed. Results from refinements of those patterns are listed in Table 5.

Table 5 Refined DW factors and corresponding R_w values (test case) from patterns of different sample-beam orientations

	Zone axis pattern			Condition I			Condition II			Condition III		
	$B_{Ni} (\text{Å}^2)$	$B_{Al} (\text{Å}^2)$	R_w									
1	0.1948	0.1665	0.21	0.2174	0.1971	0.14	0.2161	0.2667	0.18	0.2298	0.2431	0.18
2	0.3028	0.2374	0.15	0.2268	0.2250	0.12	0.1942	0.2187	0.16	0.2393	0.2353	0.19
3	0.2126	0.2136	0.20	0.2135	0.2001	0.11	0.2371	0.2262	0.17	0.1993	0.3056	0.17
4				0.1982	0.2051	0.10	0.2135	0.2163	0.14	0.1783	0.2291	0.15
5				0.2042	0.2509	0.17	0.2196	0.2040	0.15	0.1884	0.2605	0.17
6				0.1857	0.2481	0.17	0.2225	0.2343	0.15	0.2131	0.2563	0.17
Average	0.2367	0.2058		0.2076	0.2210		0.2172	0.2277		0.2080	0.2550	
Standard Deviation	0.0579	0.0361		0.0147	0.0241		0.0139	0.0216		0.0238	0.0275	

Table 5 indicates that DW factors determined from zone axis patterns are the most inconsistent. The three data points show big scatter, which results in high standard deviations for B_{Ni} and B_{Al} . This is consistent with the fact that the zone axis pattern exhibits the least sensitivity to changes in structure factors Figure 15 (a), as a relaxation of DW factors in the refinement actually changes high-index structure factors. Refinements of patterns obtained in condition I and II result in DW factors with quite small standard deviations. The slightly higher standard deviations obtained from condition III render this condition less suitable than condition II. Additionally, in condition II, all the four disks that intersect the Ewald sphere exhibit fine feature details and good signal-to-noise-ratio, which are optimal for data extraction. Conversely, in condition I, the intensity of the 100 and 010 discs is very low and strongly affected by noise, rendering both discs unsuitable for inclusion in refinement. Hence, condition I provides a much smaller number of usable data points than condition II, resulting in improved stability of the refinement using condition II. Since condition II provides the best combination of sensitivity to structure factors and DW factors and for robustness of the refinements it was dominantly used for simultaneously accurate determination of structure and DW factors.

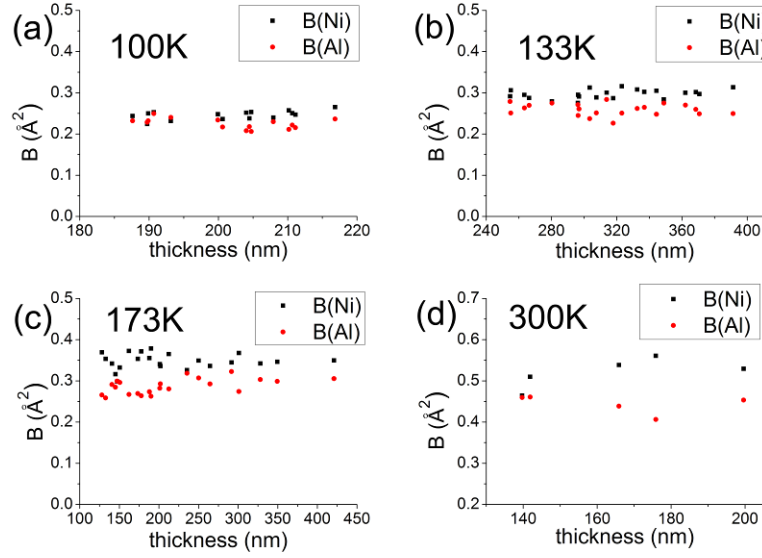


Figure 17 Refined DW factors B_{Ni} and B_{Al} versus thickness at different temperatures.

5.1.3 Temperature dependence of DW factors of β -NiAl

Multi-beam off-zone axis CBED patterns acquired in condition II were obtained at 100K, 133K, 173K and 300K. For each pattern, data points in 000, $\bar{1}10$, 110 and 200 discs were included in the refinement. DW factors B_{Ni} and B_{Al} and structure factors of reflections 100, 110 and 200 were relaxed during refinement. Other beams that have excitation errors less than 0.09\AA^{-1} are used as exact beams in the Bloch wave calculation. Beams whose excitation errors are between 0.09\AA^{-1} and 0.2\AA^{-1} are included in the calculation using the Bethe approximation [49]. Approximately 220 exact beams and 220 Bethe beams are included depending on slight changes of beam-sample orientations. Based on convergence test, this number of beams has proven sufficient to avoid error caused by truncation.

Optimized DW factors B_{Ni} and B_{Al} versus sample thickness at 100K, 133K, 173K and 300K are plotted in Figure 17 (a-d), respectively. Figure 17 (a-d) includes refinement results from 16, 21, 22 and 5 patterns obtained for different sample thicknesses, respectively. All refinement results have R_w value better than 0.2. Refinements that yield R_w values larger than 0.2 are generally unreliable and would be result in significant deviations of the experimental pattern from calculated pattern. Although many patterns obtained at room temperature have been refined only five of them yielded R_w values smaller than 0.2 (Figure 17 (d)), which can be attributed mostly to increasing detrimental effects from thermal diffuse scattering contribution. For patterns acquired at lower temperatures, R_w values are typically near 0.15. The reduced contribution from thermally diffuse scattering greatly improves the image quality and refinement reliability.

The average values and standard deviations of B_{Ni} than B_{Al} calculated from data points in Figure 17 are summarized in Table 6, which shows that increasing scatter of as temperature increases, consistent with the detrimental effects from thermal diffuse scattering. Figure 17 and Table 6 show that as temperature increases B_{Ni} increase more rapidly than B_{Al} in this temperature range. At 100K (Figure 17 (a)), the averaged B_{Ni} is only slightly larger than B_{Al} and for some data points, B_{Al} is larger than B_{Ni} . At 100K the temperature factors for Ni and Al are indistinguishable within the error of one standard deviation. At 133K and higher temperatures B_{Ni} is larger than B_{Al} , significantly so at room temperature (Figure 17 (d)).

Table 6 DW factors of B2 NiAl at 100K, 133K, 173K and 300K

Temperature	$B_{Ni} (\text{\AA}^2)$	Standard deviation (\AA^2)	$B_{Al} (\text{\AA}^2)$	Standard deviation (\AA^2)
100K	0.2462	0.0103 (4%)	0.2265	0.0132 (6%)
133K	0.2969	0.0112 (4%)	0.2591	0.0145 (6%)
173K	0.3475	0.0194 (6%)	0.2867	0.0186 (6%)
300K	0.5205	0.0364 (7%)	0.4437	0.0228 (5%)

5.1.4 Structure factors of β -NiAl at various temperatures

Along with DW factors obtained from the refinements described above, electron structure factors for 100, 110 and 200 reflections are also determined simultaneously. In our algorithm (Bloch-wave calculation), we relaxed DW factors of Ni and Al and several low order electron structure factors simultaneously. High order X-ray structure factors were approximated by the independent atom model and were fixed. High order electron structure factors were obtained from conversion of the fixed X-ray structure factors and to be refined Debye Waller factors using the Mott Formula. After completion of the refinement, low order X-ray structure factors were calculated from refined low order electron structure factors using the refined DW factors. One typical refinement result is shown in Figure 18, which plots $F_g(100)$ and $F_g(110)$ versus sample thickness from patterns obtained at 133K. Consistent structure factors are refined from patterns acquired in a thickness range of 240nm to 400nm.

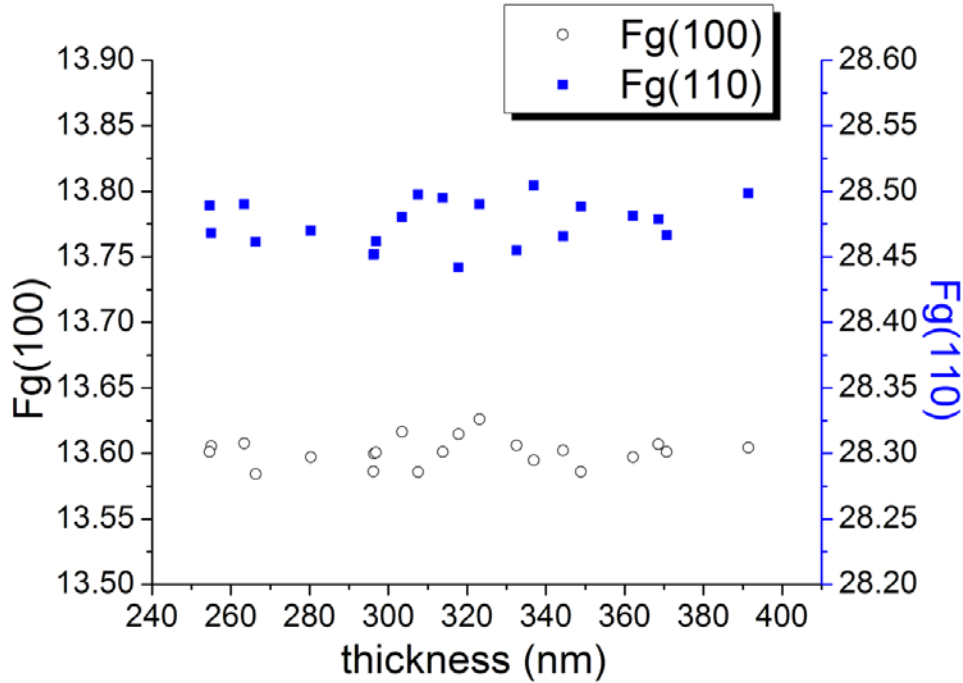


Figure 18 Refined structure factors versus thickness at 133K (left axis:F_g(100), right axis: F_g(110)).

The average values and standard deviations of low-index structures factors are summarized in Table 7. Despite simultaneously refining for DW factors and structure factors, the resulting refined structure factors are still highly accurate. The standard deviation for F_g(100) and F_g(110) at 100K is close to 0.05%. Standard deviations of the measurements for F_g(100) at all temperatures are less than 0.1%. The structure factors decrease as temperature increases because of larger atomic vibration amplitudes at higher temperatures (Table 7). Standard deviations generally increases as temperature increases because inelastic scattering is more pronounced at higher temperatures. Additionally, carbonaceous contamination films can grow under the electron beam illumination rapidly at room temperature for longer acquisition times, which can lead to increased background noise. At lower temperature ($T \leq 173\text{K}$), hardly any carbonaceous film growth was observed.

Table 7 Low-index X-ray structure factors and absorption factors of β -NiAl at 100K, 133K, 173K and 300K

	100K		133K		173K		300K	
	EXP	STD DEV	EXP	STD DEV	EXP	STD DEV	EXP	STD DEV
Fg(100)	13.615	0.008	13.601	0.011	13.568	0.013	13.517	0.011
Fg(110)	28.564	0.016	28.476	0.018	28.383	0.022	28.081	0.046
Fg(200)	23.843	0.069	23.668	0.085	23.597	0.164	23.082	0.181
Fabs(100)	0.077	0.004	0.086	0.002	0.092	0.006	0.119	0.004
Fabs(110)	0.129	0.005	0.141	0.003	0.162	0.015	0.195	0.005
Fabs(200)	0.115	0.013	0.122	0.007	0.143	0.027	0.170	0.032

5.2 DISCUSSION

5.2.1 Comparison of DW factors with previous results

Several different groups determined DW factors and structure factors of β -NiAl using various methods previously. In a prior study [97] DW factor amplitudes have been determined for Ni and Al, $B_{Ni} = 0.51 \text{ \AA}^2$ and $B_{Al} = 0.47 \text{ \AA}^2$ at room temperature using XRD. In [54] the systematic row CBED method has been used at 100K and obtained mean thermal displacements $\mu(Ni) = 0.55 \text{ pm}$ and $\mu(Al) = 0.57 \text{ pm}$, which can be converted to $B_{Ni} = 0.238 \text{ \AA}^2$ and $B_{Al} = 0.252 \text{ \AA}^2$ using $B = 8\pi^2 \langle \mu^2 \rangle$. Both data sets agree acceptably well with our results for room temperature and 100K. Our data differs from data reported by [54]. In our case B_{Ni} is higher than B_{Al} , while B_{Ni} is lower than B_{Al} in Nüchter's data at nominally the same temperature of 100K. However, the average values in Nüchter's data are within the standard deviation $B_{Ni} = 0.238 \pm 0.030$ and

$B_{Al} = 0.252 \pm 0.025$ [54] consistent with our results $B_{Ni} = 0.246 \pm 0.010$ and $B_{Al} = 0.226 \pm 0.013$. It should be noted, that, compared to prior reports, the standard deviation is by a factor of two to three time smaller for the data presented here. The implementation of the multi beam near zone axis method yields more accurate results than prior experimental reports.

5.2.2 Comparison of structure factors with previous results

Previously, [59] determined structure factors and DW factors of β -NiAl using X-ray diffraction. More accurate results were obtained by [181] using the critical voltage method. [14] calculated theoretical structure factors at 0K and room temperature. The room temperature data (300K) from prior studies are compiled and compared to the presented results in Table 4. Additionally, [52] performed CBED measurements of six low-order structure factors using two-beam conditions at 110K. The structure factors determined here at 100K and 133K (Table 8) agree within the measurement uncertainty with values reported by ([52]). Our results are consistent with both other measurements and calculations.

Table 8 Comparison of structure factors of reflection 100, 110 and 200 at room temperature, 300K

	Present result	Theory (LDA) [14]	Experiment [61]	Experiment [181]	IAM [98]
Fg(100)	13.517	13.45	13.53	13.47	13.270
Fg(110)	28.081	28.07	28.08	28.08	28.248
Fg(200)	23.082	22.99	22.60	23.02	23.120

5.2.3 Temperature dependence of DW factors

Temperature dependence of DW factors of β -NiAl have been investigated previously by [60] using a direct real space numerical simulation. [60] found that B_{Ni} is higher than B_{Al} at high temperature but lower than B_{Al} at low temperature. A crossover temperature was determined to be around 140K. The physical reason for a crossover temperature is caused by the fact that Ni has a higher atomic mass, which results in smaller B_{Ni} than B_{Al} at lower temperatures. However, the temperature dependence of lattice vibrations calculations for B2 ordered NiAl show that B_{Ni} increases faster than B_{Al} as temperature increases, which is reflected in a lower Debye Temperature for Ni, Θ_{Ni} , than for Al, Θ_{Al} [60, 180].

From our QCBED result, $B_{Ni} = (0.2969 \pm 0.0112) \text{ \AA}^2$ and $B_{Al} = (0.2591 \pm 0.0145) \text{ \AA}^2$, respectively, at 133K. Therefore, even taking into account the standard deviation, B_{Ni} is larger than B_{Al} (Figure 17 (b)). Furthermore, our measurements suggest that even at 100K still B_{Ni} is larger than B_{Al} . However, the measured values for B_{Ni} and B_{Al} could be the same at 100K, when the standard deviation of our measurements are considered. Our measurements imply that the cross-over temperature, below which is B_{Al} larger than B_{Ni} is about 100K or slight smaller. We used the Einstein model and Debye model to further analyze the cross over temperature. The DW factor amplitude of an atom in a crystal can be related to the thermal vibration frequency distribution function $g(\omega)$ using the following equation [60, 170],

$$B = \frac{8\pi^2}{3mN_0} \int_0^{\infty} \frac{E(\omega)}{\omega^2} g(\omega) d\omega, \quad (37)$$

where $E(\omega) = \frac{1}{2}\hbar\omega + \frac{\hbar\omega}{e^{\frac{\hbar\omega}{k_B T}} - 1}$ m is the atomic mass, N_0 is the number of atoms in the

crystal. $g(\omega)$ must satisfy $3N_0 = \int g(\omega)d\omega$. In the Einstein model, each atom oscillates independently and with the same frequency, which gives $g(\omega) = 3N_0\delta(\omega - \omega_E)$. In the Debye model, the vibration characteristics differ for frequencies below and above the Debye cut-off frequency, ω_D , such that $g(\omega) = 9N_0 \frac{\omega^2}{\omega_D^3}$ for $\omega < \omega_D$ and 0 for $\omega > \omega_D$, where ω_D is the Debye cut-off frequency, which is related to the Debye temperature Θ_D by $\hbar\omega_D = k_B\Theta_D$. Based on these two different models Einstein frequencies for the two atom species, $\omega_E(\text{Ni})$ and $\omega_E(\text{Al})$, and Debye temperatures, Θ_{Ni} and Θ_{Al} , can be optimized to fit the temperature dependence of the DW factor related vibration amplitudes measured here from the presented CBED data.

Einstein frequencies of $\omega_E(\text{Ni})=24.6\text{ps}^{-1}$ and $\omega_E(\text{Al})=42.8\text{ps}^{-1}$ result in the best comparison with DW factor amplitudes obtained at the various temperatures in our experiments. Figure 19 (a) shows the temperature dependence of calculated B_{Ni} and B_{Al} based on the Einstein model. The theoretical values show excellent consistency with our data at different temperatures, especially for B_{Al} . According to the Einstein model a crossover temperature of 97.8K is predicted. Previously, [60] obtained $\omega_E(\text{Ni})=26.1\text{ps}^{-1}$ and $\omega_E(\text{Al})=41.1\text{ps}^{-1}$ using B_{Ni} and B_{Al} at room temperature from [97]. Both values agree fairly well with our calculation.

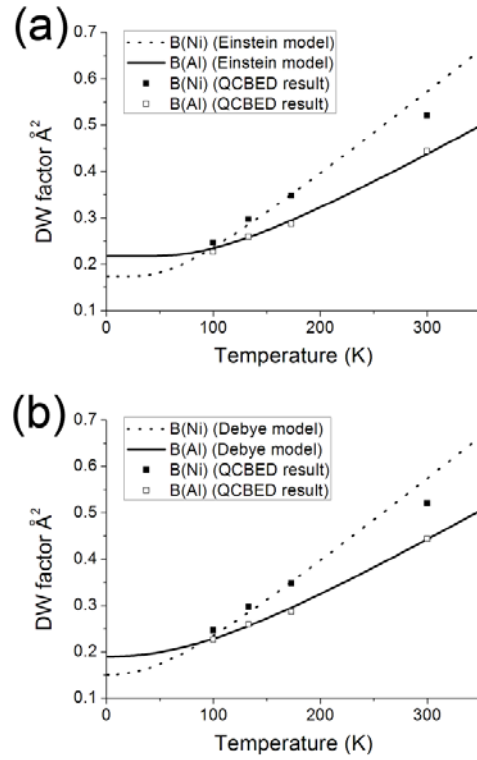


Figure 19 Plots of theoretical and experimental B_{Ni} and B_{Al} versus temperature. (a) Einstein model. (b) Debye model.

When the Debye model is used, the best comparison between theoretical prediction and the CBED based experimental measurements is achieved for $\Theta_{Ni} = 325\text{K}$ and $\Theta_{Al} = 562\text{K}$. The temperature dependence of B_{Ni} and B_{Al} based on the Debye model is shown in Figure 19 (b). Again good consistency is shown between theoretical calculation and experimental measurement, resulting in a cross-over temperature of 90.6K. Θ_{Ni} and Θ_{Al} were determined by [180] as 332K and 563K using neutron scattering. Both Debye temperature values agree well with calculation based on the CBED measurements presented here. Since the Debye model describes the temperature dependence of vibrations of crystalline structures more realistically

than the Einstein model, the cross-over temperature predicted by the Debye model is considered more accurate. It has been estimated [54] that electron beam heating may increase the sample temperature by about $\Delta T \approx 7\text{K}$. The beam heating effect may systematically shift the temperatures we report to higher values. The cross over temperature is $90.6(+7.0)\text{K}$ based on our experimental measurements by CBED, which is significantly lower than previously reported [60].

5.3 CONCLUSION

Highly accurate structure factors and DW factors were simultaneously measured using a multi-beam near zone-axis CBED method for B2 NiAl at different temperatures. An orientation close to a [001] zone axis orientation was obtained by tilting the sample to bring (200), (020) and (220) reflections into Bragg condition. In this orientation we obtained CBED patterns that produce robust DW factors and structure factors with an accuracy of 0.05% for $F_g(100)$ and $F_g(110)$ at 100K. This study demonstrated the superior sensitivity of this type of multi-beam near zone axis orientations to changes of DW and structure factors relative to that of a [001] zone axis orientation. The successful application of the refinements of special orientation QCBED patterns on the determination of DW factors and low-index structure factors of B2 NiAl suggests that the same also applicable to the more challenging cases of $L1_0$ FePd and FePt with unknown and anisotropic DW factors and structure factors.

The temperature dependence of DW factors for the Ni and Al atoms in NiAl is explained using an Einstein model and a Debye model. Our CBED based measurements qualitatively confirm prior studies by [60] that predicted that a crossover temperature exists, at which Al and

Ni would have the same DW factors. From the QCBED data presented in this study a more accurate and lower temperature of 90.6K has been determined for this cross-over temperature.

6.0 THEORETICAL INTERPRETATION OF SENSITIVITY

In this chapter, Bloch wave branches and dispersion surface analysis will be used to prove that the multi-beam off-zone axis method is more sensitivity to change of DW factors and structure factors than the other methods in the context of simultaneous measurement. This section of the dissertation document is based on a manuscript under review for publication to Ultramicroscopy.

Establishing QCBED as an experimental tool for determination of electronic density and structure via accurate measurements of structure factors from local probing of nanometer scale volumes for a broadened range of crystalline inorganic substances requires methods capable of simultaneous refinements of both structure factors and DW factors. The multi-beam off-zone axis QCBED methods appear to satisfy this requirement according to previous experiments (Chapter 4.0 and 5.0). The origins of the improved quality of experimental data acquired with the multi-beam off-axis QCBED methods relative to the excited row and zone-axis approaches remain to be elucidated.

In this chapter we investigate and compare the influence of differences in number and excitation amplitude of respective Bloch wave states for the three commonly used QCBED on accuracy of simultaneous structure and DW factor refinements. We performed computer simulations of the QCBED patterns for Si for the different methods and discuss implications on accuracy and precision of structure and DW factors obtained via simultaneous refinements. We

will focus on comparison of the multiple diffracted beam methods, namely the zone axis method and the near or off-zone axis method, since these QCBED approaches enable acquisition of data sets suitable for the simultaneous refinements of multiple structure factors from a single experiment. We find out that in general, a QCBED pattern will be more sensitive to changes in both structure and DW factor, if it contains more and stronger excited Bloch wave branches, as the dynamic interactions of the Bloch waves increase the sensitivity of the pattern.

6.1 THE INFLUENCE OF THE NUMBER AND AMPLITUDE OF EXCITED BLOCH WAVE BRANCHES ON PATTERN SENSITIVITY TO CHANGES IN STRUCTURE FACTOR

In the Bloch wave formalism description of dynamical diffraction theory of fast electrons by crystals, the wave function Ψ of an electron in the periodic potential is the sum of Bloch wave branches $\Psi^{(j)}$ with different excitation amplitudes $\alpha^{(j)}$,

$$\Psi(\mathbf{K}_t) = \sum_j \alpha^{(j)}(\mathbf{K}_t) \Psi^{(j)}(\mathbf{K}_t), \quad (38)$$

Although there are hundreds of Bloch wave branches in a crystal only two to three branches are strongly excited in the zone axis orientation and only two strongly excited branches result for the excited row incident beam-sample orientation [182, 183]. Bloch wave formalism based simulations in these conditions have been used for simplification to interpret fringe contrasts in zone axis orientation (ZAP – technique) CBED patterns [183]. The excited or systematic row method and the ZAP method are the two QCBED methods that have been most

widely used in the past for structure factor determination. The excited row method [26, 28], to date still favored by many researchers, uses a systematic row orientation, where one disk of the systematic row satisfies the Bragg condition. The interaction between the incident beam and the diffracted beam results in a simple one dimensional fringe-pattern in the CBED discs, as in this two-beam condition only two Bloch waves are strongly excited and strongly interact with each other. The structure factor of the particular excited reflection can be obtained by pattern refinement. The ZAP method approach [33, 99, 154], refines two-dimensional zone axis CBED patterns, resulting in two-dimensional fringe patterns. When the incident electron beam is parallel to a zone axis orientation of the crystals multiple diffracted beams or reflections are excited to similar levels, but none of them fulfill their respective exact Bragg condition. Thus, multiple structure factors can be obtained from one zone axis QCBED pattern simultaneously, even though many reflections have deviation vectors \mathbf{s} with small but significant magnitudes. Interestingly, the number of excited Bloch wave branches of the excited row and zone axis orientations is rather similar; i.e. only two or three Bloch wave branches are strongly excited and interact dynamically with each other. D. M. Bird et al. [139] investigated the sensitivity of CBED patterns to changes in structure factor using numerical methods and Saunders et al. [129] stated that both the ZAP and two-beam condition methods provide structure factors accurate enough for the investigation of bonding effects in crystalline materials. However, while the ZAP – method has been applied for simultaneous refinement of multiple structure factors [128, 129], the question remains whether the limited number of strongly dynamically interacting Bloch wave states suffices to ensure high enough sensitivity and low enough error for electron charge density determination. The possible role of the limited number of strongly dynamically interacting Bloch wave states regarding introduction of significant uncertainty remains to be ascertained. Enhanced

levels of certainty of refinement results from experimental QCBED are desirable and even required for simultaneous structure and DW factor determination for more complicated systems that contain multiple different elements and atom species of heavier elements with electrons in d and f orbitals. A third QCBED method, which has been applied successfully in numerous more recent studies for simultaneous determination of multiple structure factors, the near or off – zone axis multi beam orientation, uses an incident electron beam that is close to a zone axis orientation. In contrast to the zone axis method the crystalline sample is slightly tilted away from the exact zone axis orientation, such that three or more g_{hkl} reflections exactly satisfy the Bragg conditions, which is rather similar to the excited row approach. We found that compared to the zone axis technique more Bloch wave branches are excited for the near or off – zone axis multi beam orientation. In addition, the excited Bloch wave branches generally have larger amplitudes. The use of this technique has yielded results of higher accuracy than the zone axis and the excited row techniques [57, 58, 140, 154]. In the following sections, we will compare the number and excitation amplitudes of Bloch wave branches of the zone axis technique with the multi-beam off-zone axis approach, the only two methods that allow simultaneous refinement of multiple structure and DW factors and discuss implications on accuracy and precision of simultaneous refinements.

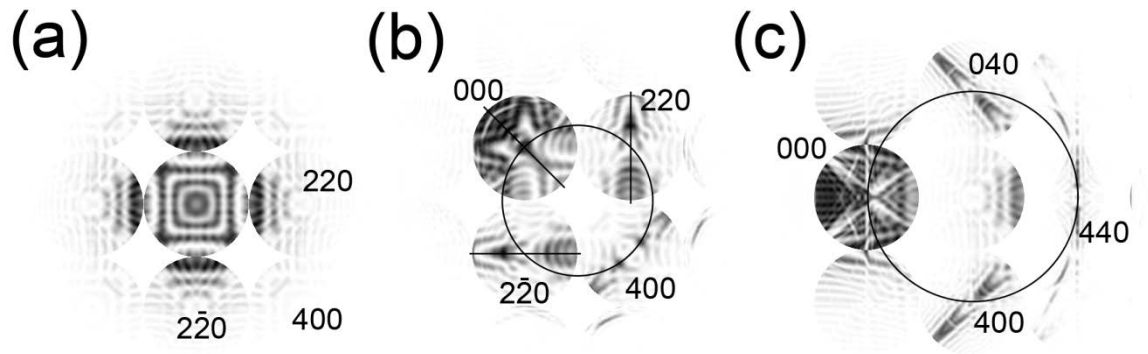


Figure 20 Simulated CBED patterns at different orientations: a) zone axis pattern, b) of – zone axis pattern multi beam orientation I (Ewald sphere intersects 000, 220, 2-20 and 400), c) of – zone axis pattern II (Ewald sphere intersects 000, 040, 400 and 440)

6.2 COMPARISON OF RESULTS FOR SI OBTAINED FROM THE ZONE AXIS METHOD AND THE OFF-ZONE AXIS MULTI BEAM TECHNIQUE CONDITION

We have performed computer simulations to obtain the excitation amplitudes for diamond cubic (A4; cF8; Fd3m) Si for a [001] zone axis orientation (Figure 20 (a)) and also for two different multi-beam off-zone axis patterns with orientations for an incident beam nearly parallel to a [001] zone axis (Figure 20 (b) and (c)). The electron diffraction simulations used an accelerating voltage of 200kV and a DW factor, $DW = 0.45 \text{ \AA}^2$, which is fairly close to the experimental and theoretical DW factor of Si at room temperature [13]. The structure factors are calculated based on the independent atom model from [98]. This approximation is appropriate as the true F_g are very similar to IAM F_g 's and additionally this study investigates the sensitivity of CBED patterns which is defined as the first derivative of the intensity with either structure or DW factors which both remain unaffected by this approximation. The sample thickness is 200 nm for all three

simulated patterns shown in Figure 20. The intensity in all patterns is inverted. Black corresponds to high intensity. Depending on the orientation, approximately one hundred exact beams and an additional 100 Bethe beams, were included in the calculations [99]. In the first multi-beam off-zone axis CBED pattern, shown in Figure 20 (b), the g_{220} , g_{2-20} and g_{400} reflections fulfill the Bragg condition and are strongly excited (from hereon referred to as orientation I), while in the second multi-beam off-zone axis CBED pattern, Figure 20 (c), g_{400} , g_{040} and g_{440} (from hereon referred to as orientation II) were exactly Bragg excited. The zone axis pattern (Figure 20 (a)) shows symmetry of a four-fold rotational symmetry axis and two sets of mirror planes expected for the [001] zone axis. The intensity in the center disk is much higher than the intensity in all the diffracted g_{hkl} discs, due to the large magnitudes of all the deviation vectors $s(g_{hkl}) > 0$. The intensity of the diffracted beams in the other disks decreases rapidly as the scattering angle increases. Areas with very low intensity in the CBED pattern generally also have very small signal to noise ratio (SNR). Concomitantly intensity data from those areas is heavily influenced by the significant noise associated with small SNR. Although modern TEM's equipped with energy filters are capable of blocking most inelastically scattered electrons, thermally diffuse scattering (TDS) background is reduced, but not filtered out completely and still present. In our experiments, Kikuchi patterns always exist in Si CBED patterns, enhancing difficulties in background correction during QCBED refinements. Most researchers assumed in first approximation a constant background [26, 99]. In reality the background distribution is more complicated [154]. If an insufficient background correction method is used during the refinement, a significant error may be introduced especially from regions with a poor SNR. Since currently existing methods cannot ascertain the quality of the background correction, we decided to exclude areas with low intensity, which are heavily influenced by inelastic scattering and TDS

and suffer from poor SNR. Therefore, for the zone axis pattern (Figure 20 (a)), only the center disk and the parts of the g_{220} , g_{2-20} , g_{-2-20} and g_{-220} reflection discs (\sim one quarter of the disc area) with sufficient SNR can be used for the refinement, which significantly reduces the area in zone axis patterns providing data useful for refinement.

Hence, we decided to use a different incident beam sample orientation and tilt away from the zone axis until at least three discs are in Bragg condition. As described in the previous section, such an orientation constitutes an off – zone axis multi beam orientation [56-58, 140]. Figure 20 (b) and (c) shows two example off – zone axis multi beam orientation CBED patterns. The black circle in the Figure 20 (b) delineates the trace of the Ewald sphere, which intersects g_{220} , g_{2-20} and g_{400} reflections in the zero-order Laue zone plane. Although this pattern cannot reflect the four-fold symmetry of the [001] zone axis, symmetry can still be used to tilt the sample into the desired orientation, as the zero disc and each of the discs of the diffracted beams g_{hkl} in Bragg orientation exhibit their own symmetry. The contrasts of the 000, 220 and 2-20 disks have mirror planes as indicated by the black lines marked in Figure 20 (b). For the CBED orientation in Figure 20 (b) the 400 disc exhibits two perpendicular mirror planes. The symmetry of this so-called dark field CBED was discussed in [155]. Similar to zone-axis patterns, the symmetry imposed on this off-zone axis pattern can be used to ascertain that the sample area is defect free. The presence of crystalline defects, such as dislocations, would introduce a symmetry break in the pattern. The intensity in the off-zone axis pattern in condition I, Figure 20 (b), is more evenly distributed in the four discs, which satisfy the Bragg conditions than in the zone axis orientation CBED of Figure 20 (a). The intensity is still highest in the center disc, but in the other diffracted g_{hkl} beam discs, which intersect the Ewald sphere, intensity is sufficiently high to offer SNR that allow for high accuracy, high precision QCBED refinement. The fringe

pattern in the 000, 220, 2-20 and 400 discs for condition I (Figure 20 (b)) is more complex than that obtained in the zone axis pattern (Figure 20 (a)), indicating interference of an increased number of Bloch wave branches. Figure 20 (c) shows another example of an off – zone axis multi beam orientation (orientation II) CBED pattern. Even though the complexity of the fringe pattern is increased even with respect to the off – zone axis multi beam orientation I shown in Figure 20 (b), indicating an involvement of even more Bloch wave branches, the intensity distribution in the pattern is less uniform among the discs satisfying the Bragg conditions as compared to orientation I. This renders orientation II (Figure 20 (c)) less ideal for refinement than orientation I (Figure 20 (b)).

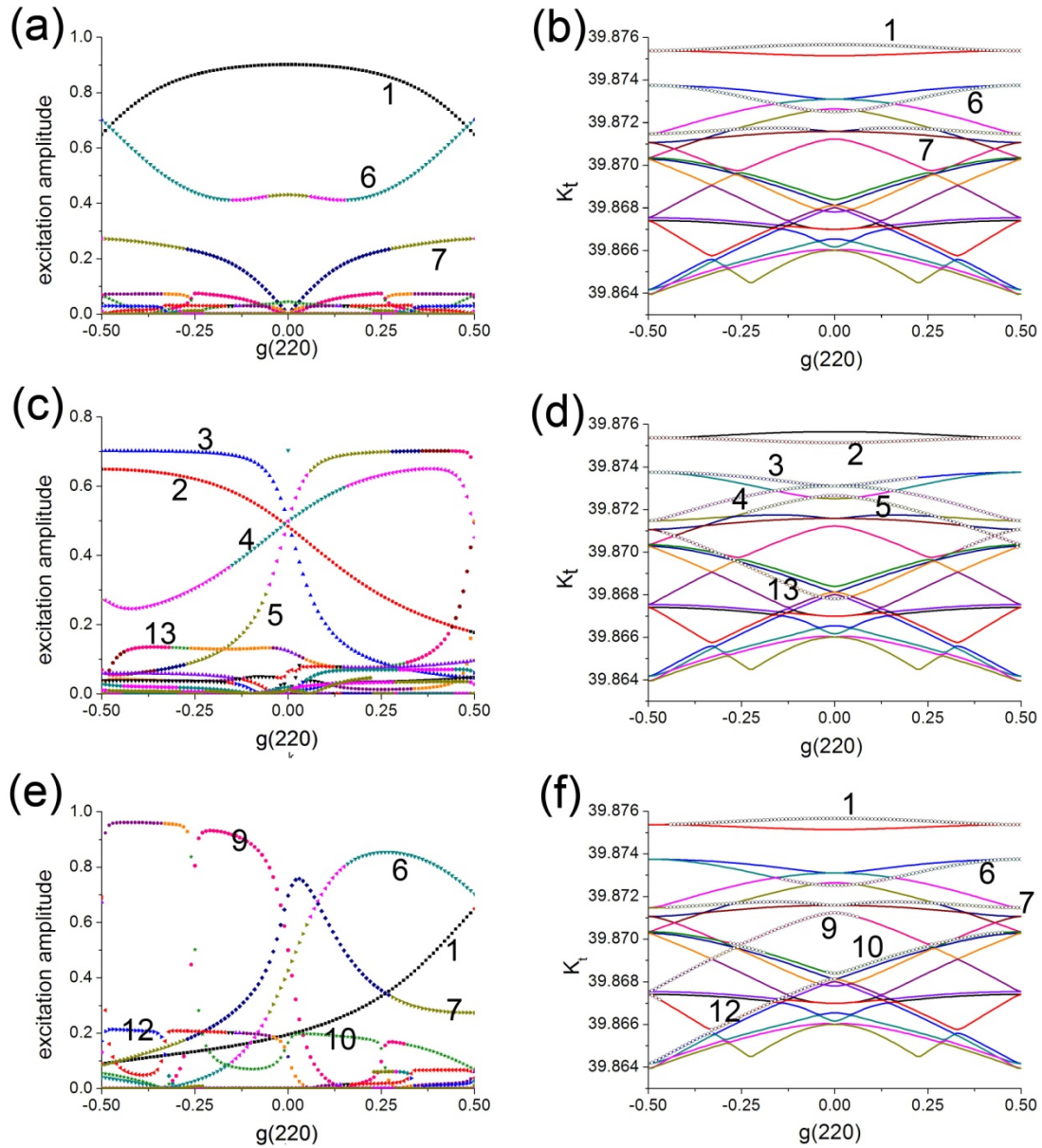


Figure 21 Excitation amplitude and dispersion surface centered about g_{220} in Si, 200kV electron beam, for zone axis condition (a, b) and the multi-beam off-zone axis orientations I (c, d) and II (e, f); The branches annotated by numbers exhibit relatively strong excitation amplitudes (see text for details)

6.3 EXCITATION AMPLITUDE

Dispersion surfaces for the zone axis CBED pattern and the orientation I and II off-zone axis CBED patterns were simulated using, depending on the orientation, approximately 100 exact and 100 Bethe beams. The results are shown in Figure 21 (b), (d) and (f). Branches with excitation amplitudes higher than 0.1 are depicted by empty circles. The variation of color in each branch is a result of curve overlap, which is therefore not differentiable in certain regions of k – space. As the dispersion surfaces for the different orientations are very similar, we investigated the excitation amplitudes (Figure 21 (a), (c), and (e)) of the first 20 Bloch wave branches.

In Figure 21 (a), (c), and (e) the excitation amplitudes of the first 20 branches for the zone axis condition (Figure 21 (a)), and the multi-beam off-zone axis conditions I (Figure 21 (b)) and II (Figure 21 (c)) are plotted in reciprocal space along the g_{220} direction. This one-dimensional profile reasonably reflects excitation amplitudes of different branches in two-dimensional discs. Only two to three branches have significant excitation amplitudes in the zone axis orientation. The high excitation amplitude branches (as indexed 1, 6 and 7 in Figure 21 (a)) are in the upper part of the dispersion surface (Figure 21 (b)), therefore representing interactions between the electron beam and the core electrons [184]. For the multi-beam off-zone axis condition I shown in Figure 21 (b), four to five beams always have significant excitation amplitudes (indexed as 2, 3, 4, 5 and 13 Figure 21 (c)). Some of the excited branches (for example branch 13 in Figure 21 (c) and (d)) are in lower parts of the dispersion surface and represent interactions of the electron beam with spaces in between atoms. These branches are more likely to interact with electrons that participate in interatomic bonding. Hence, the off – zone axis multi beam technique is superior to the zone axis method, as it utilizes an incident

beam sample orientation were not only more Bloch waves are excited but the excited Bloch wave states are also more sensitive to electrons that are more directly associated with and affected by details of the inter-atomic bonding than core electrons. This trend is confirmed upon investigation of excitation amplitudes (Figure 21 (e)) that correspond to multi-beam off-zone axis orientation II shown in Figure 21 (c), where five to six branches are strongly excited (branches 1, 6, 7, 9, 10 and 12 in Figure 21 (e)) and two of these are in the lower part of the dispersion surface (branches 10 and 12 in Figure 21 (e)). Although more Bloch waves are excited as the sample is tilted further away from the zone axis orientation, the pattern also has a less uniform intensity distribution in the discs, which can deteriorate the data quality, the SNR and concomitantly detrimentally affects refinement results.

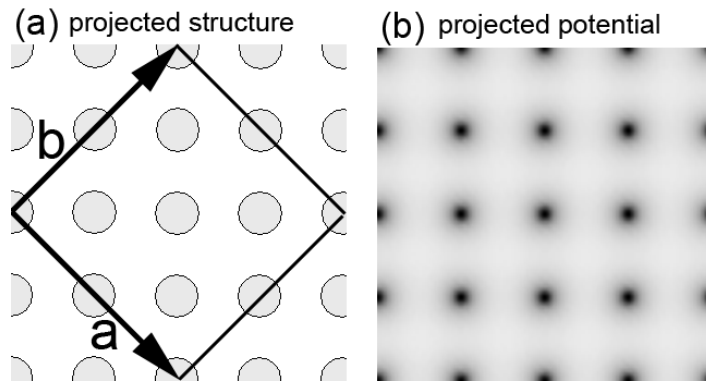


Figure 22 Projected structure (a) and Coulomb potential (b) for diamond cubic structure along [001] zone axis (black indicates a strongly positive potential)

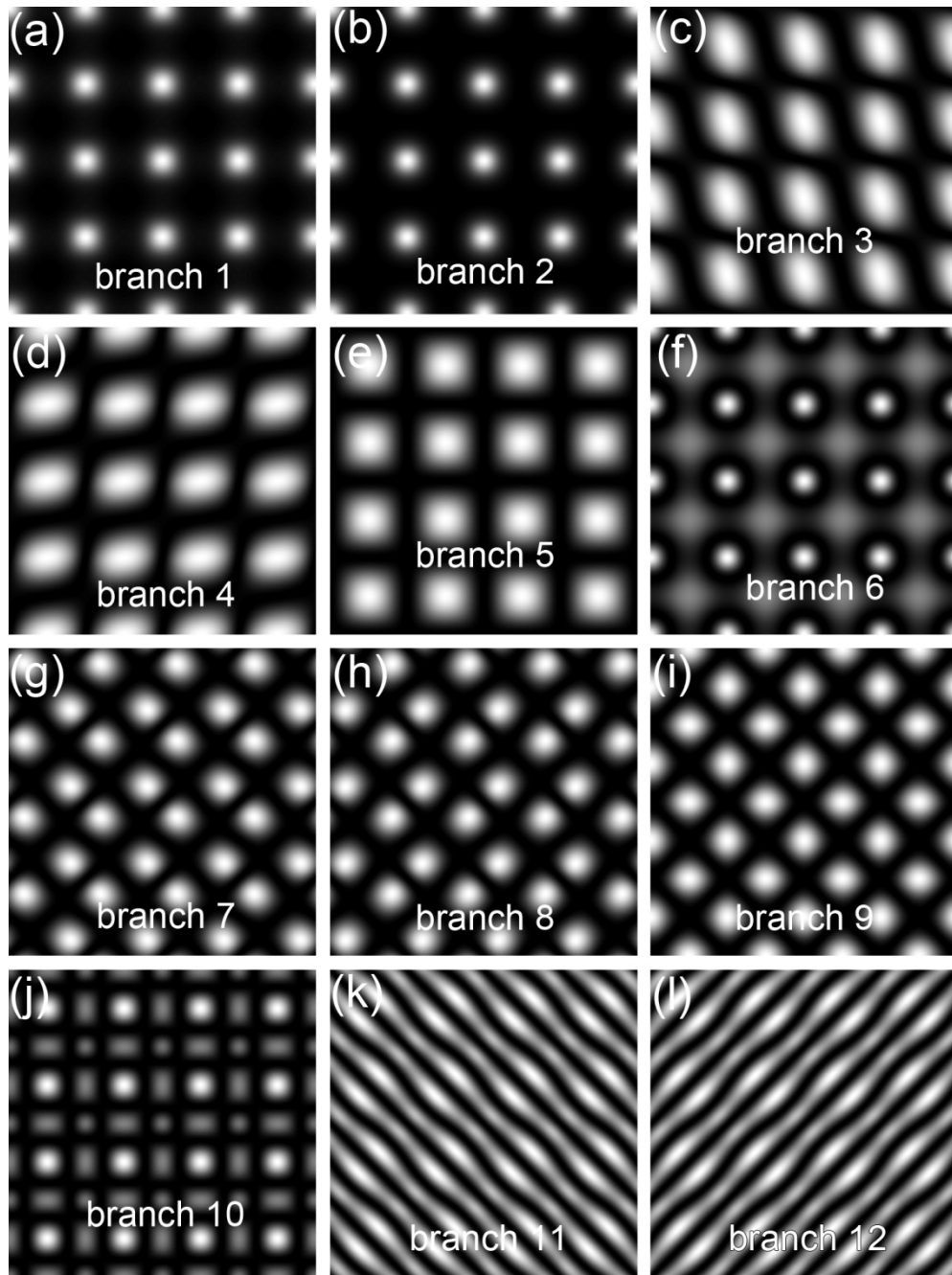


Figure 23 Electron probability distribution for the first 12 Bloch states for the [001] zone axis condition. The brightest area has the highest intensity. The darkest area has the lowest intensity. The highest intensity varies for each branch.

To better understand and illustrate how different Bloch wave branches interact with the crystal potential two dimensional intensities of various Bloch states in real space along a [001] zone axis condition are plotted in Fig. 4, and compared with the projected structure Figure 22(a) and projected potential Figure 22 (b) along the same orientation. The projected Coulomb potential in Figure 22 (b) has been constructed from IAM structure factors and is mainly used here to illustrate the positions of atom columns. The Bloch wave branches, whose probability maxima coincide with the projected atomic positions, are referred to as bound states, as for example branches 1 and 2 in Figure 23, as these Bloch wave branches interact with the strongly bound core electrons [184]. Branches 3, 4, 5, and 9 have maxima between atom columns and therefore could interact with the electron charge density, which participates in the interatomic bonding in the materials, if present. They are also referred to as anti-bound states. Branches 6, 7, 8, 10, 11 and 12 can be considered as mixed states as they have probability distribution on and in between atom column positions (i.e., they probe simultaneously bound and anti-bound). For mixed states the intensity in between atoms is usually rather weak as compared to the intensity that coincides with atom positions. Figure 21 (a) shows that in the zone axis orientation only the Bloch wave branches 1, 6 and 7 are strongly excited (see annotation in dispersion surface plot of Figure 21 (b)). Branch 1 is a bound state, branch 6 is mixed (Figure 23 (a) and (f)). Only branch 7 is an anti-bound state, which has high intensity between atomic columns and could therefore interact with the possibly present electron charge density that contributes to interatomic bonding. The probability distribution in branch 6 that coincides with areas in between atoms is very low as compared to the distribution on the atoms. The strong excitation of only one anti – bound branch that can possibly interact with bonding electrons causes the fairly low sensitivity of the

corresponding CBED pattern to small changes in structure factors originating from interatomic bond electron charge density.

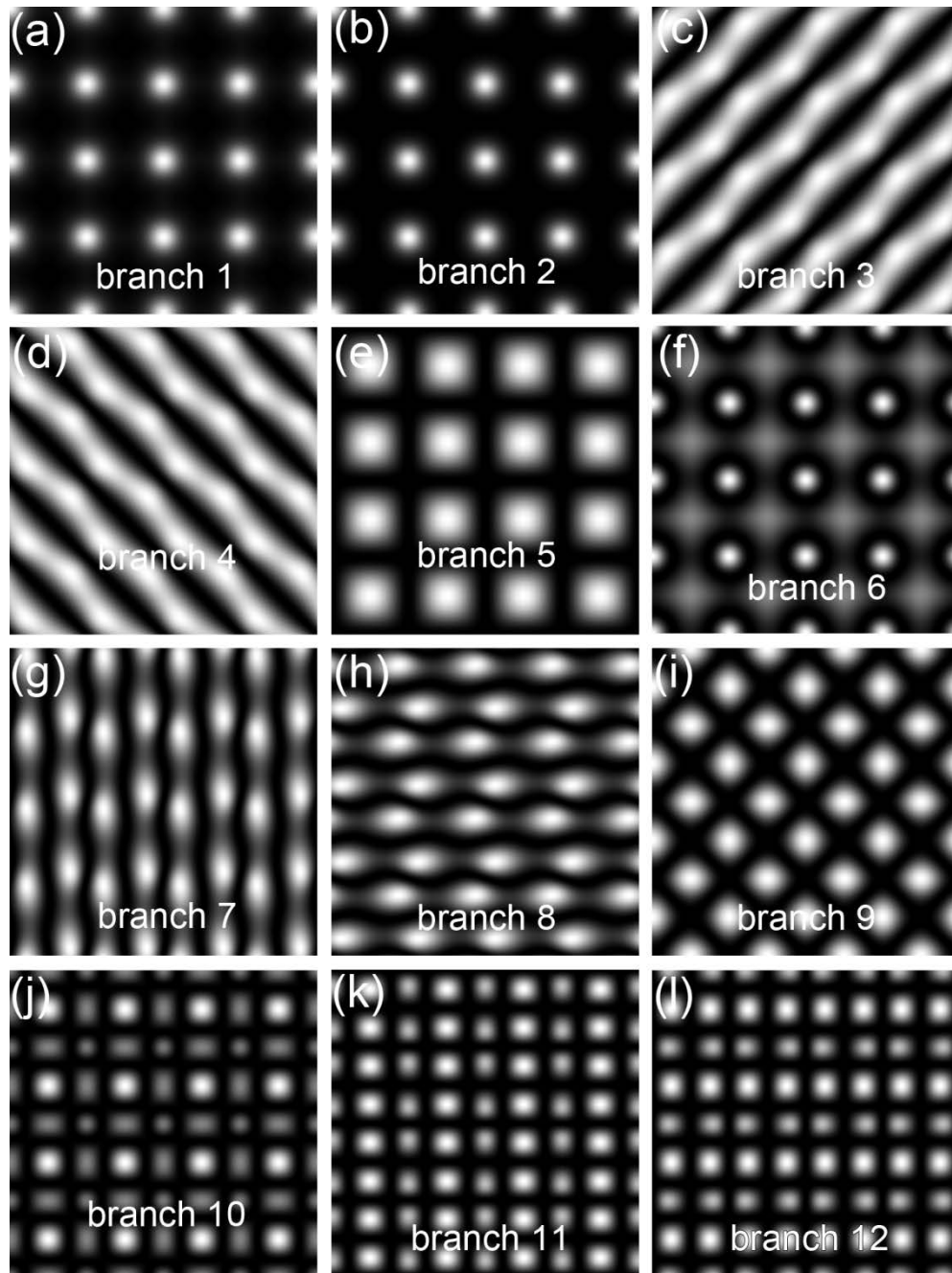


Figure 24 Electron probability distribution for the first 12 Bloch states for the near [001] off-zone axis multi-beam condition.

Bloch wave branches for the off-zone axis condition I (Figure 20 (b)) are shown in Figure 24. Branches 1, 2, 5, 6, 9 and 10 show similar behavior as compared to the corresponding branches of the zone axis orientation. Branches 1, 2 are bound states, while branches 5 and 9 are anti-bound states and branches 3, 4, 6, 7, 8, 10, 11 and 12 are mixed. Bloch wave states with highly symmetric wave functions are relatively insensitive to changes of beam direction. Therefore, bound and anti-bound state related branches and the highly symmetric mixed Bloch wave branch 6 are insensitive to small orientation changes, whereas mixed states are quite sensitive and show significant intensity changes even for small orientation changes.

For off-zone axis multi-beam condition I the mixed states 3, 4 and anti-bound state 5 are strongly excited (Figure 21 (c)). These three branches exhibit high electron probability distributions in locations that coincide with locations where electron charge density that contributes to bonding in Si crystal is expected [13], rendering these branches sensitive to interatomic bonding effects in Si. As the increased number and higher excitation of anti-bound and mixed Bloch wave branch probability amplitudes coincide with locations of electrons that contribute to interatomic bonding in off-zone axis multi-beam condition I, this orientation is more sensitive to bonding related changes in structure factors than the zone axis orientation.

The intensity distribution in the multi-beam off-zone axis condition II (Figure 20 (c)) is not as uniform as in the simulated CBED pattern of the off-zone axis condition I (Figure 20 (b)). Therefore, it does not qualify for high accuracy QCBED refinements. Additionally, image distortions caused by the lens system and the GIF system become more pronounced as the scattering angle increases. Although condition II was previously used to obtain DW factors, it was later found that CBED experiments performed with condition I (Figure 20 (b)) are also suitable to obtain both DW factors and structure factors simultaneously with high accuracy.

The sensitivity of the pattern to the changes in DW and structure factors can be calculated from comparisons of intensity distributions in CBED patterns simulated via the Bloch wave formalism that were refined using different simulation parameters. For example, to estimate the sensitivity of the intensity distribution in a CBED pattern to changes in DW factor, the relation below can be used,

$$S = \sqrt{\frac{\sum_{i=1}^N (I_i(B + \Delta B, U) - I_i(B, U))^2}{N}}, \quad (39)$$

where $I_i(B + \Delta B, U)$ is the intensity on the i^{th} point using a DW factor $B + \Delta B$ in the simulation and $I_i(B, U)$ is the intensity on the i^{th} point using DW factor B . N is the number of sampling points in the CBED pattern. For the estimation of the sensitivity of the intensity distribution to changes in structure factors, instead of the DW factor amplitude B the electron structure factor U is varied. $I_i(B + \Delta B, U)$ is replaced by $I_i(B, U + \Delta U)$ in equation (39). Si CBED patterns were simulated for sample thickness ranging from 20nm to 300nm using a DW factor of 0.45 \AA^2 . To estimate the sensitivity to changes in the DW factor, two sets of CBED patterns were simulated. One with $B = 0.45 \text{ \AA}^2$ and the second with $B = 0.451 \text{ \AA}^2$, i.e. $\Delta B = 0.001 \text{ \AA}^2$. Each disk in the CBED pattern contains 7920 data points, which is sufficient for accurate fringe and contour simulation. For the zone axis pattern, the center disc and four 220 - type discs are included in the sensitivity calculation. For off-zone axis patterns, the four discs that fulfill the Bragg condition exactly, i.e. $s = 0$ are used to calculate the sensitivity. The calculation results are shown in Fig. 6a. The CBED patterns acquired from the four - beam condition I with excited g_{220} , g_{2-20} and g_{400} reflections (Figure 20 (b)) are generally more sensitive to changes in DW

factor in the simulated thickness range than the other two conditions. The second four - beam condition II with excited g_{400} , g_{040} and g_{440} (Figure 20 (c)) is as sensitive as the zone axis orientation pattern to changes in DW factor.

To estimate the sensitivity of the different orientation CBED patterns to changes in structure factors, first the IAM X-ray structure factor 8.4552 for $F_{g_{220}}$ was used to simulate I(U + Δ U,B) and $F_{g_{220}}$ 8.4549 for I(U,B). The difference is plotted in Figure 25 (b). The four-beam condition I (Figure 20 (b)) is slightly more sensitive than the zone axis orientation, especially for thicknesses in excess of 150nm. The second four-beam condition II (Figure 20 (c)) is not sensitive to changes in $F_{g_{220}}$ as in this orientation the 220 – discs are not excited. Therefore we additionally simulated the sensitivity of CBED patterns in orientations I and II and the zone axis orientation (Figure 25 (c)) to changes in structure factor $F_{g_{400}}$. A value of 7.0672 for $F_{g_{400}}$ was used to calculate I(U + Δ U,B) and 7.0665 to calculate I(U,B). Both four-beam conditions are more sensitive to changes in $F_{g_{400}}$ than the zone axis condition. Condition I is most sensitive. In summary, for silicon, the four beam condition I is most sensitive to changes in both DW and structure factors.

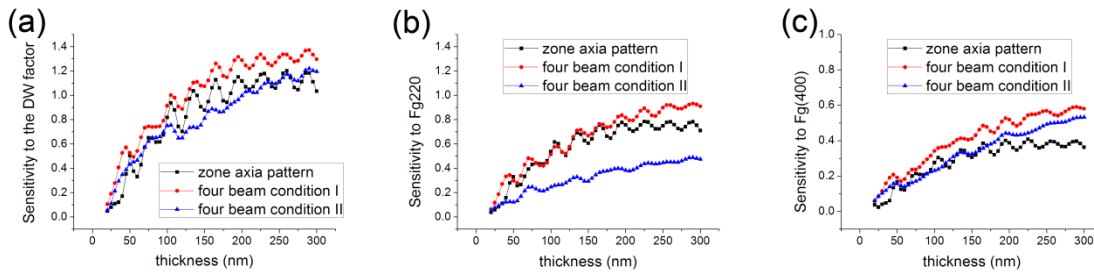


Figure 25 Sensitivity of the CBED patterns under different sample-beam orientations to the change of DW factor (a), structure factor $F_{g_{220}}$ (b) and $F_{g_{400}}$ (c) versus thickness.

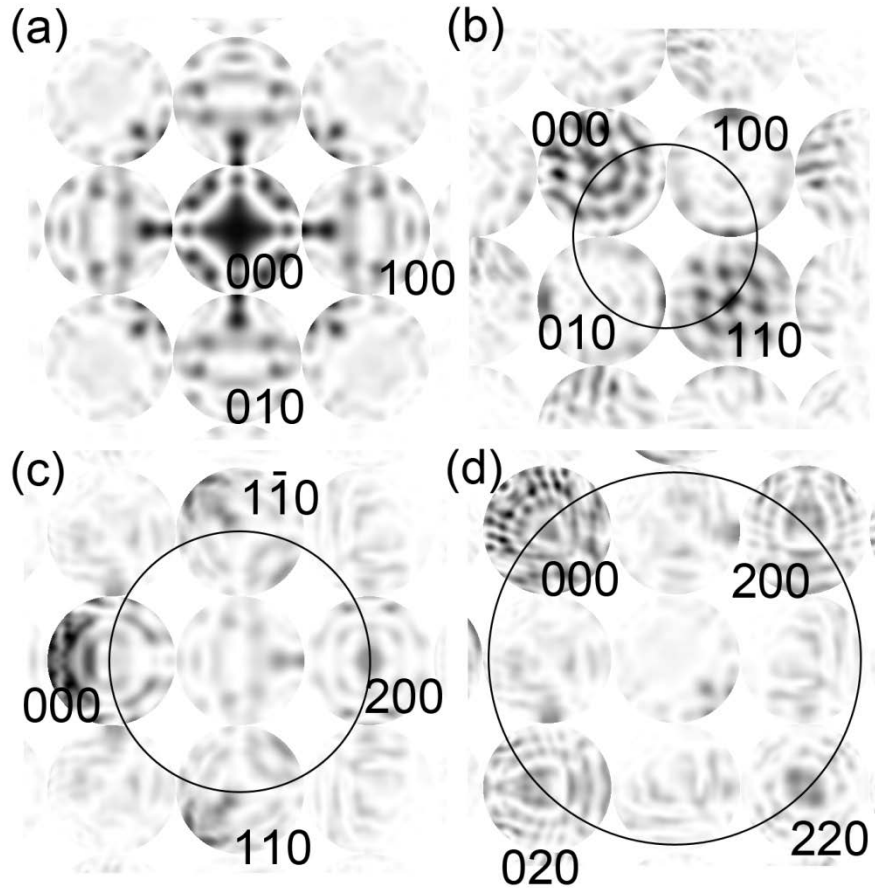


Figure 26 simulated CBED patterns for NiAl at zone axis condition (a) and three off-zone axis multi-beam conditions (b-d).

6.4 RESULTS INTERMETALLIC B2 ORDERED NIAL

To see whether our findings for Si also apply for QCBED analysis of other materials systems we investigated B2 cubic ordered NiAl, which has two different atoms in the unit cell, one Ni atom at $0, 0, 0$ and one Al atom at $\frac{1}{2}, \frac{1}{2}, \frac{1}{2}$. The DW factors of Ni and Al were set to $B_{\text{Ni}} = 0.297$ and $B_{\text{Al}} = 0.259$ respectively, which are obtained from previous measurements of DW factors for NiAl at different temperatures [58]. Structure factors were calculated based on the independent

atom model [98]. CBED patterns with a same sample thickness of 200nm were simulated for four different orientations, one zone axis condition and three different off-zone axis multi-beam conditions. Approximately 120 exact beams and 120 Bethe beams were included in the simulation. Figure 26 (a) shows the simulated CBED patterns at zone axis condition. Figure 26 (b) shows the simulated CBED pattern for the four-beam orientation where g_{100} , g_{010} and g_{110} fulfill the Bragg condition exactly (Condition I), Figure 26 (c) a simulated four-beam condition with excited g_{110} , g_{1-10} and g_{200} (Condition II) and Figure 26 (d) a simulated CBED pattern where g_{200} , g_{020} and g_{220} are in Bragg condition (Condition III). Similar to the case of the Si CBED patterns, only the center disc has a very high intensity in the zone axis pattern, while in the CBED patterns of the multi-beam off-axis CBED conditions I - III the intensity is more uniformly distributed. However, in condition I the intensity in the 100 and 010 discs is very low, resulting in very small SNR, limiting its utility for QCBED refinements. Simulated CBED patterns for condition II are of the best overall quality (Figure 26 (c)). The features in the discs show, as compared to the typical interference patterns observed in Figure 20 (a) or Figure 26 (b), very strong dynamical interactions (Figure 26 (c)).

The excitation amplitudes of Bloch waves for the four different orientations are plotted in Figure 27. In the three off-zone axis conditions more branches are excited than in the zone axis condition. Generally, the more branches are excited, the more sensitive the pattern will be to the changes in DW and/or structure factors, as the probability that at least one of the excited branches will interact with electrons that participate in interatomic bonding is increased. Hence, the off – zone axis multi beam orientations are more sensitive than the zone axis orientation patterns.

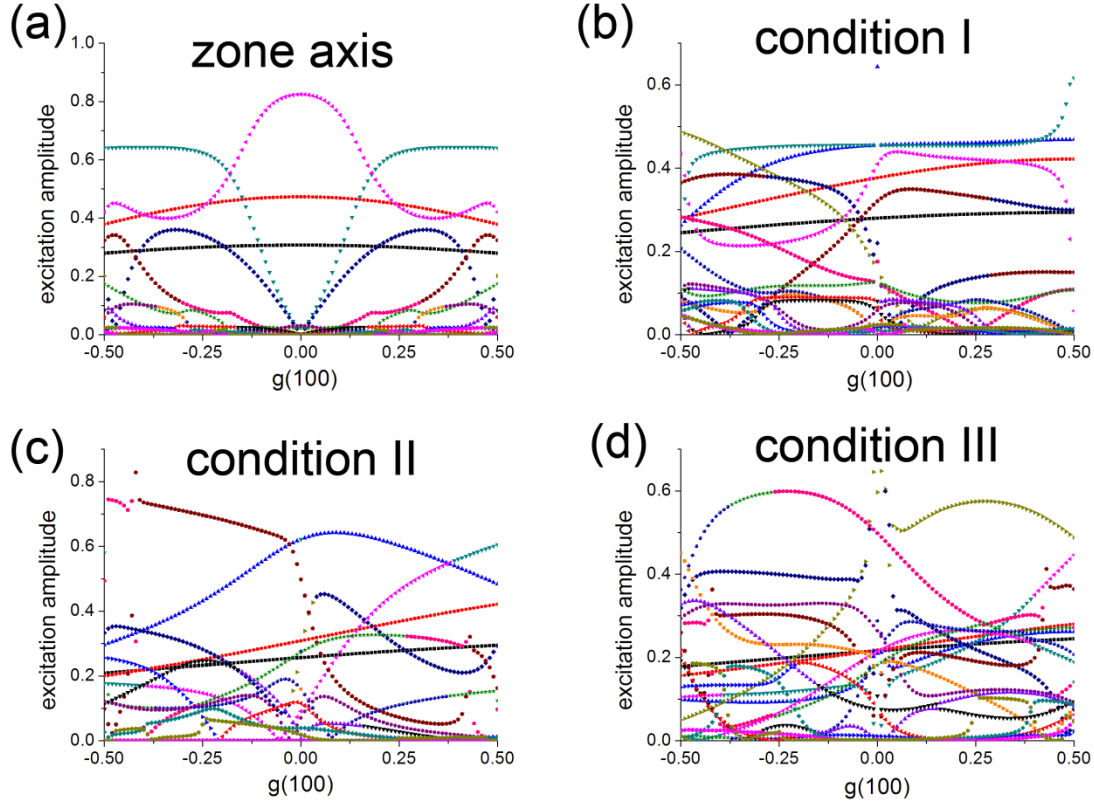


Figure 27 excitation amplitudes for NiAl zone axis condition (a) and three multi-beam conditions (b-c).

The sensitivities of the patterns for different orientations to the changes in structure factors $F_{\xi_{100}}$ and $F_{\xi_{110}}$ and DW factors $B(\text{Ni})$ and $B(\text{Al})$ are shown in Figure 28. Sensitivities are calculated using equation (39). Condition II is the most sensitive to $F_{\xi_{100}}$, $F_{\xi_{110}}$ and $F_{\xi_{200}}$. The zone axis orientation is less sensitive to changes in $F_{\xi_{100}}$, $F_{\xi_{110}}$ and $F_{\xi_{200}}$ than any of the four beam orientations. The zone axis orientation is only most sensitive to changes in DW factor for Al, B_{Al} (Figure 28 (d)). This finding contradicts a previous analysis [58], which found the zone axis orientation also insensitive to changes in B_{Al} . This apparent inconsistency can be attributed to the fact that the simulations performed here do not account for possible back-ground noise effects. In experimentally obtained CBED zone axis patterns the relatively large fractions of areas of low

intensity in the diffracted beam discs are strongly affected by noise and the small SNR for these data points deteriorates the refinement results, rendering this orientation practically insensitive to changes in DW factor amplitudes B_{Al} and B_{Ni} . Due to the improved and higher intensity in the zero disc and the diffracting discs, all off-zone-axis-multi-beam CBED conditions are affected much less by background noise as the signal to noise ratio (SNR) remains sufficiently large for the data points used in the refinements. In practice the difference between sensitivity of four beam conditions used in off-zone-axis-multi-beam CBED and sensitivity of the zone axis pattern CBED condition will be higher than indicated by the graphs in Figure 28 if the difference in uniformity of the intensity distribution in four beam condition patterns as compared to the zone axis orientation is considered. In summary, for the cases of NiAl as well as Si the superior sensitivity to changes in DW and Structure factors of the off-zone-axis-multi-beam CBED conditions relative to the zone axis orientations can be attributed to the enhanced SNR in combination with the high intrinsic sensitivity from more excited Bloch branches and uniformly distributed intensity throughout the relevant discs of the CBED pattern.

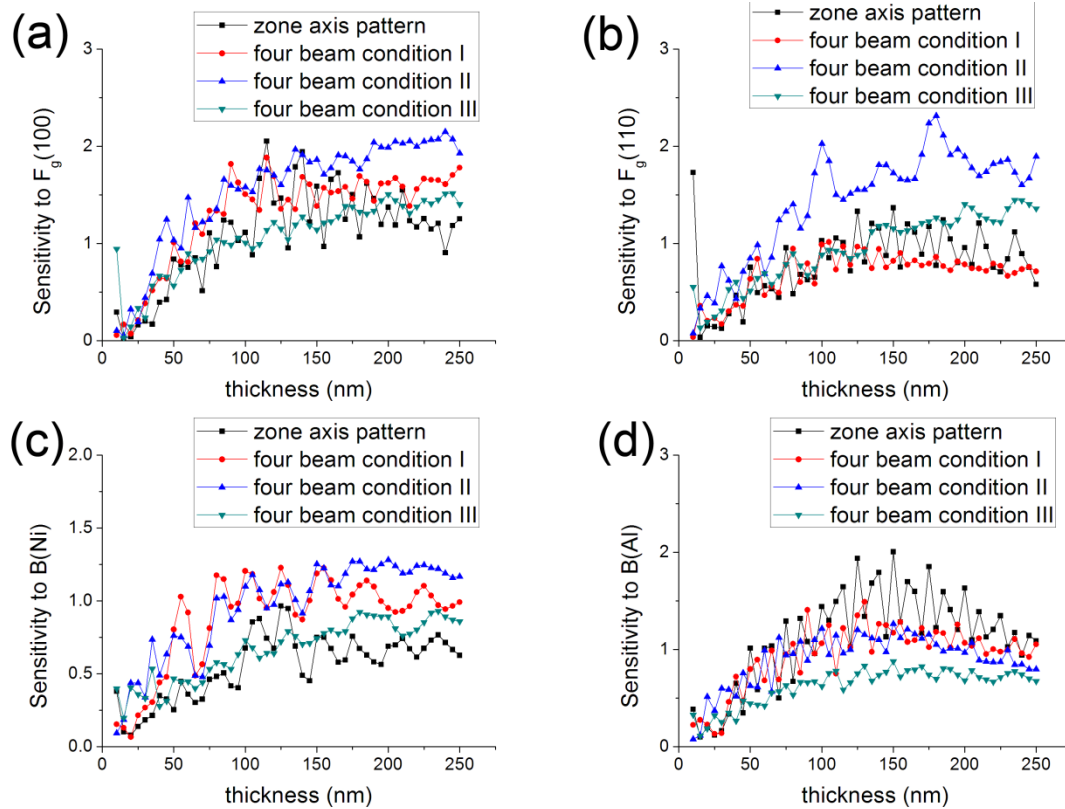


Figure 28 sensitivity of intensity distribution to change of structure factors $F_g(100)$ (a) and $F_g(110)$ (b) and DW factors $B(\text{Ni})$ (c) and $B(\text{Al})$ (d).

6.5 CONCLUSIONS

Here we systematically investigated the sensitivity of different sample beam orientations with respect to changes in structure and Debye Waller factors for two different materials by comparison of intensity changes in simulated CBED patterns using different simulation parameters, by investigation of the Bloch wave branch excitation amplitude spectra for the different beam sample orientations in combination with an analysis of Bloch wave branch probability amplitudes in real space. The different sample beam orientations are a zone axis orientation and two different off – zone axis multi – beam orientations. We found:

1. The probability of Bloch wave state interaction with bonding electrons, i.e. the CBED pattern sensitivity to changes in structure and DW factors, increases with the number and excitation of Bloch wave branches.
2. Bloch wave branches from lower parts in the dispersion surface coincide with spaces in between atoms and therefore interact with bond electrons. Strong excitation, i.e. high amplitudes of these branches increase the sensitivity of the CBED pattern to changes in structure and Debye Waller factors.
3. Sensitivity simulations showed that generally the off – zone axis multi beam orientations are more sensitive to changes in structure and Debye Waller factors, because:
 - a. In general, more Bloch wave branches are excited for off – zone axis multi beam orientations as compared to the ZAP technique.
 - b. Additionally, the excitation amplitudes of the excited beams are generally higher for off – zone axis multi beam orientations.
 - c. The off – zone axis multi beam orientation contains highly excited anti – bound Bloch wave branches with probability amplitudes that are in locations that do not coincide with atom positions in the crystal and therefore are more likely to interact with bond electrons.
 - d. Most of the excited Bloch wave branches in a zone axis pattern are bound Bloch wave branches, which coincide with atom positions and only interact with bound core electrons.
 - e. In a zone axis pattern the number of excited anti – bound Bloch wave branches is smaller as compared to off – zone axis multi beam orientation CBED patterns.

In summary, the simulations show, that in general the zone axis orientation is rather insensitive to structure factor contributions from bond electrons. The sensitivity of the off – zone axis multi beam orientations to changes in structure and Debye Waller factors proved to be much higher as compared to zone axis orientations. This finding has been attributed to a larger number of more strongly excited anti – bound Bloch wave branches. The combination of anti – bound Bloch wave excitation with a better signal to noise ratio and a more uniform intensity distribution in the CBED discs renders the off – zone axis multi beam orientation CBED patterns superior for simultaneous structure and Debye Waller factor refinement. The high sensitivity to electron beam interactions with interatomic bond electrons makes this technique ideal for investigation of interatomic bond behavior in crystalline materials.

7.0 ELECTRON DENSITY OF TIAL

This section presents and discusses the application of the new multi-beam off-zone axis QCBED method for the accurate and precise simultaneous measurement of multiple anisotropic DW and structure factors for L1₀ TiAl. The tetragonal crystal structure of L1₀ TiAl is more complex than Si and B2 NiAl, which are cubic structures. Due to the tetragonal symmetry of the L1₀-structure TiAl anisotropic DW factors have to be introduced for each of the metal elements. The magnitudes of the DW factors for each atom species differ along the crystallographically distinct [100] and [001] directions, respectively. Hence, four (two for each atom species) rather than two DW factors are required to describe this binary tetragonal phase. The accurate measurement of those four DW factors is essential for the determination of X-ray structure factors and the charge distributions [33, 57], which entails more elaborate refinement process that potentially is also applicable to L1₀ FePd and FePt.

This section of the dissertation document is based on a manuscript under review for publication to Philosophy Magazine. The high precision and accuracy (largest error < 0.5%) measurements allowed the construction of charge density difference maps from full sets of structure and DW factors, suitable for validation of first principle calculation results. Comparison of the experimentally determined charge density distribution with full electron based (LAPW – GGA PBE) ab-initio calculations shows excellent qualitative agreement. The three-dimensional charge density representations indicate a large electron charge accumulation centered about the

tetrahedral site at $\frac{1}{4}, \frac{1}{4}, \frac{1}{4}$, which is coordinated by two Ti atoms at $0, 0, 0$ and $\frac{1}{2}, \frac{1}{2}, 0$ and two Al atoms at $\frac{1}{2}, 0, \frac{1}{2}$ and $0, \frac{1}{2}, \frac{1}{2}$, respectively. First principle calculations quantitatively overestimate charge density accumulation between Ti – Ti second nearest neighbor atoms, probably due to difficulties with 3d – orbital approximations.

7.1 REFINEMENT OF ANISOTROPIC DW FACTORS

In the tp_2 description of the $L1_0$ ordered TiAl, Ti and Al atoms are at 000 (Wyckoff site a) and $\frac{1}{2}, \frac{1}{2}, \frac{1}{2}$ (Wyckoff site d), respectively. Due to the symmetry of the tetragonal unit cell, atoms on both Wyckoff sites have two different non-zero DW factors ($B_{11} = B_{22}, B_{33}, B_{12} = B_{13} = B_{23} = 0$) [170]. Therefore, four different DW factors ($B(\text{Ti})_{11}, B(\text{Al})_{11}, B(\text{Ti})_{33}$ and $B(\text{Al})_{33}$) have to be measured accurately before accurate structure factors can be determined. It proved to be very difficult to refine four DW factors simultaneously in one QCBED experiment, especially when structure factors and absorption factors are also relaxed simultaneously. Under these conditions the refinements may easily be trapped in a local minimum instead of the global minimum. To overcome this problem, we used a two-step approach to measure DW factors, in which $B(\text{Ti})_{11}$ and $B(\text{Al})_{11}$ are obtained first and $B(\text{Ti})_{33}$ and $B(\text{Al})_{33}$ later.

For a tetragonal structure, the temperature factor in the structure factor equation for a particular reflection hkl takes the form [170],

$$\exp(-Bs^2) = \exp\left(-\frac{1}{4}\left(\frac{h^2 + k^2}{a^2}B_{11} + \frac{l^2}{c^2}B_{33}\right)\right) \quad (40)$$

Along $[001]=[uvw]$ orientation, all the reflections in the zero order Laue zone (ZOLZ) of the tetragonal crystal have the form of $hk0$ and satisfy $hu + kv + lw = 0$. From equation (40) follows, when l is zero, the corresponding temperature factor is not influenced by B_{33} . Structure factors of $hk0$ for $L1_0$ TiAl are only influenced by $B(\text{Ti})_{11}$ and $B(\text{Al})_{11}$, and not by $B(\text{Ti})_{33}$ and $B(\text{Al})_{33}$. In this case only two different DW factors need to be refined, which greatly simplifies the refinement process. A more detailed example of this method will be presented when measurement of DW factors for $L1_0$ FePd is discussed in Chapter 8.0 .

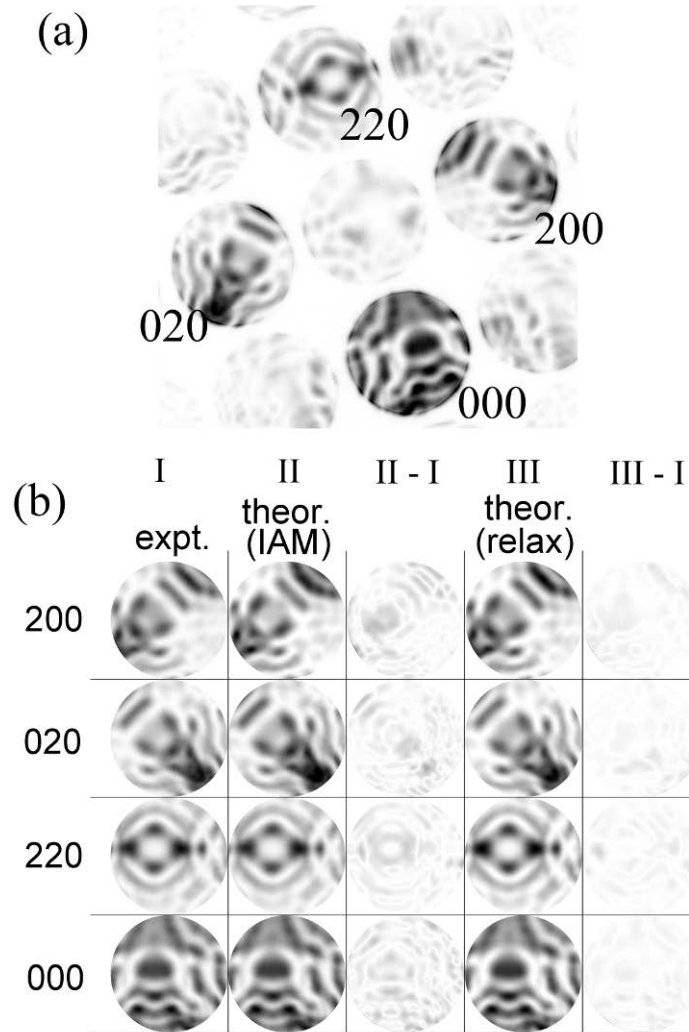


Figure 29 (a) experimental CBED pattern acquired from γ -TiAl near [001] zone axis of a thickness of 254.5nm; (b) experimental CBED discs I, simulated discs assuming IAM $F_g(hkl)$ II, difference between $F_g(hkl)_{\text{expt}} - F_g(hkl)_{\text{IAM}}$ in (II-I), and after relaxing $F_g(hkl)$ $F_g(hkl)_{\text{expt}} - F_g(hkl)_{\text{relaxed}}$ in (III-I).

7.2 RESULTS

Figure 29a shows a typical γ -TiAl CBED pattern for a beam-sample orientation close to a [001] zone axis, where the (200), (020) and (220) reflections exactly satisfy the Bragg condition, which is the most sensitive to changes of the anisotropic DW, $B_{11}(\text{Ti})$ and $B_{11}(\text{Al})$, and structure factors, $F_g(110)$ and $F_g(200)$ [58]. All strongly excited discs, which are intersected by the Ewald sphere, were included in the CBED refinement. Figure 29b shows the difference between the simulated CBED discs and the experimental CBED discs with and without relaxation of structure factors. A large reduction in the residual intensity difference between experiment and simulation, reflected in fewer features and low contrast in the respective difference maps (e.g. compare columns marked II-I and III-I in Figure 29b), can be observed after relaxing structure factors instead of using fixed independent atom model (IAM) structure factors [98], confirming the sensitivity of the four discs to changes in structure factor content and interatomic bonding information. The goodness of fit [99] improved after relaxation of low order structure factors, which is reflected in a reduction of the value R_w , from 0.24 to 0.13. $B_{33}(\text{Ti})$ and $B_{33}(\text{Al})$ were subsequently refined from CBED patterns acquired near the [110] orientation. Low order structure factors up to $hkl = 003$ were refined. For each orientation and temperature twenty to forty CBED patterns, with TEM foil section thicknesses ranging from 150nm to 400nm, were acquired, refined and the average and standard deviation of X – ray structure factors $F_{g_{hkl}}$ calculated. Anisotropic DW factors were obtained simultaneously with the low order $F_{g_{hkl}}$ from near zone axis CBED patterns for three different temperatures and are listed in Table 9. At low temperatures (96 and 173K) B_{11} is within the error about equal to $\approx B_{33}$ for both atom species. Only at room temperature a significant anisotropy develops for the thermal displacement

amplitudes of the Ti and Al atoms in the tetragonal γ -TiAl phase, with $B_{33}(\text{Ti}) > B_{11}(\text{Ti})$ and $B_{11}(\text{Al}) > B_{33}(\text{Al})$. For the temperatures below 300K the experimentally determined DW factors for Ti and Al in TiAl are in good agreement with results from molecular dynamics (MD) simulations we performed with the well-established interatomic potential [172, 178] using methods described in 2.4.2 [169-171]. Notably, the DW factors determined here for TiAl differ significantly from those determined by XRD and used in previous QCBED based structure factor determination for TiAl [38, 166].

Table 9 Experimental and theoretical DW factors

T(K)	Experimental DW factors (\AA^2)				Theoretical DW factors (\AA^2) from MD simulation			
	$B_{11}(\text{Ti})$	$B_{33}(\text{Ti})$	$B_{11}(\text{Al})$	$B_{33}(\text{Al})$	$B_{11}(\text{Ti})$	$B_{33}(\text{Ti})$	$B_{11}(\text{Al})$	$B_{33}(\text{Al})$
96	0.28(3)	0.27(2)	0.26(2)	0.24(3)	0.185	0.185	0.255	0.223
173	0.34(2)	0.37(4)	0.34(2)	0.31(5)	0.271	0.271	0.352	0.302
300	0.45(3)	0.54(5)	0.51(3)	0.45(7)	0.448	0.447	0.562	0.472

Table 10 lists static X-ray structure factors $F_{g_{hkl}}$, which are converted from $F_{g_{hkl}}$ and DW factors measured at finite temperatures. A complete set of low order structure factors up to $hkl = 003$ has been refined from CBED experiments conducted for four different zone axes of TiAl, namely [110], [101], [100] and [001] (Table 10). If a specific $F_{g_{hkl}}$ was determined from more than one zone axis orientation QCBED experiment, the $F_{g_{hkl}}$ value with the smallest uncertainty

(lowest R_w value) was selected. If specific $F_{g_{hkl}}$'s refined from different zone axes exhibited comparable uncertainty, an average value was determined and included in the set.

Table 10 Experimental and theoretical structure factors

Fg from different zone axis at different T													
hkl	96K						summary of present work	IAM	LAPW	LAPW	VASP	expt. ^a	expt. ^b
	[110]	[101]	[100]	[001]	[001]	[001]			GGA PBE	LDA PW			
001	8.03(2)		8.017(7)				8.017(7)	7.916	8.008	8.018	8.018	8.033	8.031
110	7.14(4)			7.17(4)	7.13(1)	7.10(1)	7.16(4)	7.223	7.071	7.077	7.142	7.112	7.481
111	24.28(3)	24.30(1)					24.30(1)	24.524	24.281	24.289	24.371	24.397	24.549
002	23.01(5)		22.99(4)				22.99(4)	23.245	23.027	23.018	23.132	22.933	23.007
200		22.65(2)	22.67(1)	22.67(4)	22.67(3)	22.66(2)	22.67(1)	23.031	22.717	22.715	22.813	22.571	22.005
201			5.63(3)				5.63(3)	5.649	5.602	5.595	5.646	5.640	
112	5.47(9)						5.47(9)	5.293	5.339	5.330	5.377		
202		19.23(5)					19.23(5)	19.252	19.207	19.180	19.280		19.487
220	19.08(8)			19.07(9)			19.08(9)	19.127	19.178	19.148	19.234		19.233
003	4.58(14)						4.58(14)	4.434	4.442	4.441	4.464		
R factor (%)								1.14 ^c	0.244 ^c	0.215 ^c	0.435 ^c	0.497 ^d	1.685 ^d

^aHolmestad and Birkeland (CBED with two beam condition method, experiments carried out at -150°C with B(Ti)=0.38 Å² and B(Al)=0.17 Å²) [38]

^bSwaminathan *et al.* (CBED with two beam condition method, experiments carried out at room temperature with B(Ti)=B(Al)=0.67 Å²) [166].

^cCurrent CBED F_gs as reference.

^dGGA DFT as reference.

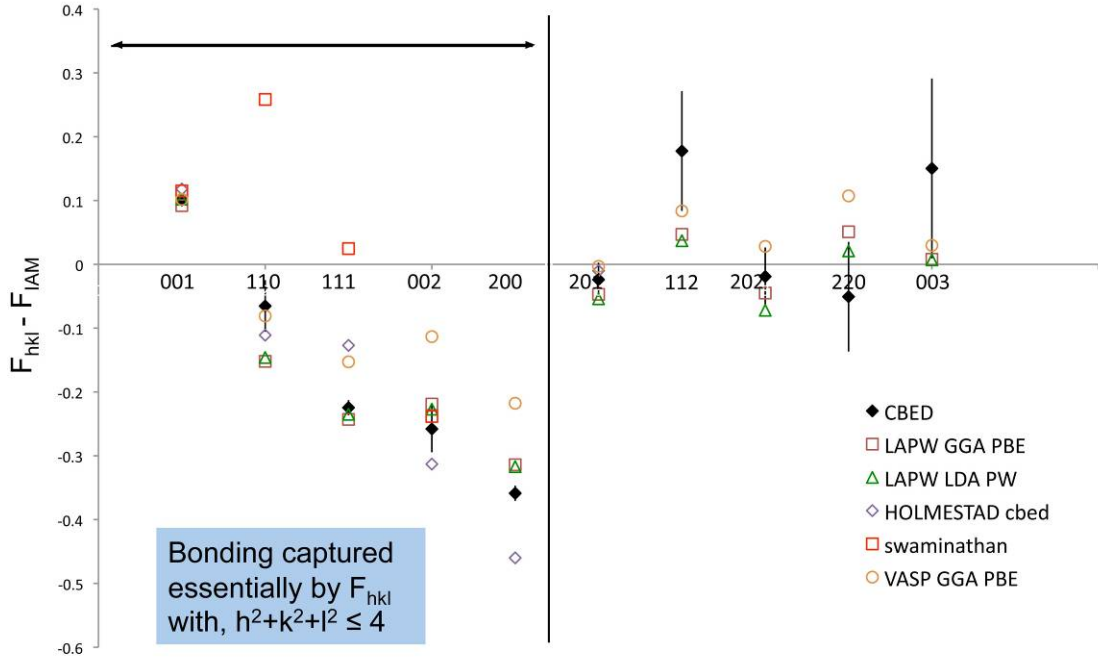


Figure 30 Comparison of $F_{hkl} - F_{IAM}$ of QCBED with other F_{hkl} measurements (Holmestad and Swaminathan) and different theoretically calculated F_{hkl}

Table 10 shows the high precision of the refined $F_{g_{hkl}}$, and the excellent accuracy, which is reflected in the consistency of data obtained from different orientations and temperatures. For example the uncertainty of $F_{g_{200}}$, which has been obtained from about ~ 100 measurements from three different zone axes and temperatures, is less than 0.05%. In Table 10 the experimentally determined $F_{g_{hkl}}$'s are compared and correlated to IAM values and structure factors determined from VASP, two LAPW (GGA PBE [177] and LDA PW [176]) based ab-initio DFT calculations and two sets of experimentally determined $F_{g_{hkl}}$'s from prior reports by Holmestad et al. [38] and Swaminathan et al. [166]. The structure factor measurements obtained in the current study by QCBED show excellent agreement with both types of LAPW based first principle calculations performed here. The correlation between the experimental measurements and the LAPW

calculation performed here is excellent, which is quantified by the small R – factor [26] $R \approx 0.2$ (Table 10, see bottom row). The correlation of the new experimental QCBED measurements with VASP based calculations is less ideal, $R \approx 0.4$, and is even worse for previously reported experimental measurements, $R \approx 0.5$ for [38] and $R \approx 1.7$ for [166] (Table 10).

Figure 30 illustrates graphically the differences between the different experimentally determined and DFT calculated sets of structure factors and those based on the IAM for hkl up to 003. The $F_{g_{hkl}}$'s measured experimentally in the current work exhibit excellent quantitative agreement within the small error ranges with the LAPW GGE PBE and LDA PW full electron based first principle DFT calculations, except for structure factors $F_{g_{110}}$ and $F_{g_{200}}$. Unlike the experimental measurements of Holmestad et al. [38], which exhibit qualitatively the same trends with respect to the IAM values as the experimental and DFT calculated structure factors obtained in the current work, the measurements reported by Swaminathan [166] are qualitatively and quantitatively significantly different from all other reports. For example, $\Delta F_{g_{110}} > 0$ in the report by Swaminathan [166], while the other experimental studies and the theoretical calculations found consistently $\Delta F_{g_{110}} < 0$ (Figure 30). For the higher order structure factors $\Delta F_{g_{hkl}}$ with $h^2 + k^2 + l^2 > 4$, which are expected to be influenced less by bonding than the low-order structure factors, the difference to the IAM values vanishes, $\Delta F_{g_{hkl}} \approx 0$, i.e. $F_{g_{hkl}}$ (measured) $\approx F_{g_{hkl}}$ (IAM). These higher-order $F_{g_{hkl}}$ also exhibit large error bars, which is a result of the large scaling factor in the Mott formula used for the conversion from electron to X – ray structure factors [49]. Hence, they will not be included for the construction of the electron charge density. Electron densities based on the experimental results, $\rho(r)^{expt}$, the DFT calculations, $\rho(r)^{theor}$, and those based on IAM approximations, $\rho(r)^{IAM}$, were calculated via Fourier transform [26], using the first

five low-order $F_{g_{hkl}}$ measured or calculated and the first five $F_{g_{hkl}}$ IAM values from Doyle and Turner [98], respectively, with $(hkl = 001, 110, 111, 002, 200)$. The electron charge density difference or electron charge density deformation was determined using $\Delta\rho = \rho(r)^{measured} - \rho(r)^{IAM}$ where the superscript ‘measured’ refers to either the experimentally determined electron density, ρ^{expt} , or that calculated by DFT, ρ^{theor} .

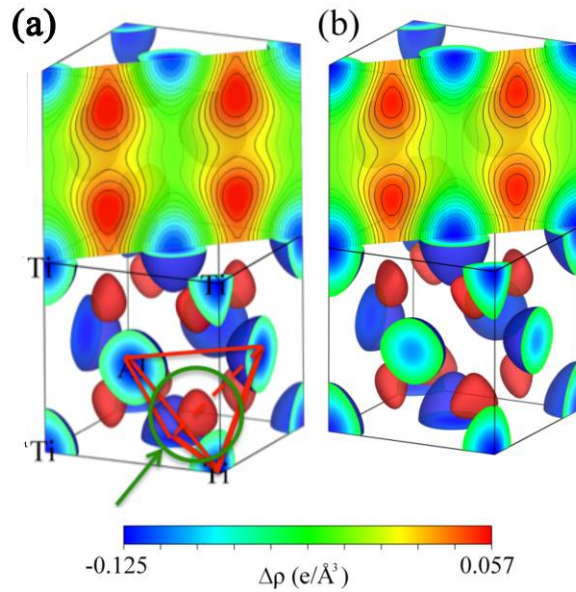


Figure 31 three-dimensional electron charge density distribution in the unit cell: a) experimentally determined (tetrahedral coordinated charge density localization); b) as calculated using LAPW GGA PBE

Figure 31 shows three-dimensional representations of the charge density differences determined from the QCBED and DFT studies performed here. Figure 31a displays the charge density difference obtained with the experimental QCBED measurements, $\Delta\rho^{expt}$. For comparison Figure 31b displays the charge density difference derived from the theoretical calculations, $\Delta\rho^{theor}$, for which the $F_{g_{hkl}}$ have been obtained with WIEN2k from LAPW GGA PBE calculations. Specifically, the electron charge density difference iso – surfaces $\Delta\rho^{expt} = 0.043e/\text{\AA}^3$ and $\Delta\rho^{theor} =$

$0.039\text{e}/\text{\AA}^3$ (both 75% of the maximum $\Delta\rho$) are shown for the fcc-related tP4 unit cell commonly used to represent the structure of L1₀ ordered γ -TiAl (Figure 31). The iso-surfaces were plotted using VESTA [185]. The maximum $\Delta\rho^{\text{expt}}$ is $0.057\text{e}/\text{\AA}^3$, located at eight tetrahedral sites of the tp4 unit cell as indicated in Figure 31a. The minimum $\Delta\rho^{\text{expt}}$ is $-0.125\text{e}/\text{\AA}^3$, at the Ti atom sites. Electron charge transfers from the two Ti atoms at $0, 0, 0$ and $1/2, 1/2, 0$ and the two Al atoms at $1/2, 0, 1/2$ and $0, 1/2, 1/2$, which form a tetrahedron (red schematic in Figure 31a), into the interstitial sites at $1/4, 1/4, 1/4$ (green circle in Figure 31a) and equivalent locations. While the three-dimensional electron charge density deformation representations in Figure 31a and b show excellent qualitative agreement between the QCBED experiments and the DFT calculations, quantitative differences are manifest in $(\Delta\rho^i)_{75\%}$, i.e., $(\Delta\rho^{\text{expt}})_{75\%} = 0.043\text{e}/\text{\AA}^3$ and $(\Delta\rho^{\text{theor}})_{75\%} = 0.039\text{e}/\text{\AA}^3$. Additionally, compared to the DFT calculated representation (Figure 31b) the experimentally determined charge density difference (Figure 31a) the electron charge density localization exhibits a slightly more pronounced elongation along the [001] direction. This break in cubic symmetry in the form of an elongation of the charge density accretion that is localized along the [001] direction is in good agreement with the larger than unity c/a ratio of the tetragonal L1₀ ordered γ – TiAl. The excellent qualitative agreement for the QCBED and DFT derived charge density in TiAl is illustrated further in the planar sections for the (110) planes in Figure 31a and b. However, planar sections of the charge density difference distribution also reveal the slight quantitative differences between the QCBED experiments and the DFT calculations. In the planar sections of Figure 31 and Figure 32 the solid black lines and the color red is used in regions with $\Delta\rho > 0$ (i.e., electronic charge accumulation relative to the IAM) and gray dashed lines and blue are used in regions with $\Delta\rho < 0$ (i.e., electronic charge depletion relative to the IAM). The first dark line delineates the surface with $\Delta\rho = 0$. The step between

adjacent contour lines is $0.01e/\text{\AA}^3$. Figure 32 compares the (001), (004), (002) and the (400) planar sections of the charge density deformation from the QCBED measurements and the LAPW GGA PBE calculations. Figure 32a illustrates the relative locations and orientation of the planar sections of the charge density deformation in the TiAl unit cell. The (002) and (400) planar sections in Figure 32b and c show excellent qualitative and quantitative agreement.

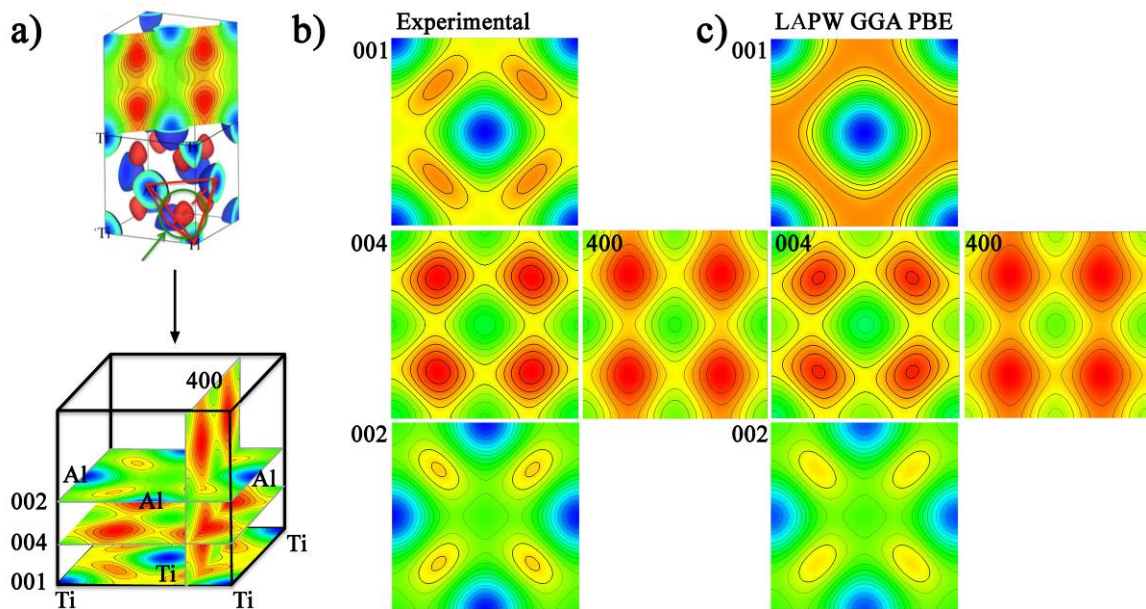


Figure 32 001, 004, 002 and 400 two – dimensional planar sections of the electron charge density distribution in the unit cell (illustrated in a)): b) experimentally determined; c) as calculated using LAPW GGA PBE

Qualitative differences can be observed clearly in the (004) planes. The electron charge density localization in the experimentally determined electron charge density deformation assumes a square shape, whereas it is more rectangular in the theoretically determined charge density deformation. The largest quantitative differences can be observed in the (001) plane sections (Figure 32b and c). The theoretically calculated map shows elevated electron charge density accumulation between second nearest neighbor Ti atoms and reduced amounts of accumulated charge between first nearest neighbor Ti atoms as compared to the experimental

measurement based map (Figure 32b and c). In summary, as would be expected from the excellent correlation of the respective structure factors determined from experimental QCBED measurement and LAPW calculations, the corresponding electron charge density deformation for TiAl also exhibits excellent qualitative agreement between experiment and theory but shows quantitative differences, which manifest themselves most pronounced in the (001) planar section.

7.3 DISCUSSION

The results reported in Table 9 and Table 10 represent the highest precision and accuracy structure factor and DW factor data for $L1_0$ ordered tetragonal γ - TiAl determined experimentally to date. The refinements show excellent internal consistency, i.e., the error of structure factors with $h^2+k^2+l^2 \leq 4$ determined from up to 100 CBED patterns recorded from up to 5 different near zone axis orientations, various different thicknesses and up to three different temperatures, never exceeds 0.56% ($F_{g_{110}}$) and can be as small as 0.04% ($F_{g_{002}}$). The Debye Waller temperature factors determined here simultaneously with the structure factors from QCBED data exhibit a small error of about 6 to 15%. The accuracy and precision of the DW factor measurements is at least as good as or much better than prior DW factor measurements obtained by X – ray diffraction, where errors between 6% and 60% have been reported [48, 186] and sufficient to allow more accurate investigations of bonding effects in TiAl than previously possible. XRD probes much larger sample volumes than CBED, which for most crystalline materials include ill-defined quantities of different types of crystal imperfections and result in an associated increase of the measurement uncertainty. The simultaneous measurement of DW factors and structure factors by QCBED from the same sample volume in a single experiment

circumvents the problems with increased uncertainty in electron density determination associated with use of DW factors obtained from separate XRD experiments [38, 166].

Figure 30, Figure 31 and Figure 32 present graphically a comparison of the charge density differences obtained with different first-principles ab-initio DFT calculations and from QCBED experiments. The QCBED measurements performed here, some prior experimental work [38] and the LAPW based first-principles ab-initio calculations show good qualitative agreement but exhibit some quantitative differences. The qualitatively and quantitatively different structure factors reported by Swaminathan et al. [166] (see Table 10 and Figure 30) may be attributed at least partly to use of a single isotropic temperature factor, DW factor, for both the Ti and Al atoms in TiAl. The current experimental structure factor measurements exhibit significantly reduced error margins as compared to previous QCBED measurements for TiAl and are therefore better suited for comparison with and validation of results calculated by DFT methods.

Unlike full-electron based ab-initio DFT, the VASP calculation produce good agreement with the current QCBED experiments only for $F_{g_{001}}$ and $F_{g_{110}}$ (Table 10, Figure 30). For higher-order $F_{g_{hkl}}$ with $h^2 + k^2 + l^2 > 2$, e.g. already for $F_{g_{111}}$, the VASP results deviate significantly. This is not surprising as VASP uses a mean-field approximation for the core electrons, only treats the bond electrons properly [187-191] and hence fails to calculate correctly the $F_{g_{hkl}}$'s that are affected by core electrons, which for TiAl includes $F_{g_{111}}$ and higher-orders with $h^2 + k^2 + l^2 > 2$. Our measurements therefore show that VASP can treat bond electrons and effects, materials properties that entirely depend on bonding quite well. Consequently, comparison with our measurements suggests, that care has to be taken with the use of VASP calculations to describe

phenomena that not only involve bond but also core electrons. For proper description of materials properties of TiAl that involve core electrons in addition to bond electrons full-electron based techniques should be used.

The two different types of full-electron based LAPW first-principles ab-initio calculations correlate best with the current experimental QCBED measurements, which is reflected in R values of about 0.22 to 0.24 in Table 10. Especially the structure factors $F_{g_{001}}$, $F_{g_{111}}$ and $F_{g_{002}}$ exhibit excellent agreement (Table 10, Figure 30). The quantitative differences that can be observed in $F_{g_{110}}$ and $F_{g_{200}}$ manifest themselves most clearly in the two- and three-dimensional charge density deformation map representations as an overestimation of charge density localization in between second nearest neighbor Ti atoms (Figure 31 and Figure 32). This might stem from the well-known problems of DFT methods with the proper description of d – orbital interactions [192]. The three-dimensional representation of electron charge density deformation iso – surface in the unit cell representation of Figure 31a, which has been constructed from the experimentally measured $F_{g_{hkl}}$'s, shows an electron charge localization at the tetrahedral site $\frac{1}{4}, \frac{1}{4}, \frac{1}{4}$, which is coordinated by two Ti atoms at $0, 0, 0$ and $\frac{1}{2}, \frac{1}{2}, 0$ and two Al atoms at $\frac{1}{2}, 0, \frac{1}{2}$ and $0, \frac{1}{2}, \frac{1}{2}$, and electron charge density depletion at the atomic sites. Furthermore, the charge density accumulation is interconnected throughout the crystal with channels of excess electronic charge density clearly discernible in the (110) and (400) planar sections for instance (Figure 31 and Figure 32). The charge density deformation for TiAl shares many characteristics with and qualitatively resembles that observed in pure Al [36]. However, consistent with the tetragonal symmetry of TiAl and a unit cell where the $c/a > 1$, e.g. $c/a \sim 1.02$ to 1.04 [193] the charge density localization exhibits a tetragonal distortion along the [001]

direction. Since Al could be considered as an example for an archetypical elemental metal with presumably metallic type bond character and given the similarities of the respective charge density deformations, it is tempting to speculate that TiAl exhibits largely metallic bond character. However, in the absence of standard representations for metallic or covalent or ionic character bonds in terms of charge density deformations it remains difficult to conclude regarding the characterization of the nature of the bonding in the intermetallic in these textbook terms. Comparison of the experimentally determined charge density deformation densities with those calculated using the full electron LAPW GGA PBE based Wien 2k simulation package reported here (Figure 31 and Figure 32) show excellent qualitative agreement but also some quantitative differences. The all Al plane, i.e. the (002) planar section (Figure 32b and c) shows excellent qualitative and quantitative agreement between experiment and theory, reflecting the capability of DFT calculations to describe s and p orbital interactions very well [192]. The (110) planar section of the charge density deformation also shows very good qualitative and reasonable quantitative agreement and displays the elongation of the electron charge localization along the [001] direction. The largest difference between DFT calculations and QCBED measurements can be seen in the (001) plane. The theoretically constructed electron charge density difference map exhibits an overestimation of electron charge density localization between second nearest neighbor Ti atoms, which can probably attributed to the difficulties with orbital interactions that involve d – d interactions [192].

The improved accuracy and precision of the QCBED measurements performed here are sufficient to construct electron charge density deformation maps, suitable to reveal shortcomings of different theoretical first principle density functional theory based calculations. Taken together with recent work of Nakashima et al. [36] and Sang et al. in [57, 58, 140], the present study

demonstrates that prior knowledge of DW factors and higher order $F_{g_{hkl}}$ with $h^2 + k^2 + l^2 > n$ ($n =$ integer number for $F_{g_{hkl}} = F_{g_{hkl}}^{IAM}$; Generally for most metals bcc and fcc and alloys $n = 4$ [36, 50, 57, 58, 140]), as determined for example by X – ray techniques, is not necessary for determination of highly precise and accurate electron density distributions from nano-scale volumes, $\approx 150 - 200 \text{ nm}^3$, of materials of known crystal structure using a field emission TEM equipped with a post column energy filter by for simultaneous structure and DW factor measurements.

7.4 SUMMARY AND CONCLUSIONS

QCBED has been used to measure high accuracy and precision structure and temperature or DW factors of $L1_0$ ordered tetragonal γ -TiAl at three different temperatures. Based on these measurements quantitative electron charge density deformation maps have been constructed. The results from the experimental QCBED have been compared to predictions obtained from electronic structure calculation based on different DFT methods. Hence, the experimental data reported here has been compared to prior experimental measurements and was suitable for quantitative comparison with DFT predictions for TiAl. The main conclusions can be enumerated as follows:

1. The high accuracy and precision of the structure and Debye Waller factors measured here by QCBED for TiAl allowed construction of electron charge density deformation maps suitable for the validation of first principle DFT calculations.
2. Comparison of the current QCBED results with previously reported experimental findings highlighted the advantages of simultaneous refinement of structure and DW

factors from the same sample volume in order to improve precision and accuracy of both structure and DW factors.

3. Structure factors, $F_{g_{hkl}}$, with $h^2 + k^2 + l^2 \leq 4$, i.e., F_{001} , F_{110} , F_{111} , F_{200} and F_{002} , contain essentially all the bonding related information in TiAl and are therefore sufficient to construct accurate electron charge density deformation maps..
4. Comparisons of $F_{g_{hkl}}$ calculated from VASP based DFT calculations with QCBED measurements showed good qualitative and quantitative agreement only for low-order $F_{g_{hkl}}$'s that are mainly influenced by bond electrons. For TiAl VASP fails to describe $F_{g_{hkl}}$'s of higher order than F_{111} . Predictions of material properties that are also affected by core electrons obtained from VASP may therefore be of limited accuracy.
5. Electron charge density deformation maps showed droplet shaped electron charge density localization in the tetrahedral site $\frac{1}{4}, \frac{1}{4}, \frac{1}{4}$ with an elongation in the [001] direction. This charge density accumulation is shared by two Ti atoms at $0, 0, 0$ and $\frac{1}{2}, \frac{1}{2}, 0$ and two Al atoms at $\frac{1}{2}, 0, \frac{1}{2}$ and $0, \frac{1}{2}, \frac{1}{2}$.
6. Comparison of electron charge density deformation maps constructed from QCBED measurements and those obtained from full electron LAPW GGA approximation DFT calculations exhibited excellent qualitative agreement. DFT calculations overestimated charge density localization between Ti second nearest neighbors, which is probably caused by and reflecting the difficulties of full electron based first principle DFT calculations with d – d orbital descriptions.

Excellent results from comparative study for $L1_0$ TiAl inspire us to further investigate more complex system ferromagnetic tetragonal transition-metal based binary intermetallics $L1_0$ FePd and FePt.

8.0 DW FACTORS AND STRUCTURE FACTORS OF L1₀ FE₂PD

This chapter presents and discusses the application of the new multi-beam off-zone axis QCBED method for the accurate and precise simultaneous measurement of multiple structure factors and DW factors for FePd with the L1₀ structure in Strukturbericht notation. This section of the dissertation document is based on a manuscript published in Acta Crystallographica A67 (2010) p229 entitled “Simultaneous determination of highly precise Debye-Waller factors and multiple structure factors for chemically ordered tetragonal FePd” by X. H. Sang, A. Kulovits and J. M. K. Wiezorek.

L1₀ FePd is a strong ferromagnetic intermetallic phase, which depending on the orientation of the crystalline lattice with respect to the incident beam can lead to large distortions in experimental CBED patterns, thereby complicating the refinement for structure factor measurements. Additionally, similar to L1₀ TiAl, due to the tetragonal symmetry of the L1₀-structure of the γ_1 -phase FePd, two different anisotropic DW factors have to be introduced for each of the transition metal elements. The values of the DW-factors for the Fe and Pd atoms in the chemically ordered γ_1 -phase FePd are predicted to differ significantly from those known for these atoms in the respective elemental transition metals in their stable crystalline structures at a given temperature due to effects from intermetallic bonding. Using the DW factor values known for the elemental crystals, e.g. at room temperature for Fe, $B(\text{Fe}) = 0.35\text{\AA}^2$, and Pd, $B(\text{Pd}) = 0.45\text{\AA}^2$ [95], as starting values may introduce significant uncertainty in computational

refinements for structure factors determination. As only a few percent $\sim 1 - 3\%$ of the total electron charge distribution made up of 72 electrons (Fe^{26} , Pd^{46}) present in L1_0 ordered FePd are expected to contribute to the intermetallic bond, the errors of the measurement after refinement have to be less than 0.1% for structure factors to yield meaningful electron charge distributions.

Highly accurate and precise DW factors and multiple structure factors from CBED experiments utilizing off-zone axis multi-beam orientations that we described in the previous chapters have been simultaneously obtained. The complete sets of DW and large sets of both electron and X-ray structure factors with unprecedented accuracy and precision can be used for electron charge density distribution determination.

8.1 RESULTS

8.1.1 Anisotropic DW factors of L1_0 FePd

The two-step method described in 7.1 was used to obtain four anisotropic DW factors for L1_0 FePd. Off-zone axis multi-beam condition CBED patterns from different sample thicknesses acquired from near $[001]$ orientations were used to obtain $B(\text{Fe})_{11}$ and $B(\text{Pd})_{11}$. Similar to the case of B2-ordered NiAl [58], we chose a multi-beam orientation that is sensitive to both DW factors and structure factors. In this condition, 200, 020 and 220 reflections fulfill Bragg's law exactly (Figure 33 (a)). Those three beams are strongly excited and dynamical interactions among them and the transmitted beam make the intensity distribution in those patterns sensitive to DW factors and simultaneously the respective structure factors. The refinement was carried

out by relaxation of $B(\text{Fe})_{11}$ and $B(\text{Pd})_{11}$ along with the low order structure factors 110 and 200. The inclusion of 220 in the refinement was shown to cause large scatter of the resulting DW factors and was therefore not included. Based on convergence criteria, approximately 315 exact beams and 194 Bethe beams were included to ensure that the truncation error caused by an insufficient number of beams is negligible. The resulting values of $B(\text{Fe})_{11}$ and $B(\text{Pd})_{11}$ from CBED patterns acquired at different sample thicknesses are shown in Figure 34 (a). The R_w values for those refinements are generally lower than 0.15 with some as low as 0.1. Average values for $B(\text{Fe})_{11}$ and $B(\text{Pd})_{11}$ are $0.30(2) \text{ \AA}^2$ and $0.20(2) \text{ \AA}^2$, respectively. The results presented in Figure 34 (a) are very stable. Stable results from different sample thickness indicate the reliability of this QCBED method. According to the Bloch wave formalism, DW and structure factors should be independent of sample thickness. However, due to sample contamination and other problems other QCBED methods, like the excited row QCBED method, have not been capable to obtain stable DW factors from thick areas ([166]).

CBED Patterns near [110] orientation (Figure 33 (b)) were acquired subsequently to obtain $B(\text{Fe})_{33}$ and $B(\text{Pd})_{33}$. This multi-beam condition includes simultaneously excited $\bar{1}\bar{1}\bar{1}$, 002 , $\bar{2}\bar{2}\bar{2}$, $\bar{2}\bar{2}0$ and $\bar{1}\bar{1}3$ reflections. In the refinement, $B(\text{Fe})_{33}$ and $B(\text{Pd})_{33}$ and six low order structure factors were relaxed simultaneously while $B(\text{Fe})_{11}$ and $B(\text{Pd})_{11}$ were fixed to the values obtained above. Approximately 286 exact beams and 207 Bethe beams were included to ensure that the truncation error caused by an insufficient number of beams is negligible. Figure 34 (b) shows stable $B(\text{Fe})_{33}$ and $B(\text{Pd})_{33}$ obtained from different sample thicknesses. The average values for the anisotropic magnitudes $B(\text{Fe})_{33}$ and $B(\text{Pd})_{33}$ are $0.21(3)\text{\AA}^2$ and $0.31(5)\text{\AA}^2$, respectively.

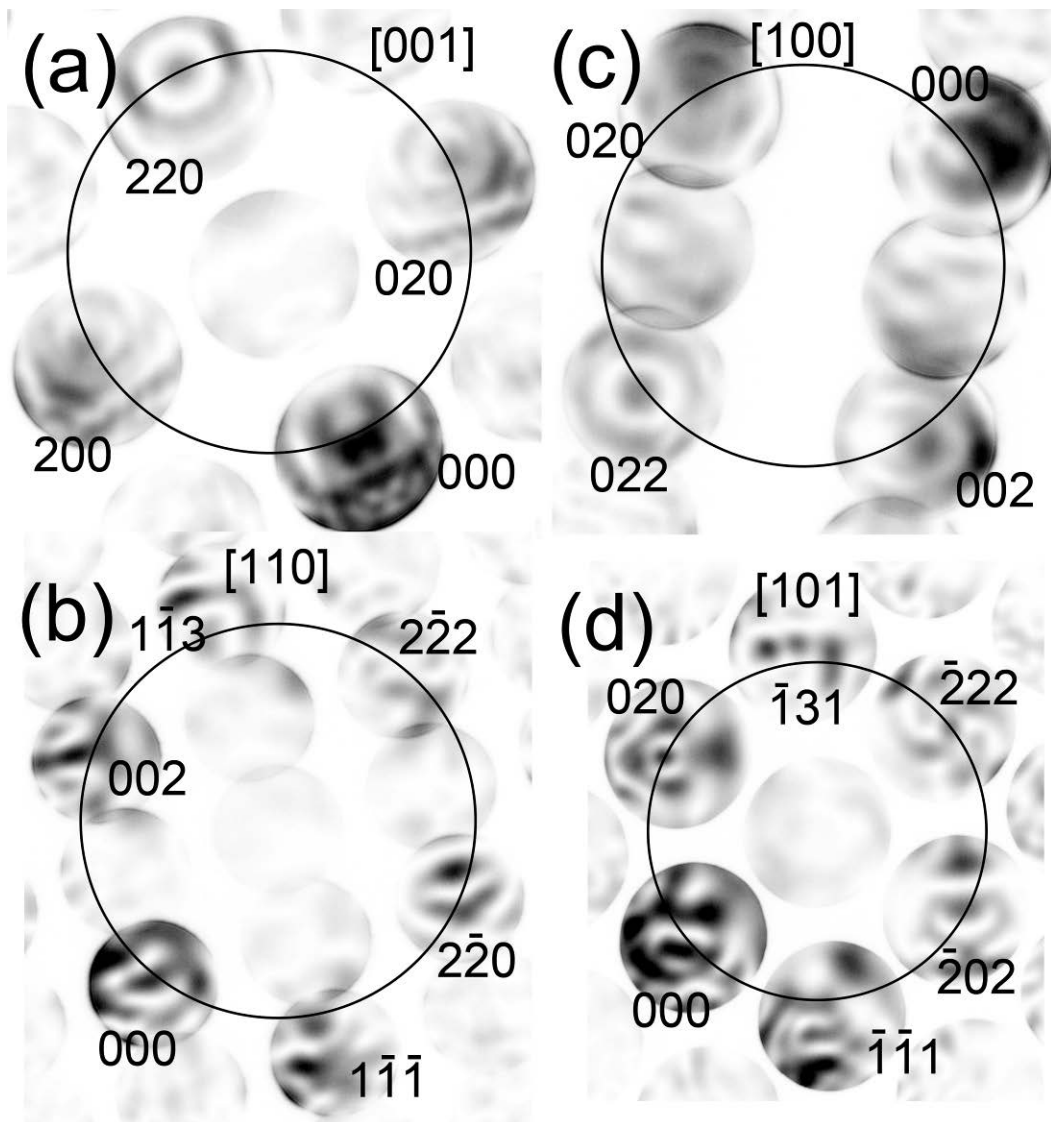


Figure 33 Off-zone axis multi-beam condition patterns acquired near (a) [001], (b) [110], (c) [100] and (d) [101] orientations. The circle in each pattern represents the trace of Ewald sphere intersecting zone order plane in reciprocal space.

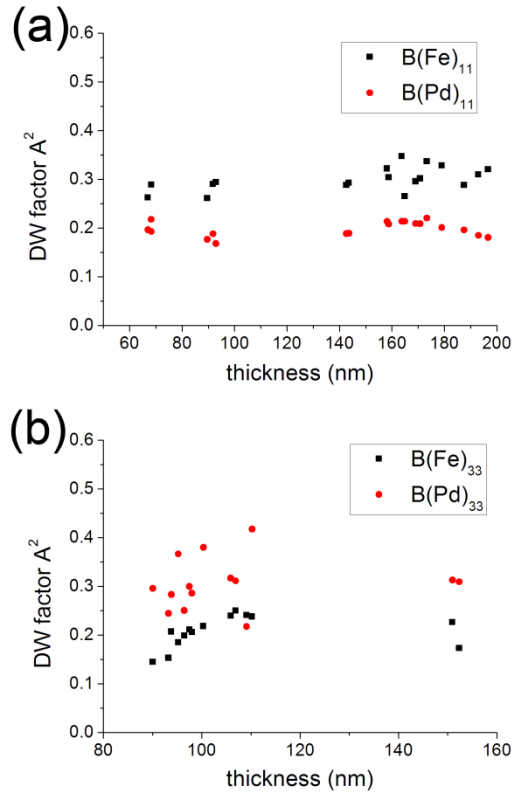


Figure 34 Refined DW factors for Fe and Pd. (a) $B(\text{Fe})_{11}$ and $B(\text{Pd})_{11}$ versus thickness, (b) $B(\text{Fe})_{33}$ and $B(\text{Pd})_{33}$ versus thickness.

8.1.2 Structure factors

Electron structure factors are subsequently refined using the experimentally measured DW factors, which are fixed during refinements, as it yields more stable refinement results. I.e. the resulting electron structure factors are the same as structure factors obtained with simultaneously refined DW factors, however the scatter is smaller. CBED patterns from four low index orientations [001], [110], [100] and [101], which can provide low order structure factors up to 222, were acquired. Off-zone axis multi-beam orientation patterns for $L1_0$ FePd along different orientations are shown in Figure 33.

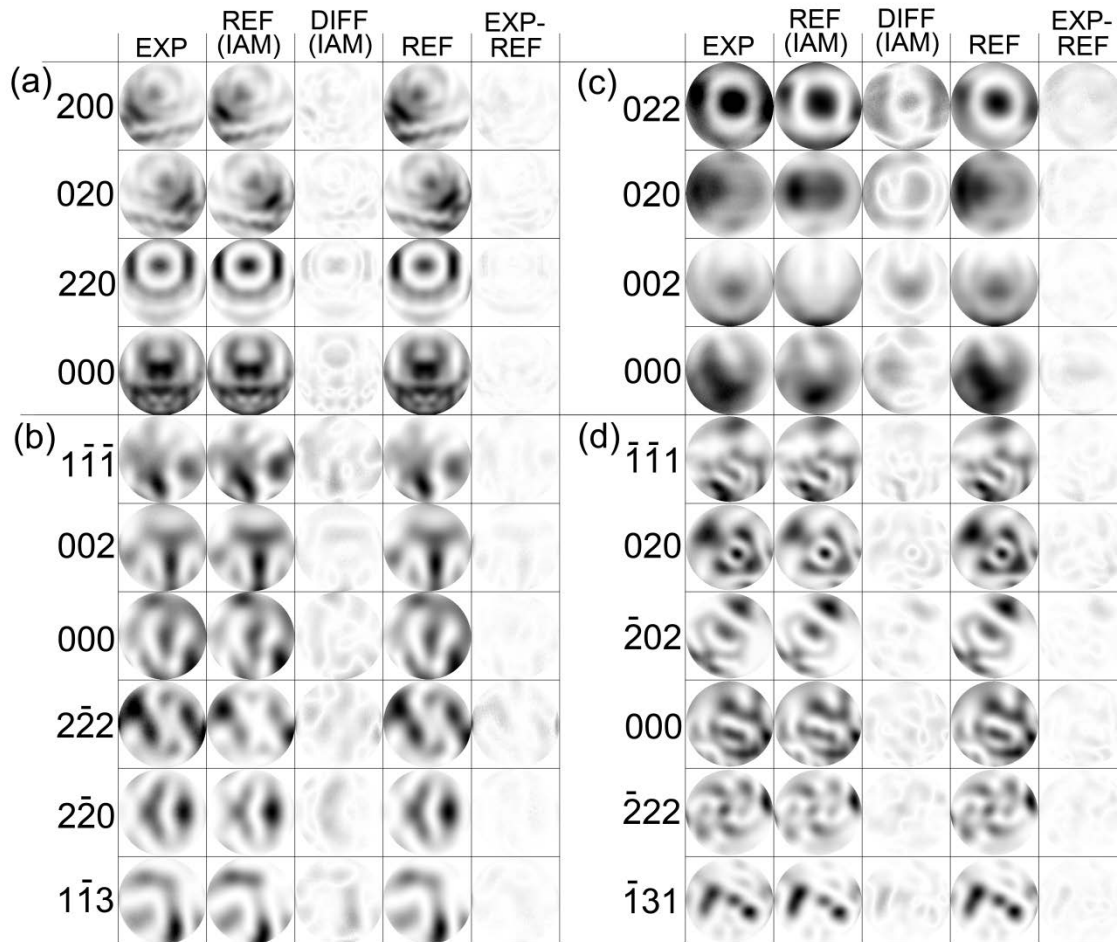


Figure 35 Refinement results of CBED patterns recorded from different orientations. The first column in each part shows experimental discs. The second column shows calculated discs by using obtained DW factors and assuming IAM. The fourth column shows calculated discs by relaxing structure factors and fixing DW factors. The third column and the fifth column show absolute value of deviation between column 1 and column 2, and between column 1 and column 4, respectively.

Discs, which intersect the Ewald sphere, are strongly excited and therefore used in the refinement. For patterns near [001] orientation, 200, 020 and 220 reflections are excited. For patterns near [110] orientation, $\bar{1}\bar{1}\bar{1}$, 002, $\bar{2}\bar{2}\bar{2}$, $\bar{2}\bar{2}\bar{0}$ and $\bar{1}\bar{1}\bar{3}$ reflections are excited. For patterns near [100] orientation, 002, 020 and 022 reflections are excited. For patterns near [101] orientation, $\bar{1}\bar{1}\bar{1}$, 020, $\bar{2}\bar{0}\bar{2}$, $\bar{2}\bar{2}\bar{2}$ and $\bar{1}\bar{3}\bar{1}$ reflections are excited. Intensity distributions in those patterns are very sensitive to the changes in structure factor content of strongly excited

reflections. The comparison of experimental acquired CBED disks with simulated discs after refinements is shown in Figure 35.

Each CBED pattern was refined two times. In the first refinement, structure factors were approximated with IAM values and fixed. In the second refinement, the structure factors were included using IAM values as starting values and relaxed during the refinement. The inclusion and relaxation of structure factors in the refinement improves the quality, reflected in a decrease of R_w values from 0.14, 0.28, 0.39 and 0.20 to 0.11, 0.14, 0.14 and 0.14 for Figure 33 (a-d), respectively. All the refinements have been greatly improved by relaxing low order structure factors, indicating that these structure factors are greatly influenced by bonding. Unlike in the excited row method, where changes in structure factor mainly causes changes in peak intensity but not in peak position [49], here in the off-zone axis multi-beam conditions, the two dimensional features change significantly if structure factors change, as can be seen clearly in Figure 35 (c). The features in the third column in Figure 35 (c) show that the IAM approximation fails for $L1_0$ FePd. This beam orientation is capable of detecting minute change of structure factors. The refined thicknesses are 143.65nm, 97.32nm, 146.67nm and 78.83nm for Figure 33 (a-d) respectively.

Figure 36 shows how the experimentally obtained structure factors vary with sample thicknesses. Both 110 and 200 structure factors are stable over a large sample thickness range.

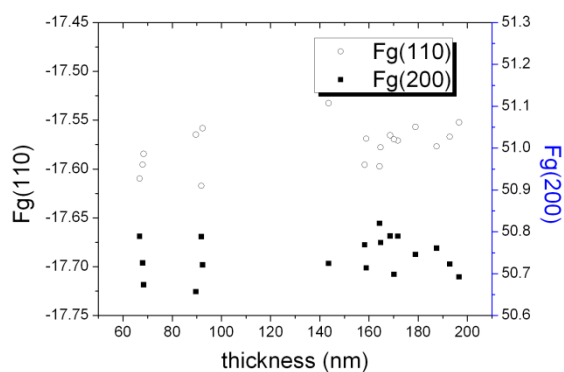


Figure 36 Refined structure factors versus thickness for patterns acquired near [001] zone axis (left axis: Fg(110), right axis: Fg(200)).

Table 11 Electron structure factors, U_g , of $L1_0$ FePd refined from different zone axes and comparison with independent atom model (IAM) values

	<110>	<101>	<100>	<001>	
Family of g contained in the zone <uvw>	$U_g (\text{\AA}^{-2})$	$U_g (\text{\AA}^{-2})$	$U_g (\text{\AA}^{-2})$	$U_g (\text{\AA}^{-2})$	$U_g (\text{IAM}) (\text{\AA}^{-2})$
001	-0.0303(9)		-0.0293(4)		-0.0236
110	-0.0287(7)			-0.0273(2)	-0.0266
111	0.1309(5)	0.1301(3)			0.1274
200		0.1164(4)	0.1166(5)	0.1154(3)	0.1141
002	0.1129(4)		0.1121(7)		0.1103
201			-0.0210(9)		-0.0227
112	-0.0196(6)				-0.0201
220	0.0815(9)			0.0797(5)	0.0804
202		0.0772(5)			0.0785
221	-0.0151(8)				-0.0169
003	-0.0144(7)				-0.0152
130				-0.0145(7)	-0.0160
131		0.0650(3)			0.0657
113	0.0632(5)				0.0632
222	0.0604(6)	0.0599(4)			0.0612
400		0.0504(8)		0.0496(14)	0.0508

Table 12 X-ray structure factors of L1₀ FePd refined from different zone axes and comparison with independent atom model (IAM) values

	<110>	<101>	<100>	<001>	
Family of g contained in the zone <uvw>	F _g ^x (IAM)				
001	-18.44(4)		-18.47(2)		-18.738
110	-17.45(6)			-17.58(2)	-17.634
111	53.53(7)	53.64(4)			54.006
200		50.56(6)	50.53(9)	50.74(5)	50.951
002	49.51(7)		49.6(1)		49.929
201			-15.1(2)		-14.732
112	-13.93(16)				-13.803
220	41.3(3)			41.9(2)	41.705
202		41.5(2)			41.078
221	-13.6(3)				-12.980
003	-12.7(3)				-12.226
130				-13.5(3)	-12.787
131		37.5(1)			37.110
113	36.3(3)				36.172
222	36.0(3)	36.2(2)			35.578
400		32.4(5)		32.9(9)	32.128

Electron structure factors are listed in Table 11. X-ray structure factors were converted from electron diffraction structure factors using the Mott formula [49] and measured DW factors. Table 12 shows a comparison of X-ray structure factors with IAM values, which shows that low order structure factors are within the error significantly different from IAM structure factors. Even some higher order structure factors, e.g. F₂₂₂, still exhibit significant differences from the IAM approximation, indicating that charge transfer and localization could possibly affect even higher order structure factors. This effect is graphically illustrated in Figure 37. The difference between measured electron structure factors and IAM electron structure factors along with standard deviations is plotted in Figure 37 (a) for each reflection. Standard deviations are

calculated for each structure factor and represented as an error bar. A similar plot for X-ray structure factors is shown in Figure 37 (b).

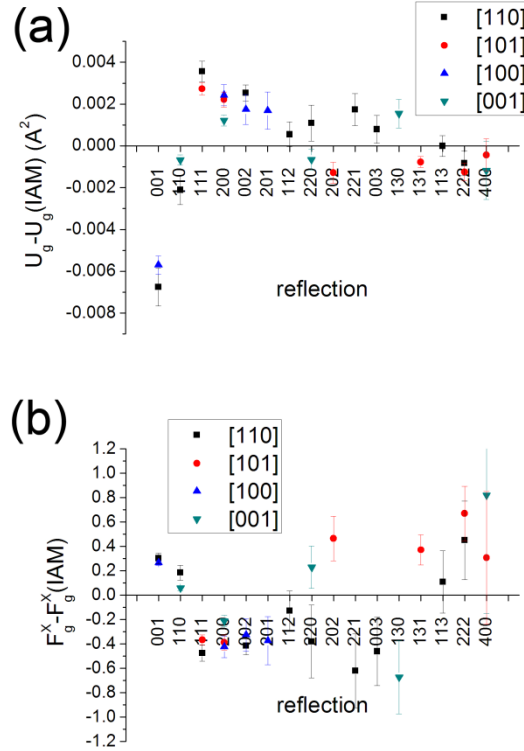


Figure 37 Difference between measured electron structure factors U_g and IAM values U_g (IAM) versus reflection g_{hkl} (a) and difference between measured X-ray structure factors F_g^X and IAM values F_g^X (IAM) versus reflection g_{hkl} (b).

Figure 37 (a) and (b) show that for low order reflections, generally the standard deviation is less than the difference between the experimental value and the IAM value (the error bar does not intersect with the X - axis). The standard deviation for electron structure factors is very small for low order structure factors since the pattern is more sensitive to changes of low order structure factors than to higher order structure factors. This trend is magnified in X-ray structure factors, because in the Mott formula used for conversion from electron to X-ray structure factors

the scaling factor s^2 is included, which significantly increases the error for high order reflections. As can be seen from Table 12, the accuracy of structure factors for 001, 110, 111 and 200 is as high as 0.1%, while for the higher order reflections, such as 113 and 222, the accuracy is reduced to on the order of 1%.

8.2 DISCUSSION

8.2.1 Sensitivity to DW factors

Generally, QCBED patterns are not as sensitive to the changes in DW factors as to changes in structure factors. As the determination of DW factors is achieved through refinement of high order electron structure factors, the sensitivity to changes of DW factors depends on the sensitivity of the CBED pattern on changes to high order electron structure factors. Since low order reflections are excited more strongly than high order reflections, CBED patterns are more sensitive to changes in low order structure factors than to changes in DW factors. The accuracy in refinements for structure factors can be as high as 0.1%, while for the DW factors the accuracy of the refinements remains always on the order of 10%. For this reason previous efforts to determine DW factors by QCBED remained unsuccessful [54]. It is essential to select an orientation, which yields DW factors that are as stable as possible. In the following discussion we assume isotropic DW factors, as the sensitivity of the four independent DW factors cannot be graphically represented conveniently. However, the general trend observed for isotropic DW factors holds true also for anisotropic DW factors (observed in refinement, not shown here). Assuming isotropic DW factors, 19 patterns near [001], 14 patterns near [110], 28 patterns near

[100] and 12 patterns near [101] were refined relaxing isotropic DW factors and several low order structure factors simultaneously. The resulting DW factors $B(\text{Fe})_{iso}$, $B(\text{Pd})_{iso}$ and corresponding standard deviations are listed in Table 13. The values for the isotropic DW factors $B(\text{Fe})_{iso}$ and $B(\text{Pd})_{iso}$ should fall in the range limited by the anisotropic DW factors for the respective elements in the L1₀-ordered structure. The values for $B(\text{Fe})_{iso}$ and $B(\text{Pd})_{iso}$ determined from orientations near the [001] zone axis are of high accuracy as can be seen from Table 3. The equivalent DW factors refined from patterns near [110] zone axis are also stable. The isotropic DW factor $B(\text{Fe})_{iso}$ was determined as $0.23(3) \text{ \AA}^2$, which lies in the range of $B(\text{Fe})_{11}=0.30(2) \text{ \AA}^2$ and $B(\text{Fe})_{33}=0.21(3) \text{ \AA}^2$, and $B(\text{Pd})_{iso}$ was determined as $0.25(4) \text{ \AA}^2$, which lies between $B(\text{Pd})_{11}=0.20(2) \text{ \AA}^2$ and $B(\text{Pd})_{33}=0.31(5) \text{ \AA}^2$.

Table 13 Refined isotropic DW factors using patterns along different orientation

Zone axis	<001>		<110>		<100>		<101>	
	$B(\text{Fe})$	$B(\text{Pd})_{iso}$	$B(\text{Fe})_{iso}$	$B(\text{Pd})_{iso}$	$B(\text{Fe})_{iso}$	$B(\text{Pd})_{iso}$	$B(\text{Fe})_{iso}$	$B(\text{Pd})_{iso}$
Value (\AA^2)	0.30	0.20	0.23	0.25	0.22	0.27	0.11	0.36
Standard deviation (\AA^2)	0.02	0.02	0.03	0.04	0.16	0.08	0.16	0.14

DW factors refined from the other two orientations [100] and [101] are not very stable. In the case of near [101] orientation the standard deviation is as high as 160%. Results in Table 13 are visualized in a graph in Figure 38, which plots contour lines of R_w , as the isotropic DW factors $B(\text{Fe})_{iso}$ and $B(\text{Pd})_{iso}$ are varied. In contour maps derived from refinements of CBED

data from near [001] and [110] orientations, unique global minima, surrounded by near-circular contour lines, can be observed. In the contour map from near [101], no global minimum can be observed. Instead two equally good R_w valleys occur, which means, that no unique set of $B(\text{Fe})_{iso}$ and $B(\text{Pd})_{iso}$ can be obtained from near [101] orientations. The refinement of near [101] orientation yields two sets of $B(\text{Fe})_{iso}$ and $B(\text{Pd})_{iso}$, which are equally likely (this was also observed in refinements using anisotropic DW factors). The contour map for near [100] orientation shows irregular contour lines. However, while $B(\text{Pd})_{iso}$ is reasonably well determined for this later orientation, the global minimum extends parallel to the $B(\text{Fe})_{iso}$ axis, which reflects a large uncertainty for values of $B(\text{Fe})_{iso}$. Since the patterns obtained from near [001] and [110] zone axes are more sensitive to changes in DW factors and refinements always result in a global minimum in the contour map, we used these two orientations to obtain anisotropic DW factors.

High order structure factors can be relatively accurately approximated using IAM values. Low order structure factors are strongly affected by bonding effects, which cause significant deviations from IAM approximations. Hence, it might be concluded, that the use of high index zone axis orientations is favorable as low order structure factors can be avoided in the refinement. However, Figure 38 and Table 13 tell us that high index zone axis CBED patterns are not necessarily a good choice since they are not sufficiently sensitive to refine DW factors. To obtain accurate DW factors, near low-index zone axis CBED patterns offer a better choice with improved sensitivity regarding changes in DW factor. We speculate that here the increased number of strongly excited beams and the consequently enhanced dynamic beam interactions are

associated with the improved sensitivity of the near-zone axis patterns regarding DW factor changes.

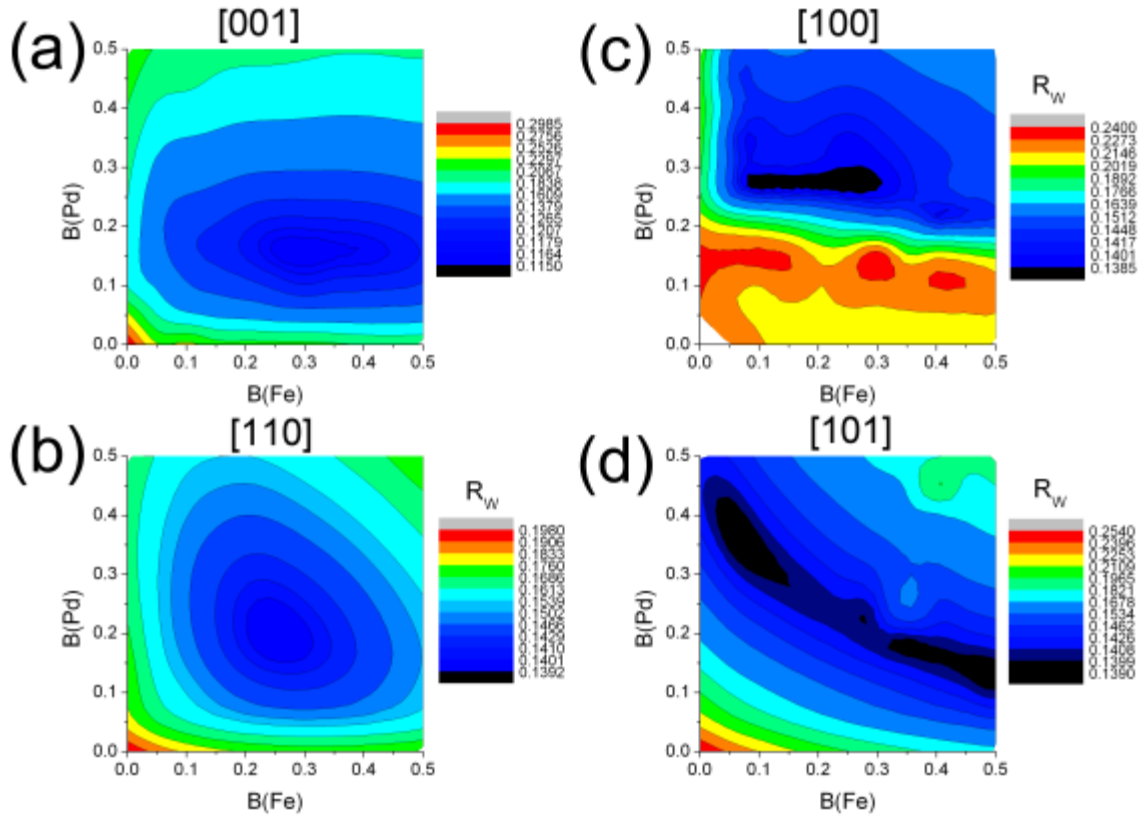


Figure 38 Contour maps of R_w with changing assumed isotropic DW factors along zone axes (a)[001], (b)[110], (c)[100] and (d)[101].

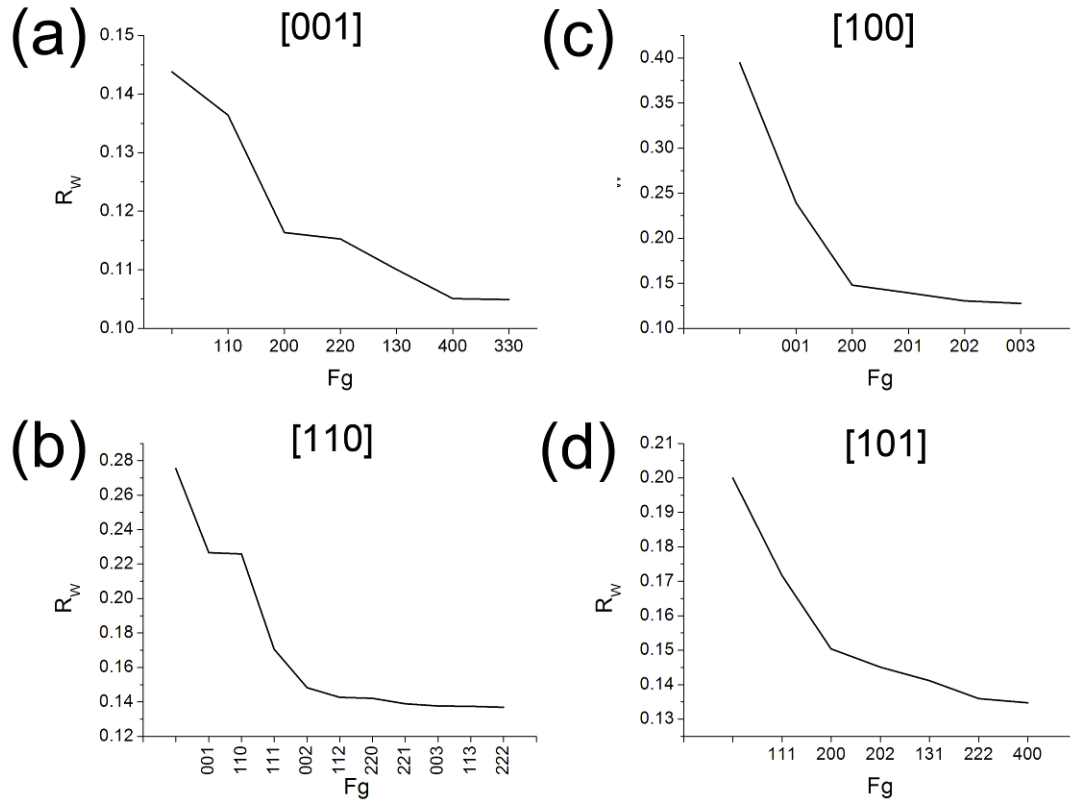


Figure 39 Changes of R_w as increasing numbers of reflections are included and relaxed in the refinement for patterns taken along zone axes (a)[001], (b)[110], (c)[100] and (d)[101].

8.2.2 Sensitivity to structure factors

We refined CBED patterns varying the number of relaxed low order structure factors, to demonstrate the sensitivity of the intensity distribution in an off-zone-axis multi-beam condition pattern with changes in structure factors. As shown in Figure 39 (a), the first value $R_w = 0.144$ was obtained using measured DW factors in 8.1.1 and approximating all the structure factors to IAM values. The next value $R_w = 0.136$ in the plot was obtained using measured DW factors and relaxing only the 110 structure factor. All other structure factors were fixed to the IAM values. Analogously, $R_w = 0.116$ was obtained relaxing 110 and 200 structure factors. Each time

an additional structure factor was included and relaxed in the refinement. As can be seen from Figure 39, R_w values initially decrease dramatically as the first few low order structure factors are relaxed, and finally become constant. R_w values improve as more structure factors are relaxed. Low order structure factors are affected by charge transfer and localization, and therefore deviate significantly from IAM values. Hence refinements that use fixed IAM values naturally yield higher R_w values. As more structure factors with increasing order are relaxed, R_w values decrease monotonously until a minimum is obtained. This can be attributed to the fact that the pattern intensity is not sensitive to the next higher order structure factor or that the IAM approximation sufficiently well describes these higher order structure factors. Intensity distributions in off-zone-axis multi-beam conditions are very sensitive to changes of a few low order structure factors. However, there is a limit after which off-zone-axis multi-beam patterns are not significantly influenced by high order structure factors. Surprisingly, although the patterns are less sensitive to higher order structure factors, the refined results (Figure 37 (a)) show that standard deviations of electron structure factors do not significantly increase from low order to high order structure factors. The high scatter shown in Figure 37 (b) for high order X-ray structure factors is caused by the term s^2 in the Mott formula, as discussed in section Error! Reference source not found..

Figure 39 also shows that this multi-beam method can be very sensitive to slight changes of structure factors, which has been shown for silicon [57] and B2 NiAl [58]. Under exactly the same off-zone-axis multi-beam condition, the change of R_w value due to relaxation of more structure factors along the same zone axis [001] can be reduced from 0.36 to 0.14 for NiAl and from 0.14 to 0.11 for L1₀ FePd, which shows that for FePd low order structure factors deviate

less from IAM values than is the case for NiAl and that FePd has smaller (relative and/or total) amount of charge transfer and localization than NiAl. Thus, the measurements of structure factors for the case of FePd require higher precision than for NiAl in order to become sensitive to effects from interatomic bonding.

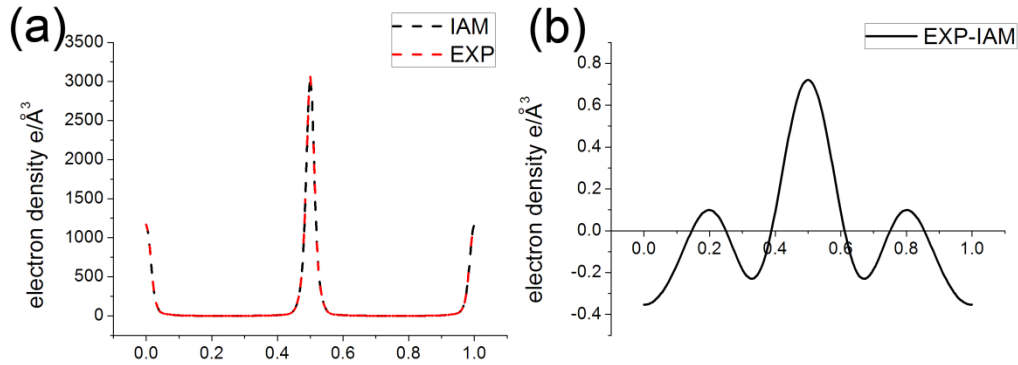


Figure 40 (a) Comparison of the electron density obtained by the IAM model approximation and the experimental CBED measurements along the $\langle 101 \rangle$ orientation in the tp4 unit cell, which is equivalent to the $\langle 111 \rangle$ orientation of the tp2 unit cell; (b) Difference of the electron density from the IAM approximation and the experimentally determined structure factors along the same direction

Figure 40 (a) shows a comparison of the electron density along the $\langle 101 \rangle$ orientation of the tp4 unit cell, which is equivalent to the $\langle 111 \rangle$ orientation of the tp2 unit cell of L1₀ ordered γ_1 – FePd. The IAM electron density was obtained by Fourier transformation of IAM X-ray structure factors satisfying $h^2+k^2+l^2 < 900$, which is sufficient based on a convergence test. For the calculation of the experimental electron density, for low order X-ray structure factors up to 311 measured values were used in the Fourier transformation instead of IAM values. While from Figure 40 (a) virtually no difference between the IAM model approximation and the experimentally determined charge density distribution is discernible, plotting the difference between the IAM approximation and the experimentally determined charge density (Figure 40 (b)) shows some small changes. In both plots of Figure 40, abscissa (X-axis) sales between 0.0

and 1.0, with corresponding positions of the Fe atoms at 0.0 and 1.0 and the position of the Pd atom at 0.5. This indicates that some charge is transferred from the Fe atoms both to the Pd atom and to locations between the Fe and the Pd atom. This result not only shows that our technique is accurate enough to detect changes as small as 0.01% of the total signal, but that our experimentally determined structure and DW factor data is also in principle accurate enough to construct charge difference maps. Why we refrain here from presenting an actual charge difference map will be explained in the next section.

8.2.3 Self - consistency of structure factors refined from different zone axis

Absolute structure factor values have to be the same no matter from which near zone axis orientation they have been obtained. Our structure factor refinements from different near zone axes orientations show good correspondence and are self-consistent data sets, as can be seen from Figure 37. The same structure factor obtained from different orientations is, with exception of the structure factor 220, always consistently larger or smaller than the IAM value. When the 220 reflection is refined from near [001] zone axis, the X-ray structure factor is larger than the IAM value. Refinement from near [110] zone axis orientation yields a 220 X-ray structure factor smaller than the IAM value.

This inconsistency is possibly caused by the insensitivity of those two orientations to changes of the 220 reflection. As can be seen in Figure 39 (a, b), the relaxation of the 220 reflection results in only very minor decrease of the respective R_w value. The other possible reason might be that the zero background assumption might not be applicable here [154]. An alternative background correction method is under investigation ([154]). A third reason could be

related to the ferromagnetic nature of $L1_0$ FePd with its high symmetry and unique easy magnetization c – axis. The interaction between the incident electrons and magnetic field within the crystal is different for different zone axes. For the non-magnetic, iso-structural intermetallic phase $L1_0$ TiAl, structure factors obtained with the off-axis CBED method from different zone axes agree very well (unpublished data). We probed the hypothesis that the ferromagnetic may have effects on the structure factor determination by CBED for $L1_0$ -FePd by comparing electron structure factors $U_g(110)$ and $U_g(200)$ obtained from different zone axes.

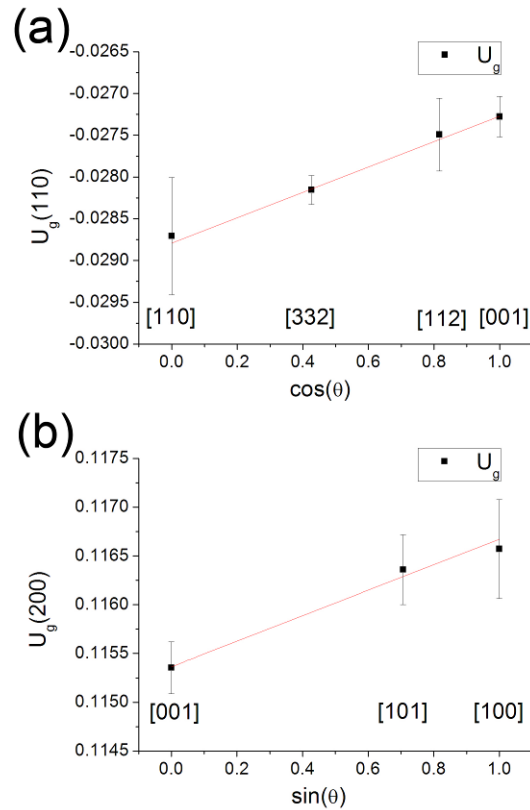


Figure 41 Dependence of the electron structure factors (a) $U_g(110)$ on the $\cos(\theta)$ and (b) $U_g(200)$ $\sin(\theta)$, where θ is the angle between the zone axis orientation, $[uvw]$, used for CBED from which the structure factor was refined and the easy magnetization axis $[001]$ of the $L1_0$ -FePd phase.

Aside from the data presented above in Table 11 and Table 12, we obtained additional structure factor measurements using off-zone axis multi-beam conditions near two other zone

axes, namely [112] and [332]. Data for the two electron structure factors $U_g(110)$ and $U_g(200)$ from different zone axes were compiled in Figure 41, where the x-axis is the sine or cosine of the angle θ , the misorientation angle between the zone axis orientation of the sample for which the electron structure factor was obtained by the off-zone axis multi-beam CBED method and the easy magnetization axis [001] of the $L1_0$ —FePd phase. Both structure factors exhibit linear relationships with respect to the respective trigonometric function of the angle between the incident electron beam, [uvw], and the easy magnetization axis, [001]. We speculate this systematic change of refined structure factor is related to the angular dependence of the interaction of the magnetic field of $L1_0$ ordered FePd and the incident fast electrons used for CBED. The conventional Bloch wave formalism does not include magnetic field terms [151]. The treatment of Bloch electrons in a uniform magnetic field has been investigated before by [194-196]. [197] reported that only the magnetic fields parallel to the incident beam would not influence the intensity of CBED patterns. Therefore, only structure factors from near [001] zone axis (i.e. U_{110} , U_{200} , U_{220} , U_{130} and U_{400}) are not influenced by the magnetic field and do not have to be corrected. All structure factors (U_{001} , U_{111} , U_{002} , U_{201} , U_{202} , U_{311} , U_{222} , etc.), which cannot be determined from [001] zone axis, have to be obtained from other near zone axis orientations and need to be corrected. Currently the adaption of interaction between fast electron and magnetic field in Bloch wave formalism is not readily available. Reasonable electron charge density maps cannot be constructed without inclusion of the structure factors that cannot be obtained from the near [001] zone axes orientation, i.e., without U_{hkl} with $l \neq 0$. Therefore, we do not present a charge density map here. Further investigation on how to correct those structure factors and construction of charge density map is in progress.

8.2.4 Comparison with DFT results

DFT simulations for $L1_0$ FePd were performed using WIEN2K software as described in 3.6.1. As the theoretical structure factors are static structure factors, all the experimental structure factors in Table 14 were converted to static structure factor by removing the influence of DW factors. It can be seen that the structure factors of the two superlattice reflections $F_g(001)$ and $F_g(110)$ are different within the error bar from the LDA and GGA simulations. The structure factors of the main reflections $F_g(111)$, $F_g(200)$ and $F_g(002)$ agree very well with both GGA and LDA theoretical structure factors. For structure factors beyond 201, due to larger error introduced from QCBED measurement and conversion from Mott formula, it is hard to tell whether the disagreement between experimental structure factors and theoretical structure factors reflect the true trend or not.

The disagreement between experimental and theoretical structure factors $F_g(001)$ and $F_g(110)$ shows that the interlayer Fe-Pd (3d-4d) interaction (corresponding to $F_g(001)$) and Fe-Fe (3d-3d) and Pd-Pd (4d-4d) nearest neighbor interactions (corresponding to $F_g(110)$) are not fully considered by current DFT approximations. Investigation on the origin of this disagreement is in progress.

Table 14 Experimental and theoretical structure factors for L1₀ FePd

hkl	[110]	[101]	[100]	[001]	IAM	LDA PW	GGA PBE
001	-18.57(4)		-18.60(2)		-18.88	-18.37	-18.39
110	-17.50(6)			-17.62(2)	-17.68	-17.28	-17.31
111	54.21(7)	54.32(4)			54.70	54.20	54.26
200		51.37(6)	51.33(9)	51.55(5)	51.76	51.29	51.36
002	50.46(8)		50.55(14)		50.92	50.55	50.62
201			-15.3(2)		-14.93	-14.91	-14.93
112	-14.36(17)				-14.27	-14.28	-14.28
220	42.64(31)			43.27(18)	43.04	42.99	43.06
202		43.01(19)			42.56	42.57	42.64
221	-13.87(31)				-13.24	-13.33	-13.33
003	-13.49(30)				-13.08	-13.19	-13.18
130				-13.68(30)	-12.99	-13.14	-13.14
131		39.16(13)			38.78	38.83	38.89
113	38.16(27)				38.12	38.23	38.27
222	37.88(34)	38.12(24)			37.44	37.54	37.59

8.3 CONCLUSION

Highly accurate structure factors and anisotropic DW factors for L1₀ ordered FePd were simultaneously measured using a multi-beam off-zone axis CBED method. $B(\text{Fe})_{11}$, $B(\text{Fe})_{33}$, $B(\text{Pd})_{11}$ and $B(\text{Pd})_{33}$ are $0.30(2)\text{\AA}^2$, $0.21(3)\text{\AA}^2$, $0.20(2)\text{\AA}^2$ and $0.31(5)\text{\AA}^2$, respectively. Low order electron diffraction and X-ray diffraction structure factors up to 222 were measured. Several low-order structure factors have accuracy higher than 0.1%. Additionally, we detected an influence of the magnetic field of the L1₀ ordered γ_1 – FePd on the intensity distribution in

CBED patterns. Depending on the orientation of the magnetic field of the investigated sample area with the incident beam the influence on the intensity distribution and the ensuing change in structure factor can be more or less severe. At this moment there is no appropriate treatment of the interaction of magnetic fields with fast electrons in the Bloch wave formalism used in refinements for structure factor determination. The disagreement between theoretical and experimental $F_g(001)$ and $F_g(110)$ hints that more reliable DFT approximations are necessary for the treatment of 3d-3d, 3d-4d, 4d-4d interactions in $L1_0$ FePd.

9.0 PRELIMINARY RESULTS OF L1₀ FEPT

As the main objective of this study the accurate measurement of the electron density of L1₀ FePd and FePt had been identified. It had been hypothesized that this could be accomplished by advancing currently available experimental methods of QCBED for simultaneous measurement of multiple structure factors and Debye-Waller factors. Further, it was envisaged that this would support development of more reliable DFT approximations to explain materials properties of L1₀ FePd and FePt based on electron density. Highly accurate and precise structure factors for L1₀ FePd have been measured using the off-zone axis multi-beam QCBED method that has been developed and optimized through this study. Hence, in principle, the measurement should be easily extended to L1₀ FePt using the same QCBED method that has worked so convincingly for TiAl and FePd. However, the attempts to prepare TEM transparent sections, specimens suitable for QCBED application from bulk L1₀ FePt, have proven unsuccessful to date. In the absence of suitable TEM foil section in samples prepared from the bulk FePt it is impossible to apply the new QCBED method to determine experimentally structure and DW factors for FePt.

Two main sample preparation methods, electrolytic twin-jet-polishing and Ar-ion-milling, have been applied in attempts to obtain artifact-free and surface-defect-free TEM-transparent L1₀ FePt TEM samples. The electrolytic-polishing method, which allows gently and uniformly non-destructive removal of the sample disc material without introduction of mechanical stresses until a hole forms in the center of the disc, is the method of choice for

QCBED, where the integrity of the crystal lattice is essential for accurate quantitative analysis of diffraction intensities. Many different solutions and polishing conditions have been selected to electrolytically jet-polish $L1_0$ FePt. However, according to our experiments, most solutions that react with common metals and intermetallics do not react with $L1_0$ FePt due to its high corrosion resistance. Searching for new solutions combined with appropriate polishing condition is ongoing.

The ion-milling method has also been used to prepare TEM samples for $L1_0$ FePt. In ion-milling experiments, one or two ion guns shoot an argon ion-beam with energy of several kV on the sample at an incident angle ranging from several to twenty degrees. The argon ion-beam knocks away constituent atoms from the sample surface by breaking the bonding between atoms, and at the same time, the argon ion-beam introduces damages such as re-deposition of materials, surface defects and point defects in the sample. These damages compromise periodicity of the crystal lattice of the intermetallic phase and influence the diffraction intensity distribution that is used for quantitative analysis. The ion-beam induced damage to the crystal lattice renders it unfavorable for QCBED work, especially for intermetallic systems where the metallic bonding between metallic atoms is not as strong as the bonding in covalent systems. Therefore intermetallic systems, such as FePt, appear to be more susceptible to ion-beam damage effects than Si for instance. In order to minimize the argon beam damage on the sample, a Fischione Model 1050 NanoMill system that is capable of lowering the argon beam voltage down to 0.2kV was used, compared with other ion-mills generally operating around 3-5kV and generating much higher energy argon ion-beam.

An $L1_0$ FePt TEM sample was prepared using Fischione Model 1050 Nanomill with following steps:

Step 1: 4.5kV /+/- 10deg./Sample rotation with beam sequencing/4 hrs.(=perforation)

Step 2: 3.0kV /+/- 9deg. /Sample rotation with beam sequencing/50 min.

Step 3: 1.0kV /+/- 9deg. /Sample rotation with beam sequencing/30 min.

Step 4: ending with 0.2kV.

A bright field image taken from a thin area of the ion-milled sample is shown in Figure 42 where contrast features that are related to ion-beam damage are clearly observed. Using appropriate imaging conditions, diffraction contrast images reveal these damage related features for all of the investigated sample areas. These surface relief or line-like defect features render the sample areas unsuitable for the QCBED experiments. For example, an off-zone axis multi-beam CBED pattern was acquired from a dislocation-free area of the ion-milled sample close to [001] orientation (Figure 43). According to symmetry analysis of QCBED patterns [155], two mirror planes (marked in red lines) should be observed for features in 200 and 020 discs respectively. Although the main contours in 200 and 020 discs meet the symmetry requirement, finer details and intensity distribution clearly show a symmetry break, which indicates that the influence on intensity distribution of CBED pattern from the ion-beam induced defects cannot be neglected. Therefore, even with the most advanced ion-milling technique, the beam damage cannot be reduced to a level that quantitative work is possible.

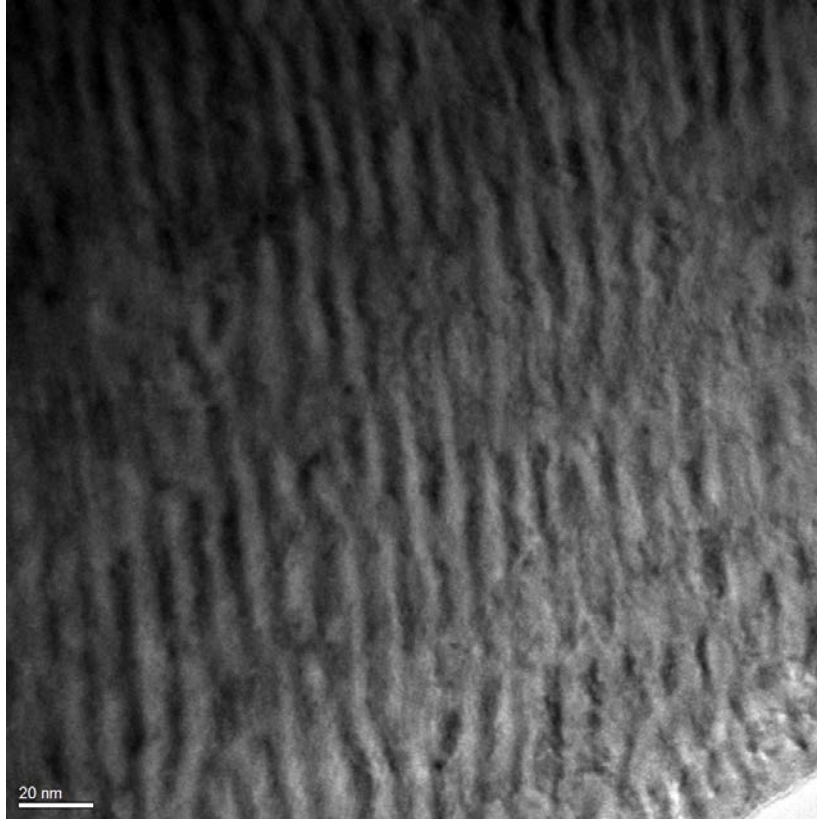


Figure 42 a bright field image of the ion-milled FePt sample

In the future, to prepare TEM samples that are suitable for high quality QCBED work, we are planning to use several other techniques. For example, in order to minimize surface re-deposition during ion-milling, it is proposed to first fabricate an $L1_0$ FePt slab with a thickness of approximately 300nm from a bulk sample using focused ion beam (FIB) and then to nano-mill the slab to remove the Ga ion-beam introduced damage layer in FIB process. By doing this, the ion-milling time is greatly reduced and the interaction area between ion-beam and the sample is also greatly reduced, which might result in a sample that is suitable for QCBED.

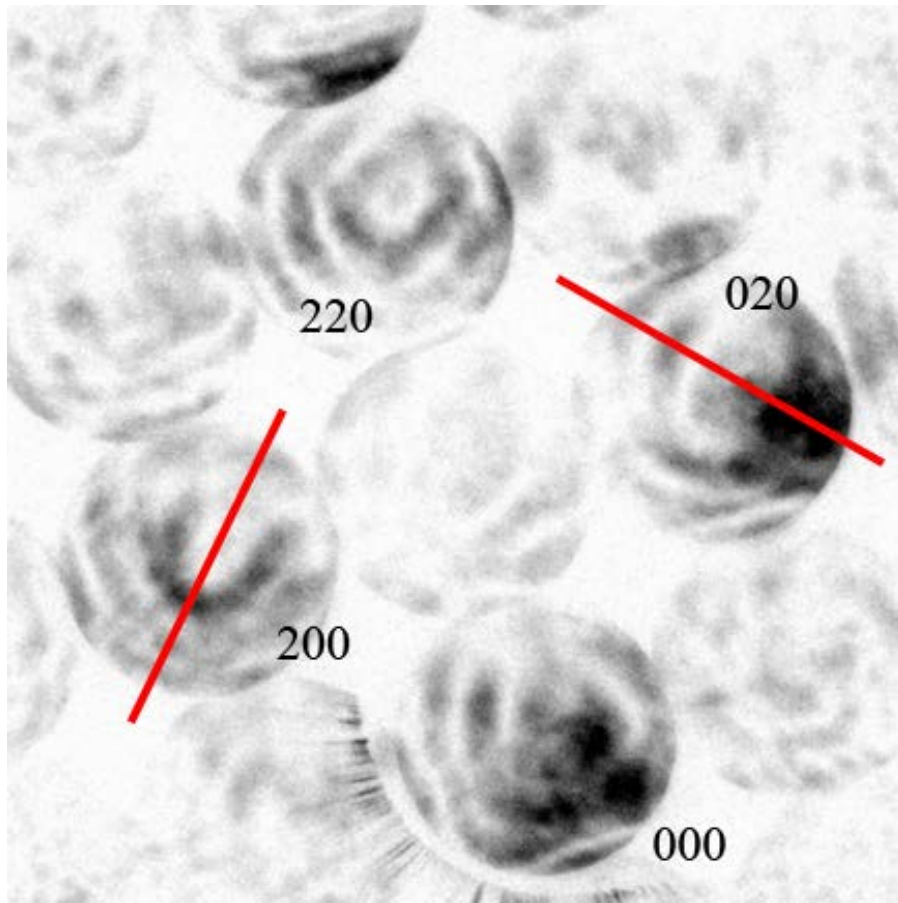


Figure 43 off zone axis multi-beam CBED pattern showing symmetry break.

Another way of preparing TEM-transparent and artificial-defect free sample is to make thin films using various deposition methods. By carefully adjusting deposition parameters, it is possible to deposit FePt thin film with a thickness sufficient for dynamical effect to dominate in QCBED, on a substrate that can be removed by dissolving in water after deposition.

If the suitable FePt TEM sample could be prepared using techniques mentioned above, accurate structure factors and DW factors will be measured using the same off-zone axis multi-beam QCBED method that has been applied successfully to $L1_0$ TiAl and $L1_0$ FePd. The electron density map of $L1_0$ FePt will also be constructed to compare with that of $L1_0$ FePd to broaden our understanding of 3d-4d and 3d-5d electron interaction and bonding information.

10.0 SUMMARY

10.1 RESULTS

In this study, the new multi-beam off-zone axis QCBED method that allows simultaneous measurement of DW and structure factors to unprecedented high accuracy and precision has been established using benchmarking materials Si, B2 NiAl and L1₀ TiAl. For the first time, excellent internal and external consistency was achieved for the DW and structure factors refined from CBED patterns acquired from different orientations and a large range of sample thicknesses. Unlike previous methods that entail measurement of DW factors using XRD with a different sample, using the new method, accurate DW and structure factors, measured solely using the TEM, are refined based on information from the same sample volume, which minimizes inconsistency stemming from using different samples for the measurements, and greatly increases the reliability of the QCBED results. Additionally, the refinement method for the new multi-beam off-zone axis method has been greatly simplified compared with previous methods, e.g. regarding background subtraction, point spread function correction or distortion correction, which are not essential in our method because of the high sensitivity of the method to the change of DW and structure factors.

In the new multi-beam off-zone axis method, the sample is tilted such that several low order diffraction discs are simultaneously excited. The dynamical interaction of several strongly

excited beams renders the resulting CBED pattern highly sensitive to change of structure factors. Using the Bloch wave theory of electron interacting with periodic potential, we proved that the new QCBED method is more sensitive to bonding information (change of structure factors) than the other experimental QCBED methods used previously, because more anti-bound Bloch wave branches that interact with bonding electrons are excited. The high accuracy enables direct evaluation of the validity of different approximations used in DFT calculations of the electron density for transition metal based intermetallics.

Complete sets of DW and structure factors for tetragonal binary intermetallics $L1_0$ TiAl and FePd have been measured using the new QCBED method. The electron density difference map constructed from accurate experimental DW and structure factors for $L1_0$ TiAl was compared with theoretical electron density difference map using DFT-based ab-initio calculations with different approximations. The experimental data qualitatively agrees with theoretical data, but quantitatively, both GGA and LDA approximations overestimate electron delocalization around Ti atoms, which suggests that the currently available DFT methods are not sufficiently accurate for electron interaction involving d-level electrons. Comparison between experimental and theoretical structure factors for $L1_0$ FePd further confirmed that the Fe-Fe (3d-3d), Fe-Pd (3d-4d) and Pd-Pd (4d-4d) electrons interaction could not be described by current DFT methods with sufficient accuracy. Therefore, highly accurate experimental data from QCBED indicates the necessity of developing a DFT approximation that better describes electron interactions involving d- and f- electrons, e. g., most intermetallic systems.

10.2 FUTURE WORK

10.2.1 Measurements of DW and structure factors for L1₀ FePt

The measurements of DW factors and structure factors for L1₀ FePt will be attempted in the near future as sample preparation difficulties are being addressed. As discussed in Chapter 1.0 , the fraction (0.5%) of transferred charge in L1₀ FePt is even smaller than that in L1₀ FePd (0.7%). Therefore, even higher accuracy is required in QCBED experiments to determine electronic structure of L1₀ FePt. Based on the accomplishments to date for Si, B2 NiAl, L1₀ TiAl and FePd, it can be reasonably expected that the multi-beam off-zone axis QCBED method will work for L1₀ FePt once suitable L1₀ FePt samples have become available.

10.2.2 Theoretical work on L1₀ FePd and FePt

After experimental and theoretical data for both L1₀ FePd and L1₀ FePt are obtained, relationship between the different properties of L1₀ FePd and L1₀ FePt and the different electronic structures of L1₀ FePd and L1₀ FePt can be investigated comprehensively. As mentioned in section 10.1, the current-established approximations used in DFT methods have problems dealing with d- and f- electron related bonding interactions. Establishment of a better DFT approximation is essential to better explain interactions in complex magnetic intermetallics, broadening the fundamental understanding on intermetallics that are based on heavier (larger atomic number) metal atoms.

BIBLIOGRAPHY

- [1] R.M. Martin, *Electronic structure, Basic theory and practical methods*, Cambridge university press, 2004.
- [2] E. Kabliman, P. Blaha, K. Schwarz, *Physical Review B* 82 125308.
- [3] S. Ghosh, *Intermetallics* 17 (2009) 708-713.
- [4] V. Murg, F. Verstraete, Legeza, Ouml, R.M. Noack, *Physical Review B* 82 205105.
- [5] H. Hsu, P. Blaha, R.M. Wentzcovitch, C. Leighton, *Physical Review B* 82 100406.
- [6] N. Narayanan, D. Mikhailova, A. Senyshyn, D.M. Trots, R. Laskowski, P. Blaha, K. Schwarz, H. Fuess, H. Ehrenberg, *Physical Review B* 82 024403.
- [7] Y.-S. Kim, M. Marsman, G. Kresse, F. Tran, P. Blaha, *Physical Review B* 82 205212.
- [8] K. Schwarz, P. Blaha, S.B. Trickey, *Molecular Physics: An International Journal at the Interface Between Chemistry and Physics* 108 3147 - 3166.
- [9] L. Kalarasse, B. Bennecer, F. Kalarasse, S. Djeroud, *Journal of Physics and Chemistry of Solids* 71 1732-1741.
- [10] R.O. Jones, O. Gunnarsson, *Reviews of Modern Physics* 61 (1989) 689.
- [11] W. Kohn, L.J. Sham, *Physical Review* 140 (1965) A1133.
- [12] P. Hohenberg, W. Kohn, *Physical Review* 136 (1964) B864.
- [13] J.M. Zuo, P. Blaha, K. Schwarz, *Journal of Physics-Condensed Matter* 9 (1997) 7541-7561.
- [14] Z.W. Lu, S.H. Wei, A. Zunger, *Acta Metallurgica Et Materialia* 40 (1992) 2155-2165.
- [15] S.L. Dudarev, L.M. Peng, S.Y. Savrasov, J.M. Zuo, *Physical Review B* 61 (2000) 2506.
- [16] M.P. Fernandez-Liencre, A. Navarro, J.J. Lopez-Gonzalez, M. Fernandez-Gomez, J. Tomkinson, G.J. Kearley, *Chemical Physics* 266 (2001) 1-17.
- [17] E.I. Isaev, A.I. Lichtenstein, Y.K. Vekilov, E.A. Smirnova, I.A. Abrikosov, S.I. Simak, R. Ahuja, B. Johansson, *Solid State Communications* 129 (2004) 809-814.

- [18] S. Grimme, Accurate description of van der Waals complexes by density functional theory including empirical corrections, in: vol 25, John Wiley & Sons, Inc., 2004, pp. 1463-1473.
- [19] S. Grimme, *The Journal of Chemical Physics* 124 (2006) 034108.
- [20] U. Zimmerli, M. Parrinello, P. Koumoutsakos, *The Journal of Chemical Physics* 120 (2004) 2693-2699.
- [21] O.A. von Lilienfeld, I. Tavernelli, U. Rothlisberger, D. Sebastiani, *Physical Review Letters* 93 (2004) 153004.
- [22] T.J. Klemmer, N. Shukla, C. Liu, X.W. Wu, E.B. Svedberg, O. Mryasov, R.W. Chantrell, D. Weller, M. Tanase, D.E. Laughlin, *Applied Physics Letters* 81 (2002) 2220-2222.
- [23] S. Sun, C.B. Murray, D. Weller, L. Folks, A. Moser, *Science* 287 (2000) 1989-1992.
- [24] J. Lyubina, O. Gutfleisch, O. Isnard, *Journal of Applied Physics* 105 (2009) 07A717.
- [25] M.A. Spackman, *Chemical Reviews* 92 (1992) 1769-1797.
- [26] J.M. Zuo, *Reports on Progress in Physics* 67 (2004) 2053-2103.
- [27] J. Friis, B. Jiang, J. Spence, K. Marthinsen, R. Holmestad, *Acta Crystallographica Section A* A60 (2004) 402-408.
- [28] J.M. Zuo, M. Kim, M. O'Keeffe, J.C.H. Spence, *Nature* 401 (1999) 49-52.
- [29] Y. Ogata, K. Tsuda, Y. Akishige, M. Tanaka, *Acta Crystallographica Section A* A60 (2004) 525-531.
- [30] B. Jiang, J.M. Zuo, N. Jiang, M. O'Keeffe, J.C.H. Spence, *Acta Crystallographica Section A* A59 (2003) 341-350.
- [31] V.A. Streltsov, P.N.H. Nakashima, A.W.S. Johnson, *Journal of Physics and Chemistry of Solids* 62 (2001) 2109-2117.
- [32] J.M. Zuo, M. O'Keeffe, P. Rez, J.C.H. Spence, *Physical Review Letters* 78 (1997) 4777-4780.
- [33] M. Saunders, D.M. Bird, N.J. Zaluzec, W.G. Burgess, A.R. Preston, C.J. Humphreys, *Ultramicroscopy* 60 (1995) 311-323.
- [34] Y. Ogata, K. Tsuda, M. Tanaka, *Acta Crystallographica Section A* A64 (2008) 587-597.
- [35] J. Friis, G.K.H. Madsen, F.K. Larsen, B. Jiang, K. Marthinsen, R. Holmestad, *The Journal of Chemical Physics* 119 (2003) 11359-11366.
- [36] P.N.H. Nakashima, A.E. Smith, J. Etheridge, B.C. Muddle, *Science* 331 (2011) 1583.
- [37] R. Holmestad, C.R. Birkeland, *Philosophical Magazine A* 77 (1998) 1231 - 1254.
- [38] R. Holmestad, J.M. Zuo, J.C.H. Spence, R. Hoier, Z. Horita, *philosophical Magazine A* 72 (1995) 579-601.

- [39] C.L. Fu, M.H. Yoo, *Intermetallics* 1 (1993) 59-63.
- [40] C.L. Fu, M.H. Yoo, *Philosophical Magazine Letters* 62 (1990) 159-165.
- [41] H. Fu, Z. Zhao, W. Liu, F. Peng, T. Gao, X. Cheng, *Intermetallics* 18 (2010) 761-766.
- [42] T. Klemmer, D. Hoydick, H. Okumura, B. Zhang, W.A. Soffa, *Scripta Metallurgica Et Materialia* 33 (1995) 1793-1805.
- [43] T.B. Massalski, H. Okamoto, *Binary Alloy Phase Diagrams* [CD-ROM], 2nd ed, ASM International, Materials Park, OH, 1996.
- [44] P.P. Ewald (Ed.) *Fifty years of X-ray diffraction*, International Union of Crystallography, Glasgow, Scotland, 1962, p.
- [45] G. Boebel, P. Cortona, F.G. Fumi, *Acta Crystallographica Section A* A45 (1989) 112-115.
- [46] P.J.E. Aldred, M. Hart, *Proceedings of the Royal Society of London. Series A, Mathematical and Physical Sciences (1934-1990)* (1973).
- [47] P.J.E. Aldred, M. Hart, *Proceedings of the Royal Society of London. Series A, Mathematical and Physical Sciences (1934-1990)* 332 (1973) 223-238.
- [48] R. Teworte, U. Bonse, *Physical Review B* 29 (1984) 2102.
- [49] J.C.H. Spence, J.M. Zuo, *Electron Microdiffraction*, Plenum Press, New York, 1992.
- [50] B. Jiang, J. Friis, R. Holmestad, J.M. Zuo, M. O'Keeffe, J.C.H. Spence, *Physical Review B* 69 (2004) 245110.
- [51] J. Friis, B. Jiang, K. Marthinsen, R. Holmestad, *Acta Crystallographica Section A* A61 (2005) 223-230.
- [52] W. Nüchter, A.L. Weickenmeier, J. Mayer, *physica Status Solidi a-Applications and Materials Science* 166 (1998) 367-379.
- [53] J. Zhu, Y. Miao, J.T. Guo, *Acta Materialia* 45 (1997) 1989-1994.
- [54] W. Nüchter, A.L. Weickenmeier, J. Mayer, *acta Crystallographica Section A* A54 (1998) 147-157.
- [55] M.Y. Wu, S.Y. Li, Z.H. Du, S.L. Li, *Acta Crystallographica Section A* A56 (2000) 189-192.
- [56] X. Sang, A. Kulovits, J.M.K. Wiezorek, *Microscopy and Microanalysis* 16(Suppl. 2) (2010) 938-939.
- [57] X.H. Sang, A. Kulovits, J.M.K. Wiezorek, *Acta Crystallographica Section A* A66 (2010) 685-693.
- [58] X.H. Sang, A. Kulovits, J.M.K. Wiezorek, *Acta Crystallographica Section A* A66 (2010) 694-702.
- [59] E.S.K. Menon, A.G. Fox, *Acta Materialia* 44 (1996) 2547-2555.
- [60] P. Gumbsch, M.W. Finnis, *Philosophical Magazine Letters* 73 (1996) 137 - 144.

- [61] A.G. Fox, M.A. Tabbernor, *Acta Metallurgica Et Materialia* 39 (1991) 669-678.
- [62] T. Ichitsubo, K. Tanaka, *Journal of Applied Physics* 96 (2004) 6220-6223.
- [63] S. Yuasa, H. Miyajima, Y. Otani, *Journal of the Physical Society of Japan* 63 3129.
- [64] K.H.J. Buschow, P.G. van Engen, R. Jongebreur, *Journal of Magnetism and Magnetic Materials* 38 (1983) 1-22.
- [65] A. Menshikov, T. Tarnóczy, E. Krén, *Physica Status Solidi (a)* 28 (1975) K85-K87.
- [66] A.Z. Menshikov, V.P. Antropov, G.P. Gasnikova, Y.A. Dorofeyev, V.A. Kazantsev, *Journal of Magnetism and Magnetic Materials* 65 (1987) 159-166.
- [67] F. Froes, C. Suryanarayana, D. Eliezer, *Journal of Materials Science* 27 (1992) 5113-5140.
- [68] T. Kawabata, T. Kanai, O. Izumi, *Acta Metallurgica* 33 (1985) 1355-1366.
- [69] L.G. Zhou, L. Dong, L.L. He, C.B. Zhang, *Intermetallics* 8 (2000) 637-641.
- [70] H. Clemens, H. Kestler, *Advanced Engineering Materials* 2 (2000) 551-570.
- [71] Y.W. Kim, *Acta Metallurgica Et Materialia* 40 (1992) 1121-1134.
- [72] Y.W. Kim, D.M. Dimiduk, *Jom-Journal of the Minerals Metals & Materials Society* 43 (1991) 40-47.
- [73] M. Yamaguchi, H. Inui, K. Ito, *Acta Materialia* 48 (2000) 307-322.
- [74] X. Wu, *Intermetallics* 14 (2006) 1114-1122.
- [75] R.M. Imayev, V.M. Imayev, M. Oehring, F. Appel, *Intermetallics* 15 (2007) 451-460.
- [76] J.M.K. Wiezorek, X.-D. Zhang, W.A.T. Clark, H.L. Fraser, *Philosophical Magazine A* 78 (1998) 217-238.
- [77] J.M.K. Wiezorek, X.D. Zhang, A. Godfrey, D. Hu, M.H. Loretto, H.L. Fraser, *Scripta Materialia* 38 (1998) 811-817.
- [78] J. Wiezorek, A. Kulovits, X.-D. Zhang, H. Fraser, *Metallurgical and Materials Transactions A* 42 (2011) 605-612.
- [79] A. Gupta, J.M.K. Wiezorek, *Intermetallics* 11 (2003) 589-600.
- [80] M.H. Loretto, Z. Wu, M.Q. Chu, H. Saage, D. Hu, M.M. Attallah, *Intermetallics* 23 (2012) 1-11.
- [81] R. Sot, K.J. Kurzlowski, *Materials Science- Poland* 23 (2005) 587-590.
- [82] Y.L. Liu, L.M. Liu, S.Q. Wang, H.Q. Ye, *Intermetallics* 15 (2007) 428-435.
- [83] S.R. Chubb, D.A. Papaconstantopoulos, B.M. Klein, *Physical Review B* 38 (1988) 12120.
- [84] M. Morinaga, J. Saito, N. Yukawa, H. Adachi, *Acta Metallurgica Et Materialia* 38 (1990) 25-29.

- [85] Y.Q. Xie, X.B. Liu, K. Peng, H.J. Peng, *Physica B: Condensed Matter* 353 (2004) 15-33.
- [86] A. Hussain, S.S. Hayat, M.A. Choudhry, *Physica B-Condensed Matter* 406 (2011) 1961-1965.
- [87] S.F. Matar, J. Etourneau, *Journal of Alloys and Compounds* 233 (1996) 112-120.
- [88] Y. Liu, H. Li, S. Wang, H. Ye, *Journal of Materials Research* 24 (2009) 3165-3173.
- [89] Y. Koizumi, M. Yoshiya, A. Sugihara, Y. Minamino, *Philosophical Magazine* 91 (2011) 3685-3704.
- [90] M. Asta, D. de Fontaine, M. van Schilfgaarde, *Journal of Materials Research* 8 (1993) 2554-2568.
- [91] W. Wolf, R. Podloucky, P. Rogl, H. Erschbaumer, *Intermetallics* 4 (1996) 201-209.
- [92] Y. Zhao, D.G. Truhlar, *The Journal of Chemical Physics* 125 (2006) 194101-194118.
- [93] A. Al-Ghaferi, P. Muellner, H. Heinrich, G. Kostorz, J.M.K. Wiezorek, *Acta Materialia* 54 (2006) 881-889.
- [94] J.M.K. Wiezorek, C.J. Humphreys, *Scripta Metallurgica Et Materialia* 33 (1995) 451-458.
- [95] N.M. Butt, J. Bashir, B.T.M. Willis, G. Heger, *Acta Crystallographica Section A* A44 (1988) 396-398.
- [96] N.M. Butt, J. Bashir, M.N. Khan, *Acta Crystallographica Section A* A49 (1993) 171.
- [97] P. Georgopoulos, J.B. Cohen, *Scripta Metallurgica* 11 (1977) 147-150.
- [98] P.A. Doyle, P. Turner, *Acta Crystallographica Section A* A24 (1968) 390-397.
- [99] K. Tsuda, M. Tanaka, *Acta Crystallographica Section A* A55 (1999) 939-954.
- [100] B.D. Cullity, S.R. Stock, *Elements of X-ray Diffraction*, Prentice Hall, 2001.
- [101] N. kato, A.R. Lang, *Acta Crystallographica Section A* (1959).
- [102] P.B. Hirsch, *electron microscopy of thin crystals*, Krieger Pub Co, 1977.
- [103] T. Saka, N. Kato, *Acta Crystallographica Section A* (1986).
- [104] N. Kato, *Acta Crystallographica Section A* (1969).
- [105] J. Jansen, D. Tang, H.W. Zandbergen, H. Schenk, *Acta Crystallographica Section A* A54 (1998) 91-101.
- [106] J.W. Steeds, *Ultramicroscopy* 26 (1988) 1-12.
- [107] J. Spence, *Acta Crystallographica Section A* A49 (1993) 231-260.
- [108] J.R. Sellar, D. Imeson, C.J. Humphreys, *Acta Crystallographica Section A* 36 (1980) 686-696.
- [109] J.R. Sellar, D. Imeson, *Acta Crystallographica Section A* 44 (1988) 768-772.

- [110] H. Matsuhata, J. Gjonnes, J. Tafto, *Acta Crystallographica Section A* 50 (1994) 115-123.
- [111] H. Matsuhata, J. Gjonnes, *Acta Crystallographica Section A* 52 (1996) 686-699.
- [112] H. Matsuhata, J. Gjonnes, *Acta Crystallographica Section A* 50 (1994) 107-115.
- [113] H. Matsuhata, J. Gjonnes, *Acta Crystallographica Section A* 51 (1995) 589.
- [114] B. Jiang, J.M. Zuo, Q. Chen, J.C.H. Spence, *Acta Crystallographica Section A* A58 (2002) 4-11.
- [115] P. Goodman, L. Liu, *Acta Crystallographica Section A* A55 (1999) 246-257.
- [116] M. David, R. Serneels, R. Gevers, *Acta Crystallographica Section A* 32 (1976) 1010-1011.
- [117] M. David, R. Gevers, H. Stumpp, *Acta Crystallographica Section A* 41 (1985) 204-206.
- [118] B.F. Buxton, J.E. Loveluck, *Journal of Physics C: Solid State Physics* 10 (1977) 3941.
- [119] B.F. Buxton, M.V. Berry, *Philosophical Transactions of the Royal Society of London. Series A, Mathematical and Physical Sciences* 282 (1976) 485-525.
- [120] J.M. Zuo, R. Hoier, J.C.H. Spence, *Acta Crystallographica Section A* A45 (1989) 839-851.
- [121] H. Zou, X. Yao, R. Wang, *Acta Crystallographica Section A* 47 (1991) 490-497.
- [122] F. Yu, H. Zou, J. Wang, R. Wang, *Micron* 35 (2004) 411-418.
- [123] M.-Y. Wu, J. Zhu, S.-Y. Li, Z.-H. Du, S.-L. Li, *Journal of Applied Crystallography* 33 (2000) 1119-1121.
- [124] K. Tsuda, M. Tanaka, *Acta Crystallographica Section A* (1999).
- [125] K. Tsuda, M. Tanaka, *Acta Crystallographica Section A* A51 (1995) 7-19.
- [126] M. Terauchi, M. Takahashi, M. Tanaka, *Acta Crystallographica Section A* A50 (1994) 566-574.
- [127] M. Saunders, P. Midgley, R. Vincent, J. Steeds, *Journal of Electron Microscopy* 45 (1996) 11-18.
- [128] M. Saunders, A.G. Fox, P.A. Midgley, *Acta Crystallographica Section A* A55 (1999) 480-488.
- [129] M. Saunders, A.G. Fox, P.A. Midgley, *Acta Crystallographica Section A* A55 (1999) 471-479.
- [130] M. Saunders, *Microscopy and Microanalysis* 9 (2003) 411-418.
- [131] G. Ren, J.M. Zuo, L.M. Peng, *Micron* 28 (1997) 459-467.
- [132] P.N.H. Nakashima, B.C. Muddle, *Journal of Applied Crystallography* 43 (2010) 280-284.
- [133] P. Nakashima, *Journal of Applied Crystallography* 38 (2005) 374-376.
- [134] B. Jiang, J.-M. Zuo, J. Friis, J.C.H. Spence, *Microscopy and Microanalysis* 9 (2003) 457-467.

- [135] K. Gjonnes, J. Gjonnes, J. Zuo, J.C.H. Spence, *Acta Crystallographica Section A* A44 (1988) 810-820.
- [136] K. Gjonnes, Y. Cheng, B.S. Berg, V. Hansen, *Acta Crystallographica Section A* A54 (1998) 102-119.
- [137] K. Gjonnes, N. Boe, *Micron* 25 (1994) 29-44.
- [138] Y.F. Cheng, W. Nuchter, J. Mayer, A. Weickenmeier, J. Gjonnes, *Acta Crystallographica Section A* A52 (1996) 923-936.
- [139] D.M. Bird, M. Saunders, *Ultramicroscopy* 45 (1992) 241-251.
- [140] X.H. Sang, A. Kulovits, J.M.K. Wiezorek, *Acta Crystallographica Section A* A67 (2011) 229-239.
- [141] D. Watanabe, R. Uyeda, A. Fukuhara, *Acta Crystallographica Section A* A25 (1969) 138.
- [142] A. Fukuhara, *J. Phys. Soc. Jpn.* 21 (1966) 2645-2662.
- [143] J. Gjonnes, R. Hoier, *Acta Crystallographica Section A* A27 (1971) 313.
- [144] J.M. Zuo, J.C.H. Spence, J. Downs, J. Mayer, *Acta Crystallographica Section A* A49 (1993) 422-429.
- [145] J. Zuo, *Acta Crystallographica Section A* A49 (1993) 429-435.
- [146] R. Vincent, D.R. Exelby, *Acta Crystallographica Section A* A51 (1995) 801-809.
- [147] J. Spence, *Acta Crystallographica Section A* A54 (1998) 7-18.
- [148] K. Mueller, M. Schowalter, J. Jansen, K. Tsuda, J. Titantah, D. Lamoen, A. Rosenauer, *Ultramicroscopy* 109 (2009) 802-814.
- [149] v.C.H. Mac Gillavry, *Physica* 7 (1940) 329-343.
- [150] W. Kossel, G. Möllenstedt, *Annalen Der Physik* 428 (1939) 113-140.
- [151] H. Bethe, *Annalen Der Physik* 392 (1928) 55-129.
- [152] P. Goodman, G. Lehmpfuhl, *Acta Crystallographica* 22 (1967) 14-24.
- [153] P.N.H. Nakashima, *Physical Review Letters* 99 (2007) 125506.
- [154] P.N.H. Nakashima, B.C. Muddle, *Physical Review B* 81 (2010) 115135.
- [155] B.F. Buxton, J.A. Eades, J.W. Steeds, G.M. Rackham, *Phil. Trans. R. Soc. Lond. A* 281 (1976) 171-194.
- [156] P. Goodman, *Acta Crystallographica Section A* A40 (1984) 522-526.
- [157] P. Liu, J. Skogsmo, *Acta Crystallographica Section B* 47 (1991) 425-433.

- [158] M. Tanaka, *Acta Crystallographica Section A* A50 (1994) 261-286.
- [159] A.W.S. Johnson, B.M. Gatehouse, *Acta Crystallographica Section B* 36 (1980) 523-526.
- [160] M. Tanaka, R. Saito, H. Sekii, *Acta Crystallographica Section A* A39 (1983) 357-368.
- [161] M. Tanaka, H. Sekii, T. Nagasawa, *Acta Crystallographica Section A* A39 (1983) 825-837.
- [162] F.W. Schapink, S.K.E. Forghany, B.F. Buxton, *Acta Crystallographica Section A* A39 (1983) 805-813.
- [163] J.W. Steeds, R. Vincent, *Journal of Applied Crystallography* 16 (1983) 317-324.
- [164] A.F. Moodie, H.J. Whitfield, *Acta Crystallographica Section B* 42 (1986) 236-247.
- [165] D.M. Bird, Q.A. King, *Acta Crystallographica Section B* B46 (1990) 202-208.
- [166] S. Swaminathan, I.P. Jones, N.J. Zaluzec, D.M. Maher, H.L. Fraser, *Materials Science and Engineering: A* 170 (1993) 227-235.
- [167] R.H. Blessing, D.Y. Guo, D.A. Langs, *Acta Crystallographica Section D-Biological Crystallography* D52 (1996) 257-266.
- [168] K. Tsuda, Y. Ogata, K. Takagi, T. Hashimoto, M. Tanaka, *Acta Crystallographica Section A* A58 (2002) 514-525.
- [169] M.T. Dove, *Introduction to Lattice Dynamics*, Cambridge University Press, London, 1993.
- [170] B.T.M. Willis, A.W. Pryor, *Thermal Vibrations in Crystallography*, Cambridge University Press, London, 1975.
- [171] S. Plimpton, *J. Comput. Phys.* 117 (1995) 1-19.
- [172] R.R. Zope, Y. Mishin, *Physical Review B* 68 (2003) 024102.
- [173] W.G. Burgess, Charge density determination in semiconductors and other materials by electron diffraction, in: *vol Doctor*, Cambridge University, 1994.
- [174] J.M. Zuo, *Ultramicroscopy* 41 (1992) 211-223.
- [175] P. Blaha, K. Schwarz, P. Sorantin, S.B. Trickey, *Computer Physics Communications* 59 (1990) 399-415.
- [176] J.P. Perdew, Y. Wang, *Physical Review B* 45 (1992) 13244.
- [177] J.P. Perdew, K. Burke, M. Ernzerhof, *Physical Review Letters* 77 (1996) 3865-3868.
- [178] D. Xu, H. Wang, R. Yang, P. Veysiere, *Acta Materialia* 56 (2008) 1065-1074.
- [179] J.S. Reid, J.D. Pirie, *Acta Crystallographica Section A* A36 (1980) 957-965.

- [180] M. Mostoller, R.M. Nicklow, D.M. Zehner, S.C. Lui, J.M. Mundenar, E.W. Plummer, *Physical Review B* 40 (1989) 2856-2872.
- [181] A.G. Fox, *Scripta Metallurgica Et Materialia* 32 (1995) 343-347.
- [182] L.M. Peng, J.M. Zuo, *Acta Crystallographica Section A* A55 (1999) 1026-1033.
- [183] M.D. Shannon, J.W. Steeds, *Philosophical Magazine* 36 (1977) 279-307.
- [184] B.F. Buxton, J.E. Loveluck, J.W. Steeds, *Philosophical Magazine A* 38 (1978) 259-278.
- [185] K. Momma, F. Izumi, *Journal of Applied Crystallography* 41 (2008) 653-658.
- [186] E.S.K. Menon, A.G. Fox, *Philosophical Magazine* 77 (1998) 577-592.
- [187] G. Kresse, J. Hafner, *Physical Review B* 47 (1993) 558-561.
- [188] G. Kresse, J. Hafner, *Physical Review B* 49 (1994) 14251-14269.
- [189] G. Kresse, J. Hafner, *Journal of Physics: Condensed Matter* 6 (1994) 8245.
- [190] G. Kresse, J. Furthmueller, *Computational Materials Science* 6 (1996) 15-50.
- [191] G. Kresse, J. Furthmueller, *Physical Review B* 54 (1996) 11169-11186.
- [192] F.W. Kutzler, G.S. Painter, *Physical Review B* 43 (1991) 6865-6872.
- [193] E.S.K. Menon, A.G. Fox, R. Mahapatra, *Journal of Materials Science Letters* 15 (1996) 1231-1233.
- [194] E.I. Blount, *Physical Review* 126 (1962) 1636.
- [195] H.J. Fischbeck, *physica status solidi (b)* 38 (1970) 11-62.
- [196] E. Brown, *Physical Review* 133 (1964) A1038.
- [197] Y. Shen, D.E. Laughlin, *Philosophical Magazine Letters* 62 (1990) 187 - 193.